

**REVIEW**

# Hierarchical biopolymer-based materials and composites

Jeremy L. Fredricks<sup>1</sup> | Andrew M. Jimenez<sup>1</sup>  | Paul Grandgeorge<sup>1</sup>  |  
Rachel Meidl<sup>2</sup> | Esther Law<sup>1</sup> | Jiadi Fan<sup>3</sup> | Eleftheria Roumeli<sup>1</sup> 

<sup>1</sup>Materials Science and Engineering Department, University of Washington, Seattle, Washington, USA

<sup>2</sup>Baker Institute for Public Policy, Rice University, Houston, Texas, USA

<sup>3</sup>Department of Aerospace Engineering and Mechanics, University of Minnesota, Minneapolis, Minnesota, USA

**Correspondence**

Eleftheria Roumeli, Materials Science and Engineering Department, University of Washington, Seattle, WA 98195, USA.  
Email: [eroumeli@uw.edu](mailto:eroumeli@uw.edu)

**Abstract**

The mass production and disposal of non-degradable fossil-based plastics is responsible for alarming environmental and social issues when not managed responsibly. Towards manufacturing environmentally-friendly materials, *biopolymers*, that is, polymers synthesized by living organisms, emerge as promising sustainable alternatives as they combine attractive mechanical properties, compostability, and renewable sourcing. In this review, we analyze the structural and mechanical properties of three of the most studied biopolymer classes: cellulose, chitin, and protein beta-sheet structures. We first discuss the hierarchical structure of the biopolymers and how their rich interaction networks induce appealing mechanical properties. Then, we review different fabrication and processing methods to translate these attractive properties into macroscopic materials and composites. Finally, we discuss a nascent approach, which leverages the direct use of microorganisms, in the form of intact cells, tissues or dissociated biological matter (biomatter), as meso-scale material building blocks. These non- or little pre-processed biomatter building blocks are composed of the biopolymer structural elements (molecular-nano scale), but also inherit the higher-scale hierarchical characteristics. Processing-structure-property relationships for biomatter-based materials are discussed, emphasizing on the role of hierarchical arrangement, processing-induced transformations, and intermolecular bonding, on the macroscopic mechanical properties. Finally, we present a perspective on the role of biopolymers in a circular economy.

**KEYWORDS**

biological-matrix materials, biopolymers, hierarchical materials, mechanical properties, structure-property relationships, sustainable materials

## 1 | INTRODUCTION

The global increase in materials production, combined with the limited fossil resources used to fabricate numerous materials, urgently call for innovations towards

designing sustainable materials with a controlled environmental and social impact. Polymeric materials are used in a very wide range of applications, and yet their sourcing, production and post-use strategies create undeniably detrimental environmental and health effects.<sup>1,2</sup> Potential solutions include the usage of *structural biopolymers*: load-bearing polymers synthesized naturally by living organisms, that can be used either as bulk materials,

Jeremy L. Fredricks, Andrew M. Jimenez, and Paul Grandgeorge contributed equally to this work.

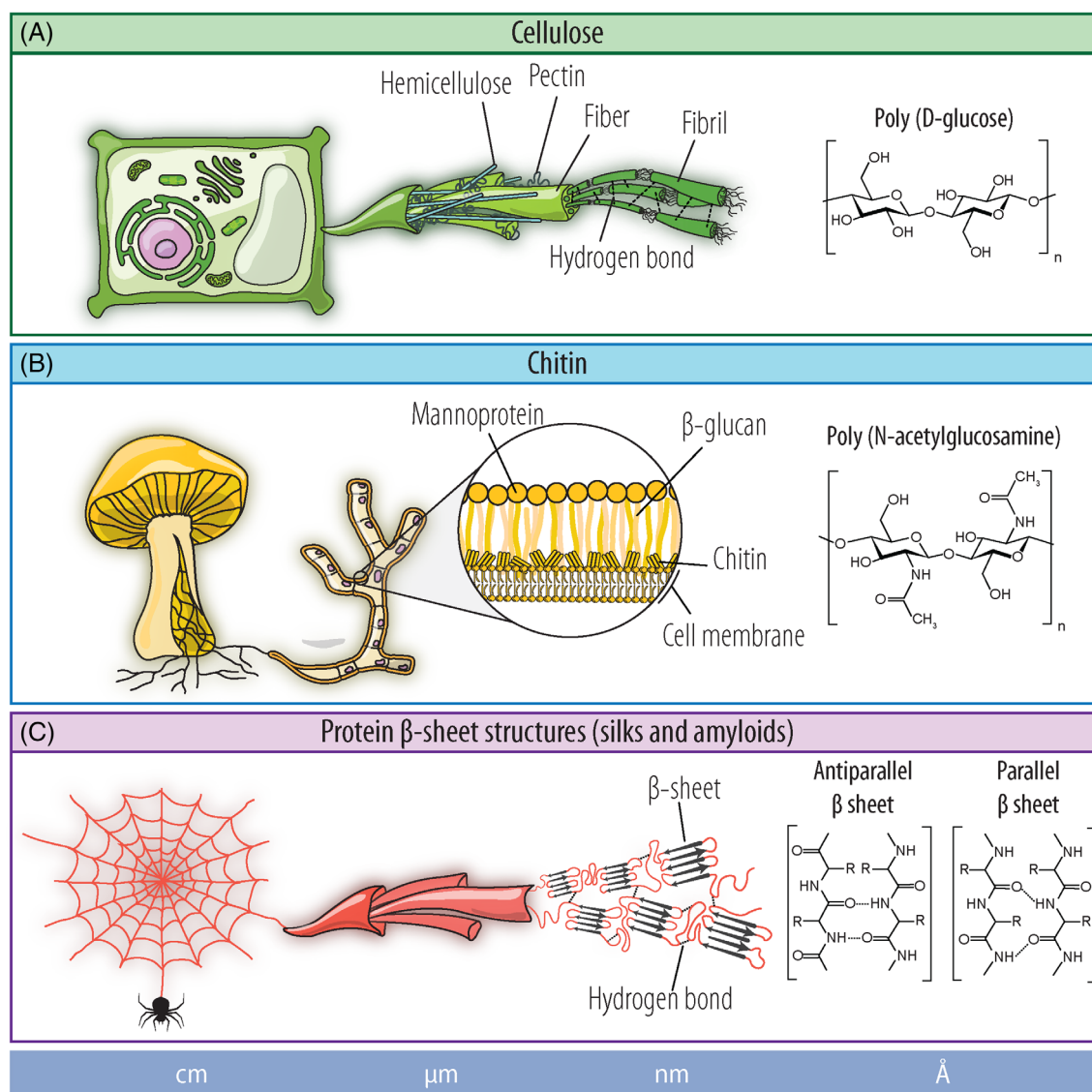


**FIGURE 1** Structural biopolymers in biomatter. (A) Cellulose is a polysaccharide which can be found in land plants and algae cell walls, as well as in some tunicates and bacteria. (B) Chitin is a polysaccharide typically found in the mycelium of fungi and in the exoskeleton of some crustaceans and insects. (C) Protein  $\beta$ -sheet structures (silks and amyloids) have remarkable mechanical properties. Silks are produced by spiders and silkworms and amyloids are synthesized by some species of bacteria to form biofilms.

or as fillers in biocomposites. This class of biopolymers, which includes cellulose, chitin, silk and collagen among others, shows appealing mechanical properties owing to the hierarchical structure that spans multiple orders of magnitude.<sup>3</sup> In this review, the term biopolymer will strictly refer to polymers synthesized directly from living organisms. In contrast, the term bio-based polymers will be used for polymers made by synthetic chemistry processes from bio-based monomers. As an example of bio-based polymer, ring-opening polymerization of lactic acid monomers (obtained from starch-rich biomass) is used to produce polylactic acid (PLA). Note that the molecular structure of some bio-based polymers prevents them from being biodegradable (e.g., bio-polyethylene terephthalate;

bio-PET). Biopolymers, on the other hand, can reasonably be assumed to be fully biodegradable.

An example of structural biopolymers arises in natural fibers, also known as biofibers or plant fibers, which are natural composites of multiple biopolymers extracted from plant biological materials (biomatter).<sup>4,5</sup> The fibers diameters typically range in the tens to hundreds of micrometers, and their composition and microstructure depend on the source species.<sup>6</sup> Natural fibers have been employed extensively over the past few decades as fillers in a variety of polymers giving rise to the “traditional biocomposite” materials class. For example, bamboo, jute, kenaf, flax, hemp, have been introduced into commodity thermoplastics such as polypropylene (PP), polyethylene

(PE), polystyrene (PS), and polyvinyl chloride (PVC), as well as thermosets such as epoxies and phenol formaldehyde.<sup>5,7,8</sup> These biocomposite materials have already reached markets like automotive and construction, offering the benefits of reducing the non-degradable polymer consumption, and being compatible with standard polymer processing methods. However, natural fibers typically require surface treatments to be compounded with hydrophobic polymer matrices, and their effects on the mechanical properties of the base polymer are not always positive.<sup>5,6</sup> Indeed, although natural fibers are partially composed of cellulose, a strong biopolymer, they also contain other non-structural weaker biopolymers. Therefore, the natural fibers mechanical properties at the fiber-level (micro- and meso-scales) are bound to be substantially lower than pure cellulose. To address this performance limitation, a generation of biocomposite materials emerged where only the extracted structural biopolymer is used as a filler or a matrix. Building on the hierarchical macromolecular backbone of structural biopolymers enables the design of high-performance, self-bonded, biodegradable polymers. Among the most studied structural biopolymers, cellulose, chitin, and protein  $\beta$ -sheet structures (mostly silks and amyloids), presented in Figure 1, have already been used widely in functional materials. Still, these polymers continue to receive an increasing attention in published literature and ongoing research strives to fully take advantage of their appealing properties, by harnessing their intricate processing-structure-property relations.

In this review, we discuss the current state of the art to valorize cellulose, chitin, and protein  $\beta$ -sheet structures by investigating their molecular structure, properties, and processing methods, as well as their emerging applications. The highlighted processing-structure-property relationships reveal the dominant role of the hierarchical design and structure of biopolymer-based materials on their macroscopic mechanical properties. While we primarily discuss fully biobased composites that require no synthetic binders to form macroscopic materials, we will also include selected examples of composites with synthetic materials to illustrate the versatility of these biopolymer-based material classes.

In addition to reviewing the properties of the extracted biopolymers, we cover a more recently developed class of materials, which uses unprocessed biomatter in the form of entire cells or tissues to serve as a meso-scale building block. These building blocks are composed of structural biopolymers as their nanoscale elemental components, but in contrast to the traditional biocomposites, they use the as-produced cells or whole microorganisms without extraction processes. The wide range of tailoring that natural organisms conduct to

engineer biopolymers with precise hierarchical features frames the vast property space that can be achieved when assembling such biopolymers into new materials. For the purposes of the present review, we focus on examples in which the biological organisms (cells or whole organisms or biomatter) or their products (pure structural biopolymers) are used as materials without requiring genetic modifications, or for the organism to remain living after the fabrication.

The goal of this review is to provide a comprehensive introduction to the vast research area of sustainable polymers, while also featuring recent advances in this field. Numerous approaches have been investigated to take advantage of polymers synthesized from living organisms, each with their own advantages and limitations. We present several of the different approaches while enabling a deeper understanding of the fundamental mechanisms at play at the molecular, meso, and macroscopic scales. This field of research undoubtedly garners increasing attention and several reviews in literature provide enlightening information from different perspectives. The curious reader looking to deepen their knowledge after reading this Review is referred to other material covering biobased approaches to design functional materials.<sup>9–13</sup>

## 2 | MACROMOLECULAR STRUCTURE AND MECHANICAL PROPERTIES OF BIOPOLYMERS

The biopolymers synthesized in the extracellular matrix or cell walls of micro-organisms, plants, fungi, bacteria or animal cells serve as structural building blocks with features spanning from the nanometric to the macro-scale. The macroscopic properties of these building blocks are rooted in the secondary bonding motifs at the molecular level, especially inter- and intra-molecular hydrogen bonding within natural macromolecular assemblies, which provide a rich network of interactions. In this first section, we focus on the structure-properties relationships of the three discussed biopolymer families: cellulose, chitin, and protein-based  $\beta$ -sheet structures (silk and amyloids in particular), as presented in Figure 1.

### 2.1 | Cellulose

Cellulose is the world's most abundant biopolymer and is one of the most studied natural materials. It has been used in a variety of applications prior even to the fundamental understanding of macromolecules. As an example

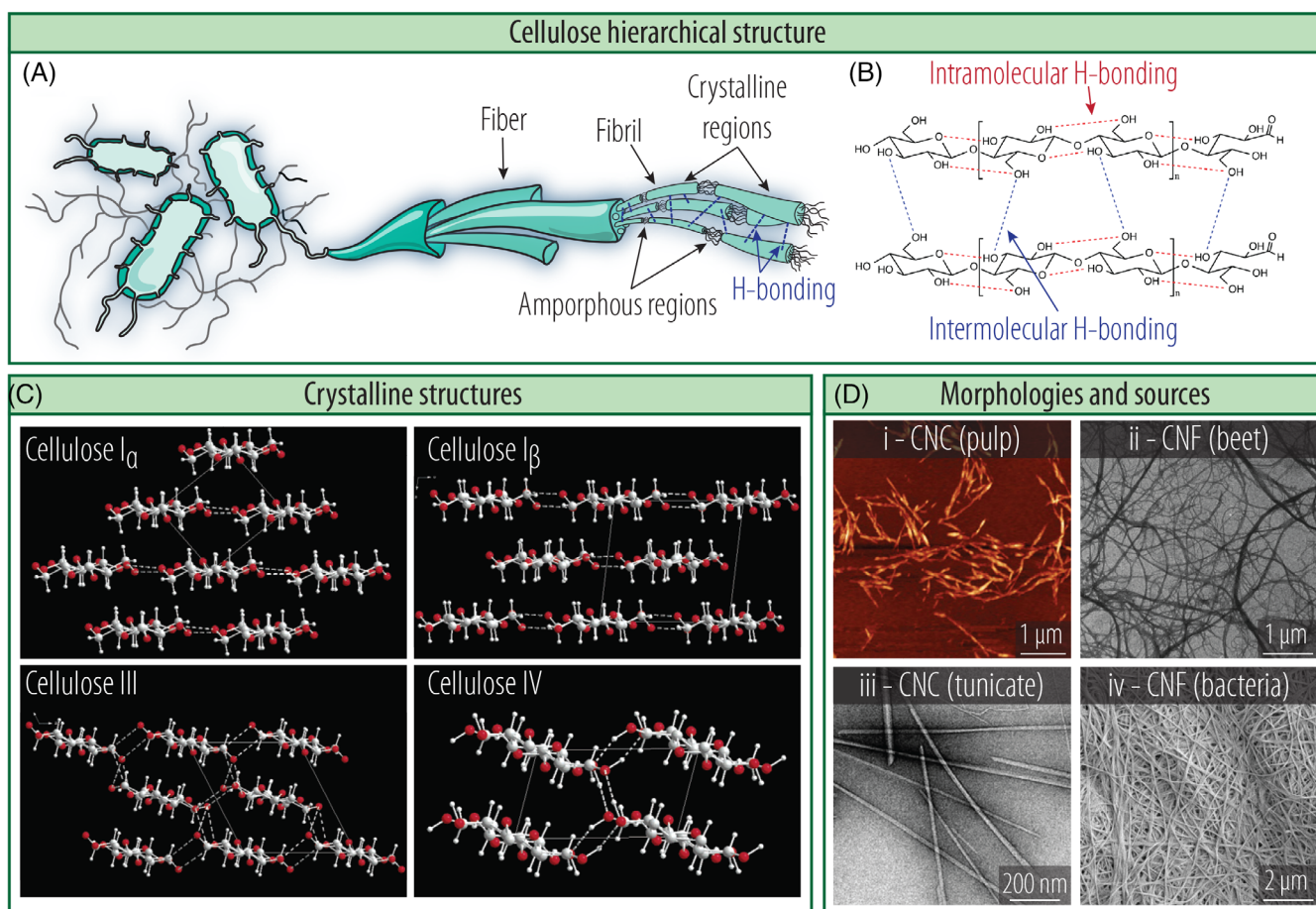


**FIGURE 2** Structure and morphology of cellulose. (A) Hierarchical composition of bacterial cellulose. Cellulose fibers are composed of fibrils, which contain crystalline and amorphous regions. The polymer chains interact through hydrogen-bonding and van der Waals forces. (B) Intra- and inter-molecular hydrogen bonding interactions in cellulose polymers. Reprinted from Reference 18 Copyright 2015, with permission from Elsevier. (C) Representations of the different crystalline structures of cellulose:  $I_{\alpha}$ ,  $I_{\beta}$ , III and IV polymorphs. Reprinted with permission from Reference 19 Copyright 2004 American Chemical Society. (D) Morphologies of different types of cellulose: (i) AFM image of CNC from bleached pulp fibers. Reproduced from Reference 20. (ii) TEM image of CNF from sugar beet. Reproduced from Reference 21. (iii) TEM image of CNC from tunicates. Reproduced from Reference 22 with permission from the Royal Society of Chemistry. (iv) SEM image of bacterial cellulose.

illustrating the technological importance of cellulose, 400 megatonnes of paper (made from cellulose fibers extracted from wood) were produced in 2008.<sup>14</sup> Other examples of cellulose used for technical materials are cellophane (transparent films) and Rayon (viscose fibers, where the cellulose is first solubilized and subsequently regenerated into a fiber).<sup>15</sup> The versatility of cellulose is rooted in the variety of molecular structures it can adopt, along with different molecular weights (or degree of polymerization), degrees of crystallinity, chain and fibril dimensions and aspect ratio, all of which influence its final macroscopic properties (mechanical, optical, and thermal). In this section, we discuss the biosynthesis of cellulose and focus on the macromolecular and hierarchical structure of pure cellulose fibers, along with their mechanical properties.

### 2.1.1 | Biosynthesis and macromolecular structure

Naturally synthesized by plants and some algal and fungal species, cellulose is a polysaccharide comprised of ringed glucose molecules that align linearly along the polymer backbone. The glucose monomers of the polymer chain are linked through  $\beta$  1–4 glycosidic bonds, where a covalent oxygen bond links the C1 and C4 carbons of adjacent rings<sup>3,12,16</sup> giving rise to the strong and stiff axial properties of cellulose. The symbol  $\beta$  denotes the orientation along which the linkage occurs, describing adjacent glucose rings being joined at  $180^\circ$ , which gives cellulose its linear structure. As presented in Figure 2A, cellulose is composed of hierarchical fibers, consisting of fibrils. These fibrils contain amorphous and

crystalline regions linked via secondary interactions. Through a combination of short-range but numerous hydrogen bonds with short and mid-range van der Waals interactions, cellulose molecular chains and their formed fibrils arrange into oriented fibers, which then utilize interfacial and interfibrillar level interactions to ultimately give rise to a well-bonded network.<sup>17</sup> The unit monomer and the linkage of a cellulose polymer are presented in Figure 2B, along with formed hydrogen bonds at the intermolecular level. The crystalline structure (Figure 2C) and morphologies depending on the cellulose source (Figure 2D) are discussed next.

In plants, cellulose is produced as the main structural element of cell walls. For land plants and algae in particular, cellulose synthase-like enzymes polymerize glucose moieties from uridine diphosphate glucose (UDP-Glc) into  $\beta$ -1,4-glucan chains, producing rigid crystalline cellulose nanofibrils (CNF).<sup>23,24</sup> In addition, the cell wall also contains a heterogeneous mixture of amorphous pectins, hemicelluloses, proteins and phenolics (later polymerizing to form lignin) which embed the cellulose fibers into a nanocomposite network.<sup>25,26</sup> Throughout the thickness of the cell wall, the relative concentration of biopolymers and their three-dimensional (3D) arrangement vary throughout the organism's developmental stage, and depends on the species and growth conditions.<sup>25–31</sup> Popper and Tuohy<sup>24</sup> proposed that the variable degrees of polymerization, dimensions and aspect ratios of the cellulose fibrils are controlled by the different terminal synthase complexes. In woody-plants, during the late stages of development, lignin polymerization is observed in the inner parts of the cell wall (secondary cell walls), thereby conferring superior strength through reinforcement by bridging the load bearing cellulose fibrils in a rigid composite structure.<sup>26–28,32</sup>

Brown and red algae, as well as bacteria, have linear terminal complexes with particles arranged in 1–4 rows which produce flat, ribbon-like cellulose fibrils, in contrast to the more cylindrical fibrils produced in land plants.<sup>24,33</sup> In some red algae species, even disordered cellulose microfibrils have been revealed, from observations during cell elongation.<sup>34</sup> We refer the reader to comprehensive reviews regarding the vast diversity of cell walls found in algal species.<sup>24,35</sup>

In some species of bacteria, pure cellulose, secreted in the form of semicrystalline fibrils, is deposited in the extracellular space but does not remain attached to the cell, marking a significant difference with the organisms discussed above, for which cellulose contributes to the structural stability at the cell level. The secreted cellulose nanofibrils form an intricate layered three-dimensional (3D) hydrogel network, called a pellicle, at the interface between the growth medium and air. It has been

hypothesized that this hydrogel may confer benefits to bacteria by protecting against pathogens, foreign organisms, and ultraviolet light, preventing dehydration, and trapping carbon dioxide, which in turn helps bacteria float.<sup>36,37</sup> Similarly to plant cells, bacteria consume low molecular weight sugars or other carbon sources and the cellulose synthase complex polymerizes glucose moieties from UDP-Glc into  $\beta$ -1,4-glucan chains. One of the most common cellulose producing bacteria, *Komagataeibacter xylinus* (*K. xylinus*), formerly known as *Gluconoacetobacter xylinus* and *Acetobacter xylinum*, can polymerize up to 200,000 glucose molecules into  $\beta$ -1,4-glucan chains per second.<sup>23</sup> The pathways of glucose synthesis in bacteria are relatively well known, but the molecular mechanisms involved in the monomer polymerization into long cellulose chains are still elusive.<sup>38</sup>

The intra-chain hydroxyl groups of a glucose ring and the oxygen of the adjacent ring are repeated between adjoining glucose units, thereby stabilizing the linear configuration of the cellulose chain. The combination of hydrogen and van der Waals bonds promote parallel stacking between neighboring cellulose chains. In the produced structures, cellulose fibrils have crystalline regions with ordered, regularly conformed macromolecules coexisting with disordered (amorphous) regions. Currently accepted model arrangements include crystalline cores coated with disordered sheath layers, and disordered domains present in between crystalline cores along the fiber axis.<sup>10,39</sup> In addition, experimental and simulation results suggest that the biosynthesized cellulose fibrils experience a twist.<sup>40–42</sup> The presence of amorphous regions has been suggested as a mechanism to release stresses involved with the fibril twist,<sup>43</sup> however the length scale at which it occurs is still a matter of investigation.<sup>41</sup> The dimensions of both the crystalline and amorphous regions are typically in the nanoscale. Cellulose nanocrystals (CNC) are the regions with only ordered cellulose and extend to 10–25 nm in length for algae and bacteria, and 100–150 nm for land plants.<sup>44</sup> For pure cellulose fibrils as the ones produced by *K. xylinus*, an average diameter of 3.5 nm has been reported, while hydrogen- and van der Waals-bonded fibrils are known to induce the formation of nanofibrils with diameters <35 nm.<sup>3</sup> Depending on the organism or processing method applied, the nanofibrils can be organized into micron-sized fibers as detailed below in Section 3.1.

Crystalline cellulose can take the structure of four different polymorphs referred to as type I, II, III, and IV (presented in Figure 2C). Naturally synthesized cellulose from plants, algae, bacteria and tunicates, has been identified as phase I. This state is thermodynamically metastable and can transform into phase II or III by rearranging hydrogen bonding through regeneration or

mercerization processes (aqueous sodium hydroxide treatments). Despite its metastability, cellulose I has been extensively studied due to its wide availability, and has been predicted to have higher axial elastic modulus than cellulose II.<sup>12</sup>

Natural cellulose (polymorph I) can conform into two allomorphs, identified as triclinic,  $I_\alpha$  (P1 space group), and monoclinic,  $I_\beta$  (P21 space group), which coexist in different relative amounts, ranging from 100%  $I_\alpha$  to 100%  $I_\beta$  (see crystalline structures in Figure 2C). Plants and tunicates primarily synthesize a  $I_\beta$ -dominant cellulose, whereas algae and bacteria produce cellulose richer in  $I_\alpha$  phase (with exceptions like the green algae species, *Micrasterias*, which primarily produces  $I_\beta$  cellulose). There is no universally accepted  $I_\alpha$ : $I_\beta$  ratio determined for all cellulose-producing species, and the two allomorphs can be found to coexist not only in the same species but even within a single elemental fibril.<sup>3</sup> Within a single algae species, *Salicornia brachiata* in particular, the  $I_\alpha$ : $I_\beta$  ratio varies from the stem to the tip, decreasing from 9.3 to 1.5.<sup>45</sup> The biosynthesis conditions, the species, as well as the potential extraction methods determine the crystal conformation ratio and the distribution of amorphous domains in cellulose fibrils. The most important difference between the two crystal conformations is the so-called *hydrogen bonding plane*, which refers to the plane in which inter- and intra-molecular bonding of the neighboring glucose units occurs. The exceptionally high axial stiffness (typically hundreds of GPa) of cellulose fibrils is attributed to the strong cooperative effects between intra-chain hydrogen-bonding and covalent bonding, while strength (typically hundreds of MPa), the unique plastic deformation behavior and enhanced toughness are related to inter-chain hydrogen bonding as well as dispersive fibril-level interactions between neighboring cellulose chains on the same or parallel planes<sup>17,46,47</sup> (see Figure 2C). On the other hand, the non-axial interactions between cellulose chains (in directions other than the principal one), are suggested to be dominated by weaker but longer range, van der Waals forces. The higher thermodynamic stability of  $I_\beta$  over  $I_\alpha$  is related to the greater inter-chain hydrogen and van der Waals bonding in the non-principal planes. The same reason would also justify the higher stiffness and strength of  $I_\beta$  over  $I_\alpha$ . Yet, some reports mention  $I_\alpha$  cellulose exhibiting higher stiffness than  $I_\beta$ .<sup>48</sup> The conflicting mechanical properties for the two phases,<sup>12,49</sup> may be associated with the processing method to extract and prepare the samples as well as with the difference of testing method used in each case.

Besides the crystalline structure, the length of cellulose chains, or degree of polymerization (DoP), also varies greatly depending on the source, the processing of the

material and the testing conditions. Inherent polydispersity of the polymer provides DoP values that can range from 10 to 100,000.<sup>50</sup> Measurements to obtain an average DoP are highly dependent on hydrolyzing steps, often necessary for isolating cellulose chains. Using derivatization methods that attempted to maintain the source length of the chains, cellulose DoP values from various plant species ranged from 1000 to 5000, measured viscometrically, where woody biomatter tends to have higher values than non-woody.<sup>51</sup> Using size-exclusion chromatographic analysis with multi-angle light scattering detection (SEC-MALLS), Yanagisawa et al.<sup>52</sup> confirmed this range and showed the DoP of an algal cellulose to be 4300, similar to the high end of plant species, whereas the bacterial cellulose (BC) in the study was measured at 7300. These numbers illustrate the diversity of cellulose chains produced across species, but even within a single species, the DoP can vary significantly depending on the location. For example, in the primary cell wall, the DoP typically lies in the range ~2000–6000, while it goes up to 14,000 in the secondary cell wall.<sup>53,54</sup>

### 2.1.2 | Mechanical properties of cellulose fibers

The hierarchical structure of cellulose chains, conformed into nanocrystals and subsequently into elemental fibrils which are bundled into fibers gives rise to a set of unique properties, and confers mechanical properties that are comparable to engineering materials like steel, Kevlar and carbon fibers,<sup>12</sup> especially considering the relative low density of cellulose ( $\rho = 1.6 \text{ g/cm}^3$ ). Experimentally characterizing the mechanical properties of crystalline cellulose can be challenging because of the coexistence of amorphous and crystalline regions in samples of testable size (typically >mm). A common method to measure axial modulus ( $E_A$ ) consists in applying a known tensile load at the ends of a cellulose fiber and measuring the local strain of crystals using spectroscopic methods such as X-ray Diffraction (XRD). The underlying assumption of such coupled method is that stress is transmitted equally in amorphous and crystalline regions. The axial and transverse modulus ( $E_T$ ) of cellulose has also been widely predicted using numerical simulations based on molecular mechanics and molecular dynamics. Experimentally quantifying tensile strength ( $\sigma_f$ ) of crystalline cellulose results even more challenging since failure of macroscopic samples will occur in the weaker amorphous regions (a failure mechanism in cellulose is discussed by Zhu et al.<sup>46</sup> and presented below in Figure 6A). In Table 1, we present ranges of mechanical properties reported for crystalline cellulose, along with the method

used to determine them and the source material used. These results are also compiled graphically in the diagrams of Figure 3, enabling a comparison with other natural and synthetic materials.

The axial elastic modulus of crystalline regions of ramie cellulose fibers under constant uniaxial tension as tested from X-ray diffraction (XRD) is reported to be 138, 88, 87, 58, and 75 GPa for cellulose I, II, III<sub>I</sub>, III<sub>II</sub>, and IV<sub>I</sub>, respectively.<sup>56</sup> Exceptionally high elastic modulus in the axial direction for purely crystalline cellulose I, was also estimated through in-situ tensile/XRD, 120–138 GPa, and inelastic X-ray scattering tested  $220 \pm 50$  GPa.<sup>12,58</sup> Atomic force microscopy (AFM) tests of single cellulose I nanocrystals from acid hydrolyzed pulp, show a transverse modulus ( $E_T$ ) of 18–50 GPa for cellulose I fibrils with a thickness of 3–8 nm.<sup>57</sup> However, we note that these values were calculated as the force divided by cell wall cross-sectional area, which might not be representative of the cellulose nanocrystals loaded cross-section. On the other hand, AFM on bacterial cellulose (BC) from *K. xylinus* fibrils with sizes varying between 27 and 88 nm, shows an elastic modulus of  $78 \pm 13$  GPa which is independent of the fibril diameter.<sup>63</sup> In-situ Raman during tensile testing of a single BC fibril of the same species results in an elastic modulus of 114 GPa.<sup>64</sup> The same method shows an elastic modulus of about 143 GPa along the axial direction for tunicate-cellulose nanopapers.<sup>65</sup> Using a sonication-induced fragmentation method based on implosion dynamics of cavitation bubbles to calculate the strength of wood- and tunicate-derived nanocellulose after TEMPO-oxidation, shows strengths of 1.6–3.0 and 3–6 GPa for wood- and tunicate-derived cellulose, respectively.<sup>61</sup> The authors mention that this is an underestimation of the true strength since they employ sonication in their tests, which introduces mechanical defects in the nanofibrils such as kinks and delamination of the molecular sheets. These defects act as failure points initiating “catastrophic” tensile fracturing. In addition, TEMPO oxidation alters the cellulose surface which the authors propose possibly lowers the strength of the nanofibrils. Finally, AFM tests on tunicate *Halocynthia papillosa* cellulose fibrils of about 8 nm thickness, after performing TEMPO oxidation or acid hydrolysis, show an elastic modulus of 145.2 GPa for the TEMPO cellulose, and 150.4 GPa for the acid-hydrolyzed cellulose.<sup>66</sup>

The Young's modulus of cellulose I and II in the principal fibril chain axis was theoretically predicted to be 167.5 and 162.1 GPa, respectively.<sup>67</sup> For type I crystals, the two transverse elastic moduli are significantly lower; 15 and 55 GPa, revealing the highly anisotropic properties of crystalline cellulose. The anisotropy is less pronounced for cellulose II, with the two transverse moduli

both being about 18 GPa.<sup>67</sup> The axial modulus is found to be mainly dependent on the intra-molecular hydrogen bonds along the chain axis, rather than the inter-molecular interactions. Specifically, if the calculations neglect the contribution of the hydrogen bond between the hydroxyl side group and the ether oxygen atom of the glucose ring, the axial modulus prediction becomes 70 GPa, less than half the value initially predicted.<sup>67</sup> However, we note that eliminating the hydrogen bonds in such simulations has direct consequences in other significant parameters such as chain packing and orientation, which together with the fact that stiffness contributions from hydrogen bonds, dispersive interactions and covalent bonds are not necessarily additive, complicates the estimation of how each of those factors contribute to cellulose stiffness by themselves.<sup>17</sup> In cellulose fibrils, the hydrogen-bonded sheets, containing covalent intramolecular bonds, are stacked together in parallel planes, which are held primarily by van der Waals (non-bonding) interactions, and, therefore, the modulus is high within the sheet plane and much lower in the normal directions. As discussed in the above, in addition to hydrogen bonding which directly impacts the packing and stabilizes the axial orientation of cellulose chains at the molecular and inter-molecular level, and likely participates in inter-fibril bonding, the contributions from longer-range van der Waals and ionic interactions, along with inter-chain diffusion and fibrillar interlocking at the interfibril and macrofiber level should not be discarded.<sup>17</sup>

#### Cellulose-based cell wall properties

When cellulose fibers remain embedded in their native state within a plant cell wall matrix, the mechanical properties of the composite material are far inferior to those of pure cellulose, as expected. This difference is clearly illustrated when the properties of primary cell walls of plants are measured. Suspension cultured plant cells (*Arabidopsis thaliana* sp.), when tested through AFM, show an indentation modulus as small as 0.1–1 MPa attributed to the hydrated cell wall composite.<sup>68</sup> Cell walls of the tissue-bonded cells of the same species show moduli varying between 0.1 and 50 MPa when tested with AFM or nanoindenter, which upon finite element modeling reveal an approximate 80–160 MPa modulus for the homogenized cell wall material.<sup>69</sup> This range within the same species arises from the fact that the cell wall properties were measured from different methods and with different indenter shapes, stiffnesses and indentation rates, as well as from the biological variability of the samples. Still, the significantly lower range of cell wall modulus when compared to pure crystalline cellulose, is a result of the semicrystalline state of cellulose in

TABLE 1 Properties of pure crystalline cellulose determined experimentally.

Material	Crystal system	$E_A$ (GPa)	$E_T$ (GPa)	$\sigma_f$ (GPa)	Method	Reference
Cellulose I (unspecified if $\alpha$ or $\beta$ )		120–138			XRD	55,56
				18–50	AFM	57
Cellulose I $_{\beta}$	Monoclinic, P21	220	15		Inelastic X-ray scattering	58
					XRD	59
					AFM	60
					2–6	Cavitation
Cellulose II	Monoclinic, P21	88–112			XRD	55,56
				0.2–10	Raman	62
Cellulose III $_I$		87			XRD	56
Cellulose III $_{II}$		58			XRD	56
Cellulose IV		75			XRD	56

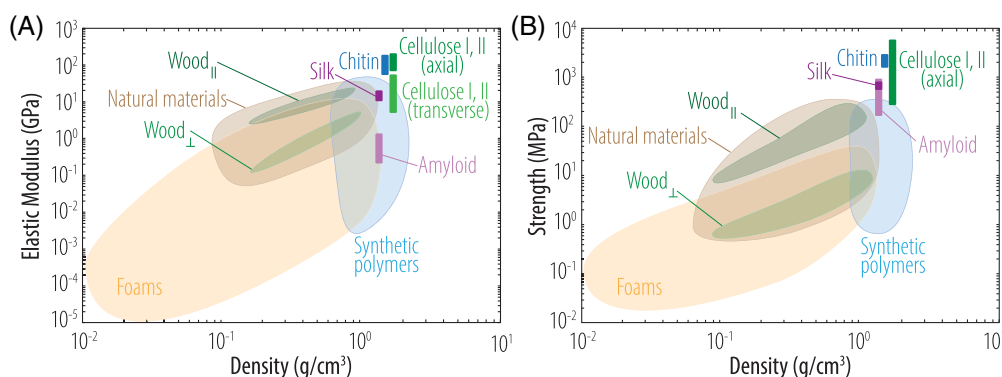


FIGURE 3 Mechanical properties of crystalline biopolymers in the context of natural and synthetic materials. (A) Elastic modulus and (B) strength. The values used to define the ranges of cellulose, chitin, silk and amyloids are respectively provided in Tables 1, 4, and 5.

the cell walls, with the presence of amorphous regions effectively reducing the strength and stiffness of the fiber, as well as the presence of the weaker polymer matrix of hemicelluloses, pectins and phenolic compounds that interconnect the cellulose fibrils through a network of hydrogen bonding in addition to polymer diffusion and fibril-level interactions.

Based on this compilation, it is apparent that the experimental method, assumptions, and precision have a major quantitative influence on the measured properties, so care should be taken when drawing general conclusions and comparisons. In addition, among mechanical testing, bulk macroscopic properties cannot be compared directly with nanoindentation or AFM, for example. In the former case, an “effective composite” material, with porosity-air voids and entire bulk fiber contribution, is tested while for the latter case, shallow nano-mechanical testing, localized pure elemental fibrils and sub-fibrils response are probed. Finally, the influence of environmental conditions (temperature and humidity) during testing, or sample pre-conditioning should also be considered, as they dramatically influence the measured properties.

### 2.1.3 | Molecular modeling methods furthering insights into bonding and mechanics of cellulose

Atomistic scale modeling has been applied to study the material properties of cellulose, as well as provide a fundamental understanding of the atomic-scale origins of these properties. Among various atomistic scale modeling methods, molecular mechanics (MM) simulation and molecular dynamics (MD) simulation are two typical methods to study the structure, mechanical properties of polymers and polymer composites.<sup>70–72</sup> MM simulation refers to the principle of energy minimization, where the positions of atoms are optimized to minimize the potential energy of the system. On the other hand, MD simulation is a computational tool to simulate the motions of atoms and molecules. In both MM and MD simulations of polymers, a force field (FF) is used to describe the interactions between atoms inside a molecule or between molecules. Different FFs have been developed for different purposes, including the widely used and general DREIDING FF,<sup>73</sup> along with others that are more focused to improve accuracy but also less generalizable, such as AMBER<sup>74,75</sup> and



OPLS.<sup>76,77</sup> Other widely applied and highly accurate FFs are PCFF<sup>78,79</sup> and COMPASS,<sup>80,81</sup> and the more recently developed ReaxFF, which is a bond order-based FF and allows continuous bond formation/breaking,<sup>82</sup> and machine learning-based FFs.<sup>83</sup>

In this section, the MM and MD simulations on mechanical properties of cellulose are summarized, and compared with experimental results. Most of simulation works in the literature focus on calculating the elastic modulus in axial direction of cellulose  $I_{\beta}$ , which is summarized in Table 2. The predicted elastic modulus of cellulose  $I_{\beta}$  are consistent with the experimental results, which are in range of 110–200 GPa.<sup>12,84–87</sup>

Given the importance of hydrogen bonding in cellulose that was discussed in the previous sections, molecular simulations have also been used to shed light specifically into the effects of hydrogen bonding on the elastic modulus of cellulose.<sup>86,93,95,96</sup> A summary of the reported results of elastic modulus in the axial direction of cellulose with and without hydrogen bonding contributions is shown in Table 3. A reduction of elastic modulus is observed without hydrogen bond, which is consistent with the experimental observation.<sup>97–99</sup>

In addition, MD simulations have been used to study other factors that influence mechanical properties of cellulose including moisture, and fiber twisting. Sahputra et al.<sup>94</sup> used MD simulations to study the effects of moisture on the mechanical properties of microcrystalline cellulose, and found that the axial elastic modulus of cellulose reduce with the increase of moisture content, which is consistent with the experimental results by Khan et al.<sup>100</sup> and Hancock et al.<sup>101</sup> MD simulations by Ramezani and Golchinfar focused on the effects of geometrical properties and twist on the mechanical properties of cellulose bundles.<sup>92</sup> They found that stiffness, strength, and toughness decrease for increasing bundle size (varying from  $2 \times 2$  to  $5 \times 5$  bundles) and applied end twist angle. As an example, the axial elastic modulus decreases with the twist angle and size up to 75%, as a result of covalent bond dissociation in the regions locally under high tension.

## 2.2 | Chitin

Chitin is another abundant natural structural polymer synthesized by numerous living organisms. This linear biopolymer makes up the principal fibrillar component of cell walls of some fungi which colonize substrates with filamentous cells called hyphae ( $2\text{--}10\ \mu\text{m}$  in diameter), forming an extended network called mycelium. Chitin is also synthesized in insect shells, crustaceans, squid pens, cocoon fibers of some beetles and other species, as well

as some algae. The hierarchical structure of chitinous materials is exemplified in Figure 4A by zooming into the lobster cuticle. This polymer has been extracted and adapted for numerous medicinal, industrial, and biotechnological purposes.

### 2.2.1 | Biosynthesis and macromolecular structure

Chitin is a polysaccharide structurally similar to cellulose with the only difference that it has an acetamide group instead of a hydroxyl group at the C2 position. It is a homopolymer of  $\beta$ -(1  $\rightarrow$  4)-linked, N-acetylglucosamine units.

Chitin synthase catalyzes the transfer and polymerization of N-acetylglucosamine from uridine diphosphate-N-acetylglucosamine into a growing chitin chain.<sup>104</sup> Similarly to cellulose chains, chitin nascent chains are also extruded through the cell membrane into the cell wall. The molecular structure of chitin chains enables strong hydrogen bonding, both intra-chain and inter-chain, in the planar direction, which together with other secondary interactions, ultimately lead to linear elemental fibrils which have crystalline (ordered) and amorphous (disordered) regions. In fungal species, similarly to plants, cell walls are assembled in a multilayered fibrillar nanocomposite structure. The innermost layer (i.e., closer to the cell membrane) is comprised of chitin chains conformed into crystalline fibrils, acting as the main load bearing elements, crosslinked through amorphous  $\beta$ -(1-3) and  $\beta$ -(1-6)-D glucan chains which extend throughout the whole cell wall thickness.<sup>104–107</sup> The branched glucans tether chitin fibrils to cell wall proteins, thereby creating a heterogeneous, fibrous nanocomposite.<sup>107</sup> The combination of chitin and glucan is considered to be the main polysaccharide building block of fungal cell walls.<sup>104–106</sup> Along the cell wall thickness, the subsequent layers vary significantly across species, but are generally comprised of a hydrated matrix of glycoproteins, mannans and other glucose-polysaccharides such as  $\beta$ -(1-6) and  $\alpha$ -(1-4) glucans, which are crosslinked with chitin and  $\beta$ -(1-3)-D glucan fibrils to give rise to a fibrillar nanocomposite cell wall.<sup>106,108</sup> Yeast cells differ to the rest of fungal cell walls, as they tend to have thinner cell walls, comprising of fewer outer layers, and therefore have exposed inner wall chitin and  $\beta$ -(1-3) glucans chains.<sup>106</sup> Another similarity to plant cell walls is the presence of complex amorphous polymerized phenolic compounds in some fungal species (e.g., in spores and black yeast). These phenolics, called melanins, are analogous to secondary plant cell wall lignins, and provide the cells with protection against pathogens and oxidants.<sup>106</sup>

TABLE 2 Summary of atomic modeling predictions of axial elastic modulus of cellulose I<sub>β</sub>, *T* represents temperature.

Method	Conditions	System size	Axial elastic modulus, <i>E<sub>A</sub></i> (GPa)	Reference
MM	DREIDING FF	Single chain	179.9 w/ hydrogen bonds, 70.8 w/o hydrogen bonds	88
MM	DREIDING FF	Single chain	167.5	67
MM	CHARMM FF	Single chain	148	89
MM	COMPASS FF	1 × 1 × 10 unit cell	Tension: 110.53, Compression: 144.88	90
MM	PCFF FF	4 × 4 × 10 unit cell	Tension: 124.6, Compression: 130.34	
MM	COMPASS FF	1 × 1 × 10 unit cell	Tension: 141.48, Compression: 153.81	
MM	PCFF FF	4 × 4 × 10 unit cell	Tension: 152.01, Compression: 154.82	
MD	<i>T</i> = 300 K, Drieding FF	Single chain	148	89
MD	<i>T</i> = 293 K, OPLS FF	34–36 cellulose chains	157	91
MD	<i>T</i> = 293 K	16–36 cellulose chains	140–200 depends on twist angles	92
MD	<i>T</i> = 300 K, ReaxFF	4 × 4 × 8 unit cell	107.8	93
MD	<i>T</i> = 300 K, ReaxFF	110 chains	190	94

TABLE 3 Summary of modeling and experimental studies of the elastic modulus in the axial direction with and without hydrogen bonds.

Method	Material	Axial elastic modulus, <i>E<sub>A</sub></i> (GPa)	Reference
With hydrogen bonds			
MM	Cellulose I <sub>α</sub>	136	95
MM	Cellulose I <sub>β</sub>	100	67
MD	Cellulose I <sub>β</sub>	139.5	86
XRD	Cellulose I <sub>α</sub>	155	98
XRD	Cellulose I <sub>β</sub>	149	97
XRD	Cellulose I <sub>β</sub>	116	99
Without hydrogen bonds			
MM	Cellulose I <sub>α</sub>	117	95
MM	Cellulose I <sub>β</sub>	40	67
MD	Cellulose I <sub>β</sub>	120.3	86
XRD	Cellulose I <sub>α</sub>	114	98
XRD	Cellulose I <sub>β</sub>	127	97
XRD	Cellulose I <sub>β</sub>	124	99

A significant functional difference between chitin and cellulose is the added interaction provided by the acetamide moiety. A common technique in processing chitin involves the removal of the acetyl group to expose the nitrogen, leading to the N-deacetylated derivative called chitosan. A typical chitin chain with ~90% acetylation can be reduced to ~35% acetylation, or less, thereby significantly changing the interaction potential of the molecule.<sup>109</sup> For an original chitin chain of 4000–12,000 units long, the deacetylation process can bring the DoP down by an order of magnitude.

Similarly to cellulose, chitin is also found to form multiple crystalline polymorphs, α-, β- and γ<sup>3,110,111</sup>

(α and β crystalline structures are presented in Figure 4B). α-Chitin has a two-chain orthorhombic unit cell with *P*<sub>2</sub><sub>1</sub><sub>2</sub><sub>1</sub><sub>2</sub><sub>1</sub> symmetry and anti-parallel chain conformation, which enable a strong network of inter- and intra-molecular hydrogen bonds.<sup>112</sup> β-Chitin has a weaker hydrogen-bonded intra-sheet parallel chain packing adopting a single-chain monoclinic unit cell, with *P*<sub>2</sub><sub>1</sub> symmetry. γ-Chitin, is a combination of the two with both parallel and anti-parallel structures. The most abundant and thermodynamically stable polymorph is α-chitin, which is found in insect shells, crustaceans, as well as some algae and mycelia. β-Chitin is found in squid pens, and γ-chitin is found in fungi, yeast, cocoon fibers

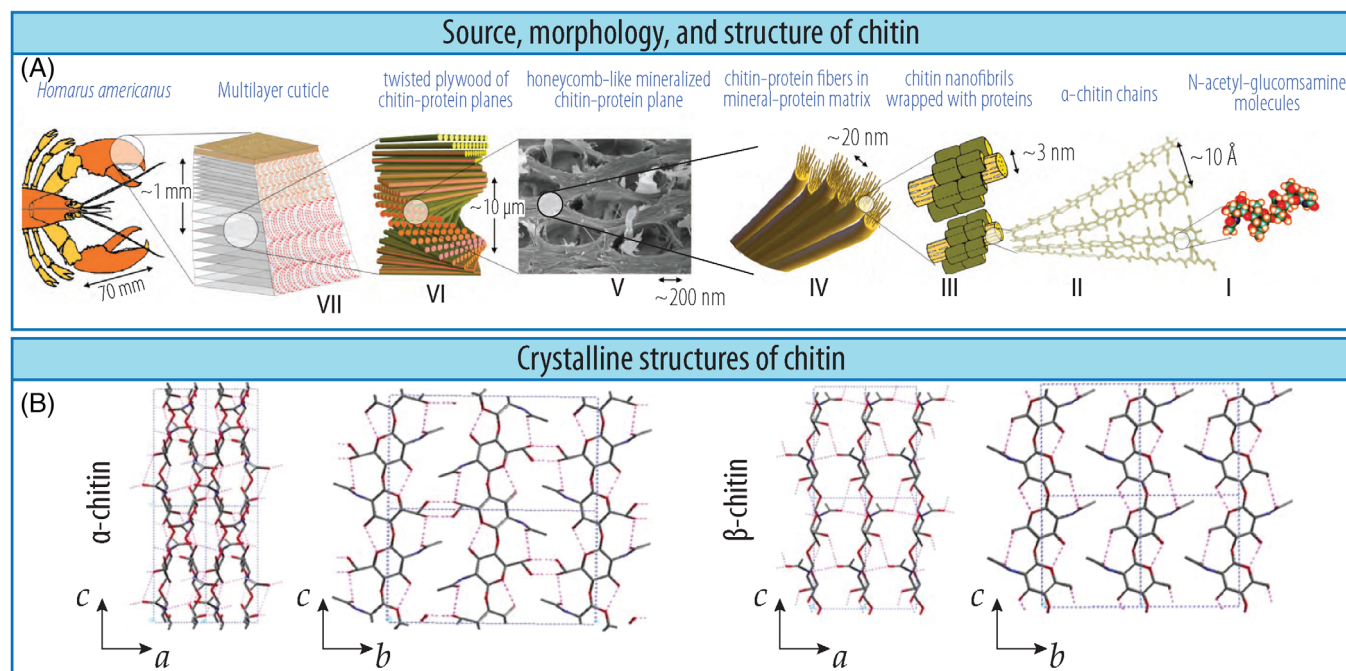


**FIGURE 4** Molecular structure of chitin. (A) Hierarchical structure of the lobster cuticle as an example of chitinous material. Adapted from Reference 102. (B) Representations of the crystalline structure of  $\alpha$ -chitin (left) and  $\beta$ -chitin (right). Dashed lines represent intra and inter-sheet hydrogen bonds. Adapted from Reference 103 Copyright 2006, with permission from Elsevier.

of some beetles and other species.<sup>110</sup> It is estimated that about 18–20 chains comprise an elemental chitin fibril of about 7 nm in diameter<sup>113</sup> and that purely crystalline chitin has a bulk density of  $\rho \approx 1.4 \text{ g/cm}^3$ .

### 2.2.2 | Mechanical properties of chitin fibers

The elastic properties of chitin nanocrystals were characterized by measuring the elongation using XRD patterns during loading. Duan et al.<sup>114</sup> reported that the axial elastic modulus of  $\alpha$ -chitin varies between 41 and 60 GPa, while  $\beta$ -chitin reaches values as high as 150 GPa. In another study, tensile tests of dried  $\alpha$ -chitin nanofibrils (ChNFs) assembled into macroscopic fibers showed a Young's modulus of 7.3 GPa, tensile strength of 171 MPa and elongation to break 5.1%.<sup>115</sup> Based on local XRD-diffractograms collected during tension experiments on the same nanofibrils, the elastic modulus of the crystalline regions was measured at 41 GPa.<sup>115</sup> In the same order of magnitude, a similar analysis by Ogawa et al.<sup>112</sup> on  $\alpha$ -chitin of snow crab (*Chionoecetes opilio*) estimated the crystalline elastic modulus to be  $59.3 \pm 11.3 \text{ GPa}$ . Cavitation-induced tensile fracture experiments on  $\alpha$ -chitin nanofibrils, extracted from *Phaeocystis globosa* (microalgal species), and two types of  $\beta$ -chitin nanofibrils from a squid pen and a tubeworm respectively, show that both types of  $\beta$ -chitin nanofibrils exhibit similar strength

values of approximately 3 GPa, while for  $\alpha$ -chitin, the strength is 1.6 GPa.<sup>116</sup> Structural analysis reveals that the algal  $\alpha$ -chitin has a higher crystallinity compared to the two types of  $\beta$ -chitin tested, and also a circular cross-section, compared to a square and rectangular cross-section of the squid and tubeworm. Moreover, the  $\alpha$  phase has a denser hydrogen-bonding network. Surprisingly, these structural findings on crystallinity and hydrogen-bonding do not support the mechanical testing results. AFM measurements performed on  $\beta$ -chitin extracted from *Thalassiosira fluviatilis* report a modulus of 100–200 GPa.<sup>117</sup> Recent MD simulations provide further information on the different mechanical behaviors of the two phases, and predict an elastic modulus of 48 GPa for  $\alpha$ -chitin and 27 GPa for  $\beta$ -chitin,<sup>118</sup> which is in agreement with the denser hydrogen bonding of the  $\alpha$  phase. The inconsistencies between the predicted and experimentally measured elastic modulus of chitin, similarly to cellulose, highlight the need for further investigation on the mechanical behaviors of chitin polymorphs. The range of mechanical properties of  $\alpha$ - and  $\beta$  crystalline chitin, determined experimentally or through numerical simulations, are summarized in Table 4 and graphically in Figure 3.

#### *Mechanical properties of chitin-based cell walls*

The mechanical properties of filamentous fungal hyphae of *Aspergillus nidulans* were probed using AFM. Results

show that, in normal growth conditions and under turgor pressure, the hyphal cell wall (thickness of about 100 nm) has a  $110 \pm 10$  MPa elastic modulus, which is decreased to  $64 \pm 4$  MPa in conditions of high osmotic stress.<sup>119</sup> Tensile tests on *Saccharopolyspora erythraea* hyphae cells with a diameter of 370 nm, and cell wall thickness 25–30 nm, show an elastic modulus of 140 MPa and a strength of 24 MPa.<sup>120</sup> Similar tests on *Saccharomyces cerevisiae* yeast cells show an elastic modulus of 135–165 MPa and a strength of 66–74 MPa.<sup>121</sup> These data reported in literature show that the cell wall properties are far inferior to pure chitin fibrils, in the same way that cellulose-based cell walls or cellulose materials also perform lower than pure cellulose.<sup>68,69</sup> This stark difference in performance is related to (i) the presence of a compliant matrix of softer polymers in the cell walls which host the load bearing chitin fibers, and (ii) the presence of amorphous domains in the chitin fibers, which compared to the purely crystalline elemental fibrils have lower mechanical properties.

## 2.3 | Protein $\beta$ -sheet structures: Silk and amyloids

Proteins are complex 3-dimensional macromolecules composed of one or more long chains of amino acids called polypeptides. A protein is characterized by its structure at different levels. The primary structure is the amino acid sequence in a polypeptide chain. The secondary structure describes the folded geometry adopted by a single polypeptide chain, which is guided and held in place by hydrogen bonds due between atoms of the backbone. Common examples of secondary structures are  $\alpha$ -helices,  $\beta$ -sheets, and turns. The conformation of a polypeptide chain in the three-dimensional space corresponds to the tertiary structure of a protein. Finally, quaternary is the protein structure created from two or more smaller protein chains (subunits).

Among the variety of protein secondary structures,  $\beta$ -sheets have been the most extensively studied and demonstrate the highest mechanical properties.<sup>3,122,123</sup> An example of a well-studied  $\beta$ -sheet protein system is natural silk fibers, which are synthesized by spiders and silkworms. Amyloid fibers are structurally close to silks and are produced by some bacteria (e.g., *Escherichia coli*) as a key constituent of biofilms. Characteristically, in amyloids, the  $\beta$ -strands lie along a direction perpendicular to the fibril axis as well,<sup>124,125</sup> constituting the main structural difference between amyloids and silks (see Figure 5A). The main reason for the remarkable mechanical performance of  $\beta$ -sheet structures lies with the

TABLE 4 Properties of crystalline chitin.

Material	$E_A$ (GPa)	$\sigma_f$ (GPa)	Method	Reference
$\alpha$ -Chitin	41–59		XRD	112,115
	48		Modeling	118
		1.6	Cavitation	116
$\beta$ -Chitin	100–200		AFM	117
	27		Modeling	118
		3	Cavitation	116

hydrogen bonding between adjacent extended peptide strands. The vast distribution of weak hydrogen bonds result in a network of not only high load-bearing capacity but also with dynamic bond reforming capabilities, leading to high toughness.<sup>3,46,123,126</sup>

### 2.3.1 | Silk biosynthesis and macromolecular structure

The primary sources of silk fibers are silkworms, particularly *Bombyx mori*, and spiders. Silk is mainly composed of fibroin and sericins, while it also contains minor polypeptides (seroins) which do not contribute to the silk fiber structure<sup>127,128</sup> (see Figure 5C). In silkworms, silk proteins are synthesized in glands divided in three regions.<sup>129,130</sup> In the posterior section, a concentrated fibroin gel is synthesized and pushed into the middle silk gland section where it is enveloped by sericin proteins in a precise spatio-temporal pattern. As the silk dope is pushed through the anterior silk gland section, the shear forces and dehydration drive the fibroin solidification into a single thread. Two threads, one from each of the two labial glands, are aligned and merged into a fiber held together and coated by sericins, as they pass through the spinneret. The surface sericin layers are able to bind consecutive fiber layers together into the web, wall or other final structures.<sup>129,130</sup> In comparison, spider dragline silk fiber consists of a multitude of aligned nanofibrils that comprise a spider fibroin (also called “spidroin”) fiber core and is surrounded by protein, glycoprotein, and lipid layers<sup>131–133</sup> (see Figure 5B–D).

Silkworm fiber is about 10–20  $\mu\text{m}$  in diameter with the individual fibroin threads roughly half this fiber diameter. Each fibroin thread is made up of nanofibrils 20 nm in diameter.<sup>131,134</sup> By degumming the cocoon silk, the load-bearing fibroins are left without the embedding sericin, resulting in altered ultrastructure and properties, as will be discussed later in this section.<sup>127</sup> Spider dragline silk, on the other hand, is about 3–5  $\mu\text{m}$  in diameter.<sup>131</sup> Spidroins consist of several fibrils 400–650 nm in

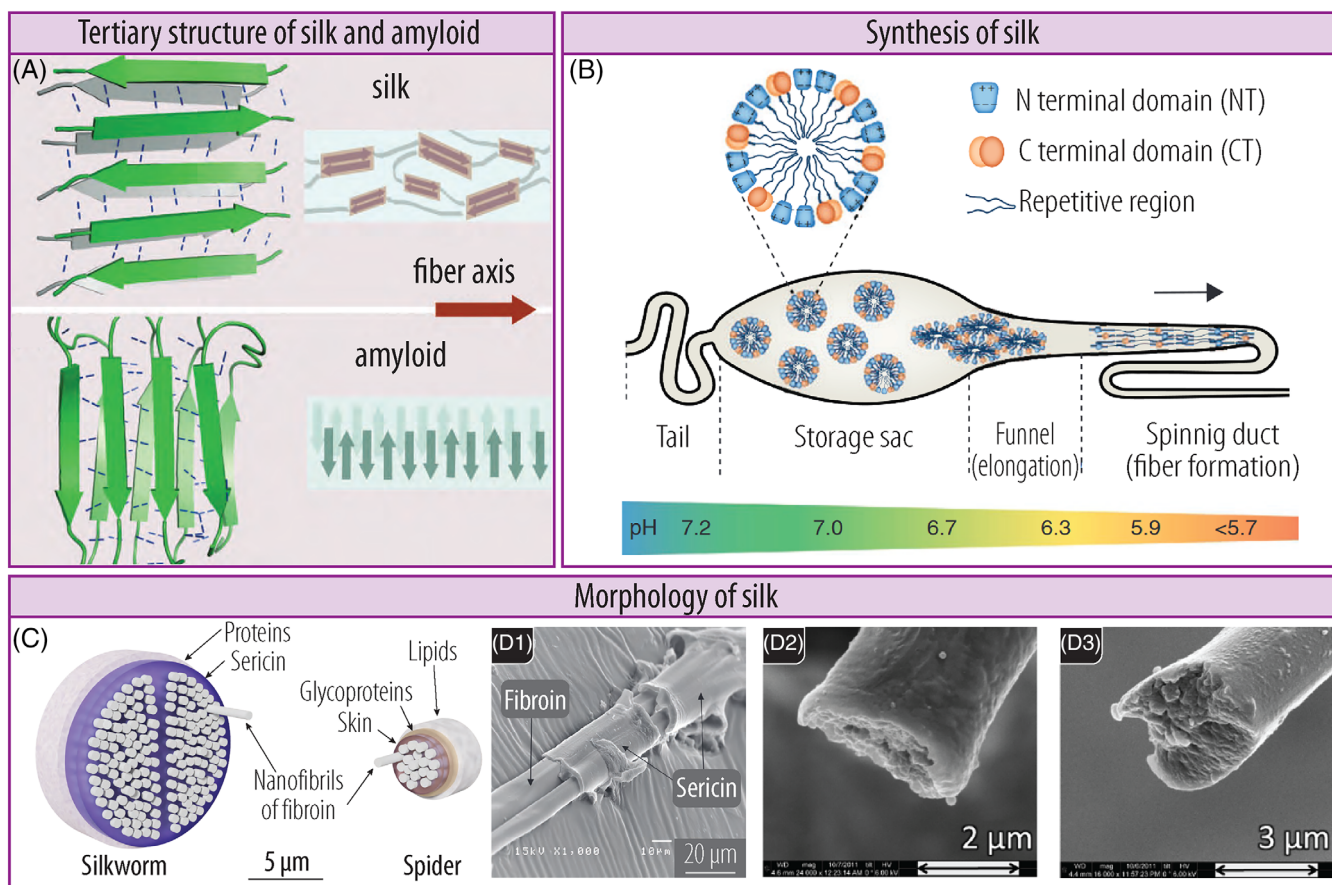


**FIGURE 5** Structure, synthesis, and morphology of protein  $\beta$ -sheet structures. (A) Orientations of silk and amyloid  $\beta$ -sheets. The same secondary structures are present in both, but are perpendicularly oriented. Reproduced from Reference 122 with permission from the Royal Society of Chemistry. (B) Overview of the silk glands of spiders. As the dope is processed, ions are exchanged and the pH drops, solidifying the dope into silk. Reproduced from Reference 133 (Creative commons. CC BY license). (C) Schematic representations of cross-sections depicting the hierarchical structure of a silk type produced by (left) silkworms and (right) spiders. (D1) SEM image of silk, revealing the fibroin and the sericin. Reproduced from Reference 137 Copyright 2016, with permission from Elsevier. (D2, D3) Micrographs of fractured silk fibers. Reproduced with permission from Reference 138 Copyright 2012 American Chemical Society.

diameter, themselves composed of smaller sub-fibrils of 200 nm diameter.

Within a single silk fibril, the crystal domains comprise of poly(Gly-Ala) and poly-Ala  $\beta$ -sheets stacked in antiparallel directions held together by hydrogen bonds.<sup>125,135</sup> The  $\beta$ -sheets form crystalline cores that are preferentially aligned parallel to the main fiber axis and are also held together by hydrogen bonds through side-chain interactions.<sup>125</sup> The ordered  $\beta$ -sheet domains are immersed in a semi-amorphous matrix that consists predominantly of less ordered structures including  $\alpha$ -helices, random coils and  $\beta$ -turns.<sup>122,136</sup> The protein chains in the amorphous domains are more mobile, primarily influencing extensibility of the natural nanocomposite system, while the ordered  $\beta$ -sheet crystals more strongly influence the stiffness and strength of the fibril. The  $\beta$ -sheet crystals are a few nanometers long and count for approximately 10%–15% of the fiber volume, but  $\beta$ -sheets are also found in the

less ordered domains for a total  $\beta$ -sheet content in excess of 50% in spider and silkworm silks.<sup>123</sup> The transition between highly ordered crystalline areas and disordered regions is not fully elucidated yet but it is considered to involve semicrystalline regions.<sup>125</sup> The two key differences between amyloid and silk fiber ultrastructure are the  $\beta$ -sheet orientation with respect to the fiber axis, which is parallel for silks versus perpendicular for amyloids, and the sub-optimal side-chain packing in amyloids.

### 2.3.2 | Amyloids biosynthesis and macromolecular structure

Amyloid fibers are protein assemblies folded into a cross- $\beta$ -sheet structure (Figure 5A). The repeat subunit of this structure is usually a soluble protein or a set of soluble proteins that changes conformation and becomes insoluble

upon assembly.<sup>139</sup> Assembled fibers consist of an extended network of repeating 3-dimensional  $\beta$ -sheet cores, stacked perpendicularly to the fiber axis and held together by hydrogen bonds through side-chain interactions.<sup>122</sup> Each sheet consists of hydrogen-bonded  $\beta$ -strands.

Amyloid fibrils are secreted by bacteria, alongside exopolysaccharides, into the extracellular matrix, where they play functional and structural roles in bacterial biofilms.<sup>139–141</sup> Transporters and protein channels move constituent proteins from inside of the cell to its surface where assembly is initiated. A natural example of such assembly occurs with biofilm associated proteins (BAPs) in *Staphylococcus aureus*. In this case, conformational changes inducing  $\beta$ -sheet formation and amyloid assembly occur under set conditions of pH and  $\text{Ca}^{2+}$  concentration.<sup>142,143</sup> The most commonly studied amyloids include Curli/CsgAB (*E. coli*), FapC family (*Pseudomonas* sp.), and TasA-TapA (*Bacillus subtilis*). In *E. coli*, the *csgDEFG* operon contains genes that regulate the production and transportation of the fiber proteins, and the *csgABC* operon expresses the CsgAB proteins which comprise the curli fibers.<sup>140</sup> CsgB is the nucleator protein upon which CsgA polymerizes. As a result, CsgA is the major component of curli fibers while CsgB is the minor component. In contrast, amyloids produced by *Pseudomonas* bacterial species are expressed from a single *fapABCDEFG* operon.<sup>139</sup> Like curli fibrils, fap fibrils comprise multiple components: majority FapC proteins with minor proportions of FapE and FapB.<sup>144</sup> In summary, amyloids usually consist of combinations of distinct proteins, present in uneven amounts, and are coded with other proteins that regulate their assembly.

From a functional perspective, amyloid fibrils act as “molecular glue,” enabling bacteria to adhere to surfaces and to each other and to bind metabolites and nutrients necessary for bacterial colony survival.<sup>144</sup> Structurally, they contribute to the physical framework of the biofilm and help to incorporate and stabilize exopolysaccharides and other components in a biofilm. The hierarchical structure of amyloids spans from the atomic and peptide scales ( $\leq 1$  nm) to the  $\beta$ -sheets ( $\sim 10$  nm) that they comprise, which in turn stack into fibrils ( $\sim 100$  nm) that coil into fibers ( $\sim 1$   $\mu\text{m}$ ) which subsequently form biofilm networks (sometimes referred to as plaques) that are macroscopically visible ( $>$  tens of  $\mu\text{m}$ ).

### 2.3.3 | Mechanical properties of silks and amyloids

Silk fibers have a larger axial strength than amyloid fibers, owing to the parallel alignment of  $\beta$ -sheets to the fiber axis and side-chain packing, which maximized

inter-chain hydrogen bonding.<sup>122,125</sup> However, amyloid fibers consist only of  $\beta$ -sheet crystals while, in silks, the  $\beta$ -sheets are immersed in a disordered matrix, which ultimately allows amyloid fibers to exhibit macroscopically the same stiffness as silks, around  $E_A = 10$  GPa.<sup>122</sup>

Experimentally, the mechanical properties of amyloid fibers are often approximated by testing the biofilms they compose. However, due to the multicomponent and heterogeneous nature of amyloids, there is a need to study the fibrils themselves to evaluate the contributions of each protein. A review meta-analyzed measured properties from various amyloid systems and reported that amyloid fibrils span Young's modulus values of 0.2–14 GPa and tensile strengths of 0.1–1.0 GPa.<sup>145</sup> Solar and Buehler performed atomistic MD simulations to shine light on the failure mechanism in amyloid proteins in six different secondary motifs.<sup>146</sup> They predict ultimate tensile strengths ranging from 242.6 to 917.0 MPa and show that this value is proportional to the number of hydrogen bonds broken per  $\text{nm}^2$ . In Table 5, we summarize mechanical properties of different types of amyloid fibers reported in literature.

Molecular dynamics simulations shedding more light into the outstanding toughness and strength of silk fibers demonstrate the impact of size effects in this hierarchical biomaterial system.<sup>123,147</sup> Studies show that when the  $\beta$ -sheet nanocrystals are sufficiently small, 3 nm identified as the critical crystal length dimension, they are stiffer and stronger as they are primarily loaded under uniform shear which utilizes their dominant hydrogen bonding planes<sup>123</sup> (Figure 5B). A stick-slip energy dissipation mechanism is observed, the same as later proposed for nanocellulose fibril assemblies<sup>46,126,148</sup> which is discussed in Section 3.1.2. According to that mechanism, after the initial rupture of the stacked  $\beta$ -sheet assembly, protein strands can slide and are able to reform hydrogen bonds with the neighboring sheets which, as an energy dissipation step, effectively toughening the nanocomposite. When the nanocrystals are larger, the main failure mode is bending, not shear, which creates crack-like flaws in the sheet assembly as the hydrogen bonding plane is non-uniformly loaded. This causes larger crystals to be softer and to fail at lower forces. The catastrophic failure upon further loading of the disrupted sheet assembly is due to dangling hydrogen bonds being accessed more easily by competing water molecules instead of neighboring  $\beta$ -sheets.

Patel et al.<sup>149</sup> used MD simulations to study the modulus, tensile strength, and yield strain of silk fibers with four different nanostructures under three strain rates. Results showed that modulus, tensile strength, and yield strain all increase with the strain rate. Under the strain rate of  $5 \times 10^9$  per second, a modulus of 6.4–7.4 GPa, a

TABLE 5 Comparison between silk and amyloid materials.

	Amyloid	Silk
Structure	$\beta$ -Sheets oriented along fibril axis, $\beta$ -strands oriented perpendicular to fibril axis	$\beta$ -Sheets oriented along fibril axis, $\beta$ -strands oriented parallel to fibril axis
Functionality	Structural support for biofilms, glue to stabilize components within composites (incl. biofilms). Genetic modification and fusion with other proteins possible between core subunits	Supercontraction phenomenon (i.e., full recovery of plastic strain possible)
Natural sources	Functional amyloids: Some species of bacteria. Pathological amyloids: Other proteins under specific conditions	Silkworm, spider
Composite combinations in literature	Biofilms, hydroxyapatite, silk, alginate, nanocarbons (graphene), inorganic nanoparticles (gold, titanium dioxide). See References 155,156	Silica, hydroxyapatite, biobased carbons, microalgae, alginate, collagen, elastin, keratin, amyloid-like proteins, sericin (gumming agent that bonds natural silk strands), nanocarbons (carbon nanotubes, graphene, graphene oxide), synthetic polymers (nylon, poly(vinyl alcohol), poly(acrylamide), poly(acrylonitrile), poly(ethylene oxide) and others). See References 151,157,158
Mechanical properties of fibers	$E = 0.2\text{--}14$ GPa $\sigma_f = 0.1\text{--}1$ MPa	$E = 7\text{--}20$ GPa $\sigma_f = 600\text{--}700$ MPa

tensile strength of 270–340 MPa, and a yield strain of 0.13–0.25 are predicted, which are in the range of experimental results.<sup>131,150,151</sup> Note that strain rate in MD simulation is usually much higher than experiment due to the time scale difference in the molecular simulation.<sup>152</sup> A further MD study by Patel et al.<sup>153</sup> focused on the mechanical properties of silk under different hydration levels (0–70 wt%). Results revealed that the hydrophobic effect has a dominating role at lower hydration levels resulting in an enhanced interaction between protein chains and mechanical strengthening. However, at higher hydration levels, the osmotic pressure plays a dominating role, resulting into screening of interatomic interaction between protein chains thus giving a weakening effect.

More insights into silk failure are provided by considering the balance between protein chain unfolding and stacked  $\beta$ -sheet separation, as determining factors of the fiber failure.<sup>147</sup> Specifically, calculations motivate the hypothesis of a two-stage deformation mechanism (see Figure 6B,C): (1) shear failure pulls the stacked  $\beta$ -sheets apart so that they form smaller nanocrystals (with a fewer number of stacked sheets) which demonstrate a higher strength and stiffness (require more energy to deform further<sup>123,154</sup>); (2) within a single  $\beta$ -sheet, chain unfolding requires a higher amount of energy than the first mechanism, and therefore appears as a secondary failure mode. These two modes are proposed in addition to the amorphous chain alignment in the more mobile regions of the silk fiber. The same publication also provides a strength-map

schematic, which shows the balance between optimized protein chain length within the  $\beta$ -sheet and amount of stacked sheets. Interestingly, the highest and lowest strength crystals appear rather close to each other in this map demonstrating the intricate interplay between the two structural factors on the final performance of the  $\beta$ -sheet crystal.

For the crystalline areas of  $\beta$ -sheet cores in silk, a modulus of 30–70 GPa has been reported. However, as seen in this section, silk fibers have a substantial amorphous matrix component that ultimately reduces the macroscopic mechanical properties, to such an extent that they reach the same modulus as amyloid fibers. The effects of sericin, at the mesoscale, coating and binding elemental silk fibers are also important. Experiments by Vepari and Kaplan showed a 15–17 GPa modulus for *B. mori* silk without sericin, versus 5–12 GPa in absence of sericin, and a tensile strength of 610–690 versus 500 MPa at the respective samples.<sup>127</sup>

A comparison between silks and amyloids is presented in Table 5 and their respective mechanical properties are reported in Figure 3.

### 3 | BIOPOLYMERS IN MATERIALS AND COMPOSITES

The main challenge when designing nanomaterials is to transfer or integrate their attractive properties into macroscopic materials. Typical physical interactions between nanomaterials lead to aggregates, entanglements or other

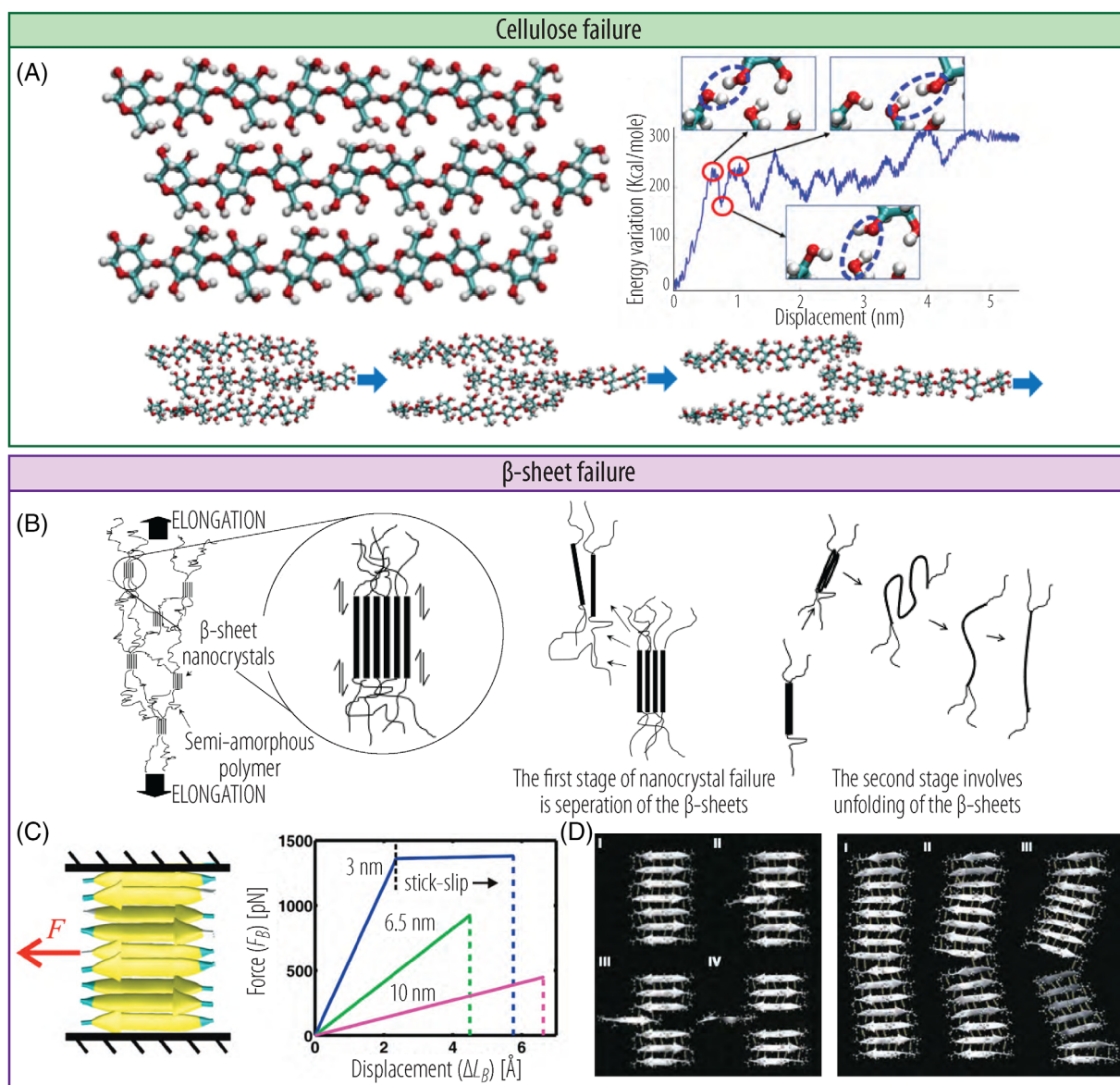


**FIGURE 6** Failure mechanisms in cellulose and silk. (A) Molecular dynamics simulations of a pull-out experiment of a cellulose chain. The dynamic breaking and reformation of hydrogen bonds is observed in the energy variation throughout the imposed displacement. Adapted from Reference 46. (B) Proposed cascade mechanism for the failure of a silk fiber under uniaxial tension. First, the  $\beta$ -sheets separate and subsequently unfold. Adapted from Reference 147 (Creative Commons Attribution 3.0 license). (C) Simulations of the transverse pull-out experiment in a  $\beta$ -sheet configuration. The fiber (of given length) is confined between two rigid plates and the pulling force is monitored throughout the displacement. For the longer fibers (6.5 and 10 nm), the fiber bends and snaps suddenly whereas for the shorter fiber (3 nm), the  $\beta$ -sheet is pulled out and the authors report a stick-slip behavior. Adapted with permission from Reference 154 Copyright 2010 American Chemical Society. (D) A more recent study of the molecular dynamic lateral loading experiment on a  $\beta$ -sheet fiber where the stick-slip behavior is also reported for short fibers (left) instead of the bending-induced snapping of longer fibers (right). Reproduced with permission from Reference 123.

types of bundles. Aggregation imposes difficulties in the controlled dispersion of nanomaterials which is a key requirement to achieve a macroscopic assembly with maximized filler-matrix interfaces. Increased dispersion leads to higher amount of available filler-matrix interfaces, which ultimately facilitate molecular-level interactions of the elemental building blocks. For example, for CNFs, the mechanical properties of the processed

macroscale materials show 3–15 times lower values compared to theoretical and experimental values of the corresponding single fibers.<sup>148</sup> In this section, we now discuss how the dispersion, orientation and bonding of biopolymers in the micro-scale allows controlling the macroscopic mechanical properties of biopolymer-assembled materials and their composites for cellulose-, chitin-, and protein  $\beta$ -sheet-based materials.



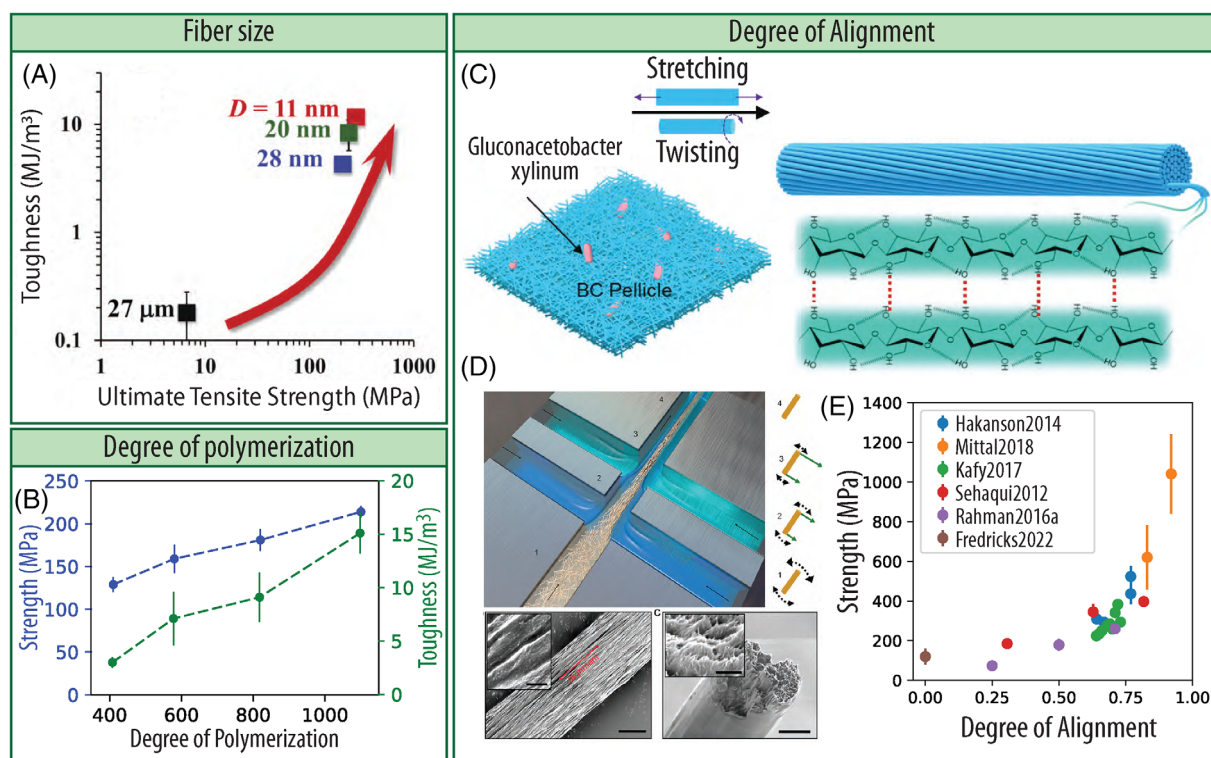


**FIGURE 7** Improving mechanical properties of cellulose-based materials. (A) Toughness and ultimate tensile strength of cellulose fibers both increase for decreasing fiber diameters,  $D$ . Reproduced from Reference 46. (B) Experimental characterization of strength and toughness for increasing degree of polymerization of cellulose. Data extracted from Reference 159. (C) Strategy to strengthen cellulose by aligning the fibers of bacterial cellulose through the stretching and twisting of pellicles. Adapted from Reference 160. (D) Hydrodynamic alignment of cellulose fibers in a liquid flow. Scale bars of the SEM snapshots, 3  $\mu\text{m}$  and insets are 400 nm. Adapted from Reference 148 (CC BY 4.0). (E) Strength of cellulose materials as a function of the degree of alignment of fibers based on literature data from References 148,161–165. Note that the degree of alignment of Kafy et al.<sup>162</sup> was interpolated from their reported order parameter using an empirical relation between order parameter and degree of alignment of Reference 163 as means of calibration.

### 3.1 | Cellulose-based materials

The remarkable combination of high strength and stiffness of individual cellulose fibrils has yet to be achieved by a macroscopic material composed of cellulose fibers. In this section, we describe examples of cellulose materials processed via various methods and assembled into nanopapers, microfibrils, hydrogels and aerogels. We show that these materials exhibit widely varying mechanical properties and we highlight the connections between structure and properties.

#### 3.1.1 | Effects of fiber diameter

A study by Zhu et al.<sup>46</sup> on pure cellulose nanopapers comprised of fibers with different diameters underline the remarkable size effects in the mechanical behavior of this material system. Specifically, tensile tests of isotropic papers obtained from soft-wood extracted, TEMPO and mechanically treated cellulose micro- and nano-fibrils of different diameters (11 nm, 28 nm, 27  $\mu\text{m}$ ) show a

staggering 40-fold increase of tensile strength, from 6.7 to 275.2 MPa, when decreasing the fiber diameter, from 27  $\mu\text{m}$  to 11 nm (see Figure 7A). Their results suggest that the increase in strength is inversely proportional to the square root of fiber diameter. In addition, decreasing fiber diameter increases the toughness almost 130-fold from 0.13 to 11.68  $\text{MJ m}^{-3}$ , and the fracture toughness over 10 times from 143.3 to 1481.4  $\text{J m}^{-2}$ . The reduced defect size due to nanoconfinement as the mechanism underlying this *smaller is stronger* behavior.

#### 3.1.2 | Molecular-level interactions controlling the mechanical properties of cellulose fiber assemblies

The exceptionally high toughness of cellulose fiber assemblies is proposed to arise from a molecular-level mechanism, supported by experiments and MD simulations,<sup>46</sup> similar to the mechanism proposed for silk fracture<sup>123,147</sup> (Section 2.3.3). The mechanism involves

concurrent hydrogen bond breakage and reformation events along with chain slippage and fracture during failure<sup>46,148</sup> (Figure 6A). Under tensile loading, the entangled chains of the CNF network align in the direction parallel to the applied force. As tension increases, the CNF fibers slide past each other and subsequently fracture, leading to ultimate failure. During chain sliding and fracture, some inter-chain hydrogen bonds break while others actively reform. Therefore, even if cellulose chains fail under tension, the reformation of hydrogen bonds keeps the fractured pieces bonded to neighboring chains.<sup>46</sup> MD simulations show that the number of hydrogen bonds (per unit area) remains constant as fibrils slide against each other during loading.<sup>148</sup> In conclusion, (i) active bond breaking and reforming and (ii) entangled chain unfolding are the two proposed mechanisms which result in a significant increase in energy dissipation, leading to the outstanding fracture toughness of all cellulose materials.<sup>46,148</sup>

The first mechanism (active bond breaking and reforming) has been theoretically confirmed by Meng et al.<sup>126</sup> The proposed multiscale crack-bridging model is based on cohesion of the interfaces between neighboring cellulose nanofibrils, connecting the hydrogen bonding interactions at the atomistic level to the bulk macroscopic properties at the fiber assembly level. This model confirms the experimentally observed relationships between the fracture toughness and fibril size (diameter and length) in cellulose nanopapers, as well as the proposed molecularly-controlled interactions governing the toughening. The predicted results show that smaller fibril diameter and larger length lead to more efficient crack resistance, and thus enhanced toughness (the lower and upper bounds for toughness are provided by this model). The smaller fibril diameter, for a fixed volume fraction of CNFs, will lead to larger amount of interfacial area and, as a result, increase the number of hydrogen bonds available for reformation, justifying the significant increase in the fracture toughness with reduced fibril diameter. On the other hand, the larger nanofibril length effectively leads to a bridging zone with higher length and a thus larger crack opening displacement (which enhances toughness).

Prior to these studies, AFM testing of isolated BC fibers with diameters ranging between 27 and 88 nm reported no change in the elastic modulus.<sup>63</sup> The shear forces were deemed unimportant and the nanofibers behaved like a homogeneous material in the nanoscale 3-point bending experiment that was conducted. Therefore, the aforementioned molecular-toughening observations and size-effects, which arise when *collective* or *assembled* cellulose fibril responses are probed in tension, were not detected in a single fiber nano-bending test.

### 3.1.3 | Effects of degree of polymerization

Studies correlating cellulose DoP with the macroscopic mechanical properties of cellulose papers show that at low DoP ranges, between 410 and 1100, at approximately the same film density, the DoP does not influence the elastic modulus of the produced film but does affect strength and toughness<sup>159</sup> (see Figure 7B). In the range 410–1110, DoP was found to increase the ultimate strength from 129 to 214 MPa and toughness from 3 to 15.1 MJ/m<sup>3</sup>. Because of this correlation, the failure mode is proposed to be chain slippage, rather than covalent bond breakage, which is expected at higher DoPs. This hypothesis traces back to the early fundamental work by Wainright et al.<sup>166</sup> which documents that cellulose fiber tensile strength increases with increasing molecular weight up to about 2500. For DoP > 2500, no correlation between DoP and tensile strength was reported, which suggests that below 2500 the overlap fibril length is shorter than a critical length and thus the fibers fail by chain slippage. Above that threshold, they yield by chain scission. Wainright et al. also highlighted that in natural cellulose materials (plant fibers), the DoP is several times greater than that critical value, indicating that in plant cellulose fibers, failure happens through chain rupture.

### 3.1.4 | Effects of modulating bacteria culturing conditions on the properties of bacterial cellulose

While in static culture, BC is produced in a pellicle form, in agitated cultures small, BC particles with spherical or ellipsoidal shapes are obtained.<sup>167</sup> In both cases, a network of random cellulose nanofibrils forms, with differences in the crystalline features and DoP of the produced cellulose.<sup>167–169</sup> We summarize the reported properties and culture conditions in Table 6.

Results on *K. xylinum* show that BC synthesized in agitated conditions exhibits lower degree of polymerization, crystallinity, and lower amount of I<sub>α</sub> phase in total when compared to statically-grown BC, which result in an overall lower elastic modulus.<sup>50,168–171</sup> The shear stresses exerted on bacteria during agitation have been proposed as an explanation for the lower degree of elemental-level ordering in BC. Moreover, the BC fibrils produced from agitated cultures are more entangled and more wavy compared to the more elongated fibrils obtained from static culture.<sup>50,169,171</sup> In cases of intensive agitation and aeration, cellulose synthesis may even be inhibited as spontaneous cellulose non-producing mutants have been detected.<sup>171</sup> Interestingly, there are reports of modified media (referred to as

**TABLE 6** Properties of bacterial cellulose (BC) depending on culture conditions (results are grouped by publication to enable a comparison unbiased by the measurement method).

Culture conditions	Young's modulus (GPa)	Strength (MPa)	DoP	Crystallinity (%)	I <sub>α</sub> (%)	I <sub>β</sub> (%)	Reference
Stationary				89	76	24	169
Agitated				84	71	29	
Stationary	2.6	34.1					170
Agitated	0.32	2.4					
Stationary	33.3		14,400	80	73		50
Agitated	28.3		10,900	72	61		
Stationary	2.7	92					171
Agitated	0.3	22.9					

Yamanaka-mannitol, Zhou-sucrose and Zhou-mannitol media by the authors) which allow pellicle formation even in agitated cultures, even reaching the same BC yield.<sup>168</sup> In these cases, a critical culture time was identified, following the initial BC spheres formation in agitated cultures, after which an uneven pellicle actually forms and connects the initial spheres together.

Strategies to alter the properties of BC by establishing a co-culture, or incorporating other biopolymer additives either during culture or after harvest have been reported.<sup>172–176</sup> Additives in the form of either glucose-based exopolysaccharides (EPSs) synthesized from *E. coli*<sup>172,174</sup> or hyaluronic acid (HA) synthesized from *Lactococcus lactis* (*L. lactis*),<sup>173,175</sup> when incorporated in BC either by being introduced with the culture media, or even when each of the bacterial strains were co-cultured with *Gluconacetobacter hansenii* (*G. hansenii*), show analogous effects on altering the mechanical properties of the biocomposites (though not numerically identical). Based on the reported data, we identify the following competing mechanisms governing the performance of the produced BC-composites: the biopolymer additives at small amounts cause an improvement in the mechanical properties of BC (stiffness and in some cases also strength<sup>172</sup>) by effectively de-clustering the cellulose fibrils as they lie in spaces between or on top of the fibril, thus promoting better fibril isolation. Furthermore, reports on additives increasing the fiber density and facilitating a closer packing between cellulose fibrils have been presented. Those effects are observed when the additive amount is kept below a certain threshold. Above a threshold value, the presence of additive biopolymers, begins to act as a stress concentrator, thus reducing the stiffness and load transfer abilities of BC, while causing a plasticizing effect (enhancing elongation to break).

In an elegant approach, Das et al.<sup>177</sup> utilized the symbiotic relationship between two unicellular organisms, *Acetobacter aceti* (*A. aceti*) bacteria and *Chlamydomonas*

*reinhardtii* (*C. reinhardtii*) microalgae, to create biocomposite biofilms. The ratios of each component were varied to optimize microalgae distribution and immobilization within the BC hydrogel matrix. The byproducts of (*C. reinhardtii*) metabolism enabled the incorporation of BC produced by (*A. aceti*) throughout the matrix instead of concentrating it at the air-medium interface, thereby creating homogeneous biofilms. In turn, the byproducts of BC synthesis were used as a carbon (nutrient) source for the microalgae enabling its survival. The symbiotic hydrogel has lower stiffness and strength compared to the pure BC biofilm produced by *A. aceti*. With no detectable differences in the crystal phases of cellulose between the two materials (though the degree of crystallinity was unreported), the lower performance of the composite can be associated with a lower concentration of cellulose compared to pure BC hydrogel, and the presence of algae in the BC pellicle creating large micron-sized aggregates between the cellulose fibers.

### 3.1.5 | Alignment effects in cellulose materials

As mentioned before (Section 3.1.2), an increased fibril alignment increases the surface contact area between neighboring fibrils, thus enhancing inter-chain bonding and ultimately, strength and modulus. In this section, we report methods that enable controlling the fibril alignment and therefore degree of orientation, which allows tuning of the macroscopic mechanical properties. A summary of literature on the strength of cellulose materials as a function of the degree of alignment (DoA) of their constituting fibers is proposed in Figure 7E. Note that the DoA is calculated from wide-angle X-ray diffraction (WAXD) data: 100% is perfectly perpendicular alignment to the beam and 0% is perfectly random alignment.

### Through hydrodynamics

Hydrodynamic alignment is a well studied method to improve significantly the CNF alignment within cellulose microfibrils. Hydrodynamic stresses generated from extensional flows can break up fibril aggregates more efficiently compared to shear flows.<sup>148</sup> Surface-charge-controlled gel transition in combination with hydrodynamically induced fibril alignment showed impressive results in controlling the CNF orientation into micrometer thick cellulose fibers<sup>148,161</sup> (Figure 7D). The proposed hybrid processing method that allows for this flow-focusing system<sup>161</sup> is mechanistically a two-part system: (1) hydrodynamic alignment of fibrils followed by (2) fixing fibrils in place by gel-transition. The hydrodynamic alignment part occurs in the direction of the flow causing the fibril alignment. A gel transition is induced to “freeze” the fibrils in place with lowered repulsion and better fibril alignment. Geometry-induced acceleration and deceleration, which are also used in spider spinners, allows, by a flow channel radius change, for fibril orientation along the perpendicular axis (in deceleration) or along the main flow channel axis (in acceleration).<sup>161</sup> As the microfiber diameter decreases from 38 to 28  $\mu\text{m}$ , there is an increase in the order parameter from 0.39 to 0.5 and consequently a 66% increase in strength and 38% increase in modulus<sup>161</sup> (from 290 to 495 MPa for strength and from 12.8 to 17.6 GPa for modulus). The introduction of a second set of focusing flow channels allows further control of the balance between fibril electrostatic repulsion and alignment due to supramolecular interactions.<sup>148</sup> This double flow focusing setup assembled the CNFs into highly aligned microfibrils (diameter about 7  $\mu\text{m}$ , degree of alignment 0.83–0.92, corresponding to an order parameter range of 0.53–0.72) and achieved remarkably high mechanical properties (elastic modulus 45–70 GPa and strength of 630–1200 MPa). Shorter (in length) fibrils experience a faster alignment and disorganization in that setup. However, they achieve lower mechanical properties (45 GPa modulus, 630 MPa strength) and the lowest fibril orientation degree of 0.83. When CNF length increases from 390 to 600–700 nm, the orientation index is maximized (0.92) as are the stiffness and strength (elastic modulus about 70 GPa and strength of 1200 MPa). Further, preconditioning the fibrils in low humidity conditions (14% vs. 50% RH) increases more the obtained properties which reach 82 GPa and 1320 MPa for modulus and strength, respectively, at a cost of strain to break which was reduced more than 50%. The improvement of stiffness and strength at a cost of elongation to break at lower humidity conditions has been observed in many cases. The strengthening of interfibrillar interactions is promoted by the removal of water molecules from the inter-fibrillar space thus freeing up more

hydroxyl groups for inter-chain interactions. At the same time, water works as a plasticizer between cellulose chains, thus facilitating larger deformations. Finally, chemical cross-linking of the fibers (with 1,2,3,4-butane tetracarboxylic acid or BTCA) was also found to improve the strength (not the stiffness) reaching a remarkable 1430 MPa, as it improves the connectivity and load transfer between the cross-linked chains. The deformation behavior follows the same molecular model described in Section 3.1.2, with high toughness stemming from hydrogen bond breakage and reformation.

### Through spinning

Wet and dry spinning have also been explored to create microfibrils from CNFs<sup>160,162,178–180</sup> with significantly lower mechanical property improvements compared to hydrodynamically-aligned microfibrils.<sup>148,161</sup> Dry spinning of CNFs with diameters between 8 and 35 nm,<sup>179</sup> results in microfibrils with orientation indexes of 0.62–0.68, in no particular correlation to the fiber diameter, which at best have an elastic modulus of 12.6 GPa and a strength of 222 MPa (at the smallest fiber diameter of 154  $\mu\text{m}$ ).<sup>179</sup> Wet spinning CNFs from wood pulp and tunicates having different aspect ratios, 2 nm diameter and 200–500 nm length for the wood-CNF and  $>10 \mu\text{m}$  length and  $8 \times 20 \text{ nm}$  cross section for the tunicate-CNF followed by heated drying under weak tension (undefined amount), leads to more significant changes in structure and properties of the fibers.<sup>178</sup> In the case of thin and short CNFs (from wood) the modulus and strength increase significantly as the degree of alignment increases (at higher spinning rates) with simultaneous (small) increase on the elongation to break. Increases as high as 180% on Young's modulus and 168% on strength (corresponding to 23.6 GPa and 321 MPa, respectively, at an orientation index of 0.72) are noted for the fibers with highest orientation index. On the other hand, the long and thick CNFs exhibit a non-significant change in their mechanical performance in response to a change in their orientation. The thin and short CNF fibrils “respond” to the spinning rate with significant improvements in alignment, stiffness, strength and toughness, for the same reasons mentioned previously—more enhanced interfibrillar interactions. The longer and thicker CNFs are not able to follow the same trends. Even if their alignment is improved with higher spinning rates, it is not enough to affect fibrillar bonding substantially to get observable differences in the mechanical properties.

When spinning is followed by a 5%–10% wet stretching of the CNF-spun microfibrils,<sup>162</sup> the degree of orientation can be improved (0.6–0.73) and higher modulus and strength values can be achieved (13–23.9 GPa and 224–383 MPa, respectively). The higher spinning speed and

drawing ratio lead to the stiffest and strongest fibers, albeit the least extensible ones since the strain at break is reduced with increased degree of alignment. The application of spinning and stretching in cellulose fibrils of short length (below 1  $\mu\text{m}$ , which is smaller than for example to the microfibers made by Wang et al.<sup>160</sup>), together with the fact that pre-stretching un-entangles CNFs, justify the decrease in elongation to break upon stretching. The CNF un-entanglement, on the one hand, improves their hydrogen bonding interactions, so strength and stiffness increase, but when subsequently stretched, there is less chain unfolding available for future energy dissipation upon loading, thus fiber fracture occurs earlier. In a variation to the above method, when wet spinning in a coagulation bath is followed by stretching in a humidified chamber instead of a solution,<sup>180</sup> larger drawing ratios are possible. A 10%–20% stretch gradually improves the degree of alignment (from 0.77 to 0.86), while simultaneously improving the modulus from 24.3 to 37.5 GPa and strength 492 to 543 MPa, at a cost of strain to break (12%–3.7%). The same study confirms that there is an optimum spinning speed as the maximum attempted (2310 cm/min) actually reported less stiff and strong and more ductile fibers compared to fibers spun at lower speeds.

#### *Through templated growth of bacteria*

Another way to control the cellulose fiber alignment in the case of BC is by utilizing bacterial adhesion and movement along patterned substrates.<sup>164,181–184</sup> Examples of patterned substrates with hexagonal,<sup>181</sup> ridged<sup>182</sup> and linear repeating groove<sup>164,183</sup> shapes have been proven to result in BC membranes templated in the shape of the substrate. Experiments with concave honeycomb scaffolds<sup>181</sup> show no BC on the top of the walls, regardless of the scaffold material, and bacteria populating the edges of the walls, indicating that bacterial movement is physically constrained. The dimensions of the scaffold path along which the bacteria are intended to align are also critical in ridged substrates, with a ridge size of 4.5  $\mu\text{m}$  (equal to the length of the tested *K. xylinus* cells) producing films with the highest degree of orientation for *K. xylinus*.<sup>182</sup> The patterned membranes produced from substrates with that critical ridge size outperform unoriented membranes (produced on a flat substrate) in strain to and strength at failure (by about 2 and 2.3 times higher values respectively).<sup>182</sup>

Substrates patterned with linear grooves show that the well width can cause BC alignment effectively as long as the well depth was at least 0.6  $\mu\text{m}$ , below which there was no preferred alignment.<sup>183</sup> Substrates with a wavelength of 2  $\mu\text{m}$  and depth of 1  $\mu\text{m}$  show the maximum degree of BC alignment along the wells, yet the

mechanical properties of the aligned films showed a non-statistically significant difference compared to those of the randomly oriented BC when tested in the principal alignment direction, indicating that better alignment did not lead to mechanically superior substrates.<sup>183</sup> In contrast, the same geometry (rectangular parallel wells), when scaled in larger dimensions of 2 mm width and 1 mm depth, was able to deliver aligned BC films with significantly enhanced properties compared to unoriented BC films.<sup>164</sup> The patterned BC sample shows a 230% improvement in Young's modulus (10.9 GPa) and 144% improvement in tensile strength (179 MPa) along the aligned direction compared to the pellicle (3.3 GPa and 73 MPa, respectively).<sup>164</sup> A promising and effective patterning approach for BC alignment along a wrinkled substrate, with a wavelength of about 1  $\mu\text{m}$  and about 300 nm height, shows significantly improved tensile strength and modulus, 178 MPa and 4.6 GPa versus 97 MPa and 2.5 GPa for the wrinkled versus flat-templated BC.<sup>185</sup> The wrinkled patterning also leads to a higher degree of crystallinity in the BC, which supports the film's superior stiffness and strength. The mechanical performances of aligned BC films are summarized in Table 7.

#### *Through stretching*

Wet-stretching cellulose nanopapers, hydrogels, pellicles or fibers has been used either in conjunction to other processing methods,<sup>162,180</sup> as seen in the previous section, or as a standalone method<sup>160,163,186</sup> to control cellulose fiber orientation. Wet-stretching CNF hydrogels by 20%, 40%, and 60% improves the fibril alignment drastically from 30% to almost 82% (in plane).<sup>163</sup> Stiffness and strength also increase significantly, in a monotonous trend with draw-ratio, while the strain to failure progressively decreases. The maximum improvements are over 220% in modulus, and 110% in strength, reaching 33.3 GPa and 428 MPa, respectively. The elongation to break was reduced by 65%, from 5.3% to 1.8%.

The record high in terms of strength of a cellulose nanopaper<sup>186</sup> and stiffness of cellulose macro-fiber<sup>160</sup> are achieved from wet-stretching induced alignment on BC fibers (see Figure 7C). A 40% stretching degree of BC pellicles, without damaging the cellulose fibril network, is achieved by introducing an intermediate relaxation step following the initial 20% pre-stretching.<sup>186</sup> This work reports a progressive increase in the degree of fibril alignment with the degree of stretching (qualitative dependence). Subsequently, the elastic modulus also increases progressively from 11.4 to 18.1 GPa, and the tensile strength reaches a groundbreaking 1 GPa of strength, starting from almost 195 MPa in the non-stretched nanopaper. The elongation at break is almost not affected,

TABLE 7 Effects of templated growth and wet-stretching on the mechanical properties of bacterial cellulose pellicles.

Material	Through-plane DoA (%)	In-plane DoA (%)	Young's modulus (GPa)	Max tensile stress at break (MPa)	Reference
Unstretched, statically-grown BC	25, 29, 29	36, 38, 38	3.3, 3.2, 3.0	73.2, 71.3, 70	164,187,188
Unstretched BC-SPI	–	–	1.9, 2.0	40.0, 40	187,188
Stretched, statically-grown BC	63	71	6.5	132.0	187
Stretched BC-SPI	–	–	3.6	66.3	187
Unstretched BC array	50	62	10.9	178.6	164
Stretched BC array	71	85	16.8	260.4	164
Unstretched TBC	48	58	8.0	155	188
	–	–	$2 \times 10^{-5}$	0.59	184
Stretched TBC	68	82	13.0	230	188
Unstretched TBC-SPI	–	–	4.0	95	188
Stretched TBC-SPI	–	–	8.0	150	188

Abbreviations: BC-SPI, soy protein isolate resin-impregnated BC pellicle; DoA, degree of alignment, calculated from WAXD data using  $\frac{180 - \text{FWHM}}{180} \times 100$ , where 100% is perfectly perpendicular alignment to the beam and 0% is perfectly random alignment; TBC, tubular bacterial cellulose.

while the nanopaper density increases from 0.64 to 1.18 g/cm<sup>3</sup> for the 40% stretched nanopaper. This performance surpasses CNF-hydrodynamically aligned microfibrils and previously reported wet-stretched CNF nanopapers in terms of strength (428 MPa,<sup>163</sup> and 490 MPa<sup>161</sup>) which may be associated with the higher aspect ratio of BC fibrils. Combining wet-drawing to reach extensions of up to 30% with twisting them, enables the fabrication of micron-thick but macroscopically long fibers with a high degree of cellulose alignment (index not reported), and the record high tensile strength (826 MPa) and Young's modulus (65.7 GPa) for cellulose microfiber materials.<sup>160</sup> The significant effects of stretching are clearly illustrated by comparing the properties of unstretched fibrils (modulus of 3.5 GPa and strength of 115 MPa), which are almost 19 and 7 times lower compared to the stretched fibrils respectively.

#### Through electrokinetics

A less studied approach to control the growth and orientation of BC during the culturing period involves the use of electric fields.<sup>189,190</sup> Electrokinetic forces capable of influencing cell movement, as demonstrated in the case of *K. xylinum*, are able to produce BC pellicles with increased degree of alignment compared to control samples cultured in absence of external fields.<sup>189</sup> Experiments in static cultures show that the cell movement velocity is influenced by the applied field, and when the cell speeds are greater than the cellulose production speeds, the produced BC shows better degrees of fibril alignment. Moreover, the same study identifies an upper limit to the applied electric field (0.45 V/cm), above which cellulose production ceases. On the other hand, alternative current

(AC) external fields above a specific threshold (600 V) in conjunction to a double flow focusing hydrodynamic alignment setup are able to enhance orientation of CNFs by 16% which leads to a modulus improvement from 20 to 25 GPa, a 63% increase in tensile strength (reaching 260 MPa), and a 46% increase in elongation to break (up to 2.8%).

#### 3.1.6 | Effects of crosslinking

Introducing physical or chemical crosslinks is another effective way to modulate the mechanical properties of cellulose-based materials, and has been achieved using synthetic polymers,<sup>191–194</sup> biomolecules or biofibers,<sup>187,188,195–197</sup> ions (monovalent or multivalent metal ions, such as Ag, Ca, Zn, Cu, Ca, Na, Fe<sup>198–201</sup>) among others, as crosslinking agents. Polymers like polyethylene glycol diacrylate (PEGDA), polyethylene glycol (PEG),<sup>191</sup> polyacrylamide,<sup>192</sup> glyoxal,<sup>202</sup> gelatin fibers,<sup>195–197</sup> and proteins,<sup>187,188</sup> have been explored extensively in literature to crosslink cellulose-based scaffolds, pellicles and hydrogels. In general, there is a positive correlation between increasing degree of crosslinking and obtained mechanical properties (primarily compressive properties are tested)<sup>191–194,198,199</sup> in physical, chemical and hybrid (double networks) crosslinked cellulose materials. The improved compressive strength and modulus are coupled with a decrease in strain to break indicated in the embrittlement of the hydrogels.<sup>191,194,197,203</sup>

A study of the effectiveness of ions with different valence states in crosslinking 2,2,6,6-tetramethylpiperidinyloxy (TEMPO)-oxidized (charged) cellulose, shows that trivalent

cross-linking leads to better bonding and higher mechanical properties compared to divalent ion cross-linking.<sup>201</sup> Specifically, Fe<sup>3+</sup>-crosslinked cellulose fibers show an elastic modulus of 22.9 GPa and a tensile strength of 357.5 MPa, while Cu<sup>2+</sup> cross-linking leads to a modulus of 20.2 GPa and a strength of 317 MPa and Na<sup>+</sup> leads to a modulus of 16.4 GPa and a strength of about 250 MPa, respectively. Comparing to monovalent or divalent cations, ions with three valence electrons experience higher electrostatic force from the charged surface groups of cellulose fibrils. Therefore, the higher inter-fibrillar interactions in presence of the trivalent ions give rise to the highest mechanical properties.

The effects of covalent crosslinking are more pronounced in the wet-tested BC samples, compared to dry-tested BC, when glyoxalization was applied as a case study.<sup>202</sup> Specifically, while glyoxalized BC has an unaffected degree of crystallinity and crystal morphology compared to the control BC, it has a higher elastic modulus, 6.1 compared to 1.9 GPa of the control, and tensile strength, 76.8 versus 10 MPa, in the wet-tested samples, at a cost of extensibility as the strain to break is reduced from 9.3% to 1.5%. In the dried samples, there is a non-significant difference between the moduli of the cross-linked and non-crosslinked BC, while there is a clear embrittlement upon glyoxalization, as evident from a drastic reduction in strength and toughness. Thus, the effective covalent crosslinking, at the dry state embrittles cellulose by occupying hydroxyl bonds that otherwise would be free to interact with themselves, but in the wet state it actually preserves the (reduced compared to dry) load-transfer abilities of bonded cellulose chains, thereby reducing the negative impact of the presence of water on the material.

Some studies focus on creating an “artificial plant cell wall” paper, with BC embedded in matrix of hemicelluloses and pectin, which are the natural binders in plant cell walls, but as expected, the properties achieved are far from comparable to pure BC or pure cellulose extracted from plant/wood nanopapers. Gu and Catchmark<sup>204</sup> introduced xyloglucan and pectin in the culture media of *G. xylinus* and report that compared to pure BC films, the “cell wall” composite in which the added polysaccharides were uptaken and incorporated in the BC pellicle, have lower elastic modulus and strength. The composites with xyloglucan show the lowest modulus, strength and strain to break. The “cell wall” composites have lower crystallinity and the crystal size compared to pure BC. The presence of xyloglucan and pectin decreases the cellulose node density, hindering cellulose inter-chain bonding, thus weakening the composite. Other papers also report a decrease in stiffness and strength but improvement of extensibility of the BC/pectin and/or hemicellulose.<sup>205–207</sup> Conflicting results reported by Dayal and Catchmark<sup>208</sup>

who found that introducing pectin to the media of *G. xylinus* improves the mechanical properties of the pellicle, while maintaining the same degree of crystallinity but a reduced crystal size. However, in this study, the hydrogel's wet properties were tested in contrast to the previously mentioned results, which were all from dried BC films. The hydrogel elastic modulus improved from 7.6 to 16.7 MPa when 1 wt% pectin was added to the growth medium, and the compressive modulus from 7.4 to ~140 kPa in the 3 wt% added pectin in the medium.

### 3.1.7 | Effects of humidity

In presence of water molecules, the hydrogen bonds between cellulose chains are reduced as water molecules occupy the pendant hydroxyl groups of CNFs, while a plasticizing effect is also observed allowing extended deformations to the polymer chain before failure.<sup>148</sup> The elastic modulus can vary from 20 to 0.7 GPa, the tensile strength from 360 to 5 MPa, both over an order of magnitude reductions, for dry versus wet CNF nanopaper, with the strain to break affected only in the case of samples being soaked in water.<sup>209</sup> The transition in the mechanical behavior of cellulose nanopaper from linear elastic with a brittle failure in the dry state, to predominantly plastic with a fibrillar pull-out as a consequence of poor inter-fibrillar interactions in the hydrated state, is clearly observed.<sup>209</sup> The amorphous regions are more prone to water-induced plasticizing effects, since water diffuses in these areas more easily than in crystalline regions. The hydrogen bonding network disruption and lower friction among cellulose fibers as a consequence of the presence of water between them, are the main reasons for the observed stiffness and strength deterioration. In addition, the swelling of the material in presence of water reduces the film density and the contact points between fibrils, thus reducing the load transfer capabilities.

### 3.1.8 | Effects of hot-pressing

Applying heat and pressure on cellulose membranes enables their densification, thereby increasing stiffness and strength. For example, Fredricks et al.<sup>165</sup> studied the effect of hot-pressing bacterial cellulose in the presence and in the absence of lignin as an additive. At the optimal pressing conditions (temperature 120°C, pressure 5 MPa for 20 min), the pure cellulose sheet reached an ultimate tensile strength of 190 MPa, at a density of 1.3 g/cm<sup>3</sup>. The authors proposed a path to further enhance mechanical properties by impregnating the BC mats with lignin. At optimal pressing conditions (temperature 120°C,

pressure 15 MPa for 30 min), the resulting composite sheets had ultimate tensile strength 220 MPa with a higher density, 1.9 g/cm<sup>3</sup>. The authors hypothesized that lignin acts as a binder, enabling the load transfer between the structural cellulose fibers. This mechanical improvement required more extreme pressing conditions (by either increasing the temperature, pressure, or pressing time) to ensure lignin bonding. Hot-pressing layered BC was also proposed by Guan et al.<sup>210</sup> to fabricate large cellulose-nanofibril plates (thickness in the cm scale with width and length in the tens of cm scale). Using three-point bending tests, the authors reported a flexural modulus in the range 13–16 GPa and strength 200–250 MPa depending on treatment, at a density of 1.35 g/cm<sup>3</sup>. These layered plates show remarkable machinability, as well as attractive specific impact toughness of 67 kJ m<sup>-2</sup>/(g cm<sup>-3</sup>).

### 3.2 | Chitin-based materials

After discussing cellulose-based materials, we now focus on chitin-based materials. We describe the structure and properties of nanopapers obtained from chitin fibrils extracted from crabs, prawns, lobster, squid, tubeworms and mushrooms. Typically, the mechanical properties for chitinous materials range between 0.2 and 7 GPa for Young's modulus, and between 30 and 200 MPa for strength.

#### 3.2.1 | Effects of chemical treatments and degree of acetylation

In a native state, the amine groups of chitin chains are partially de-acetylated.<sup>103</sup> Complete de-acetylation transforms chitin into chitosan. This critical molecular difference has major effects in the structure and properties of the chitin and chitosan (see Figure 8A). The acetyl group in chitin's macromolecular backbone provides hydrophobicity, while the remaining amino groups in chitosan are more charged. Consequently, as chitosan lacks the hydrophobic acetyl group of chitin, it is soluble in aqueous media, when chitin remains insoluble.

Studies on  $\beta$ -chitin films from squid pens report a general trend for high degrees of acetylation resulting in stiffer and stronger papers, while reducing degrees of acetylation allow more extensibility.<sup>215,216</sup> Specifically, high acetylation degrees (83%–89%) result in Young's modulus values between 200 and 300 MPa, and tensile strength 15–17 MPa.<sup>215</sup>  $\beta$ -Chitin fibrils dissolved in hexafluoroisopropanol show the same trends with respect to degree of acetylation, with different numerical values—

2.5 GPa elastic modulus and 150 MPa tensile strength for the acetylated sample, which are reduced to 0.9 GPa and 60 MPa, respectively after deacetylation.<sup>216</sup>

#### 3.2.2 | Effects of the presence of other native cell wall components in chitin nanopapers

Chitin fibers from crustaceans (*Homarus americanus*) when processed with a mild treatment<sup>217</sup> that allows retaining 4.7%–12.4% of native proteins along with the very high aspect ratio of chitin nanofibers (thickness 3.6–3.9 nm, length 1.0–1.5  $\mu$ m), produce nanocomposite films with a very high degree of acetylation (86%) and a very high degree of crystallinity 90%. The obtained films have densities between 1.09 and 1.21 g/cm<sup>3</sup>, elastic modulus between 7.3 and 8.3 GPa, tensile strength 110–153 MPa and a strain to break 4%–8%. Increasing protein concentration correlates to samples with lower ultimate strength and deformability while the elastic modulus is not affected by protein amount changes. Therefore, the lowest protein amounts facilitate more effective transfer loading to chitin nanofibrils (higher strength) and act as plasticizers to enable chain movement during loading, but when they exist in higher concentration they hinder load transfer (weaker composites) and failure happens at lower deformations.

Studies on retaining native cell wall glucans along with ChNFs in two different model systems, a crab (*Cancer pagurus*), and a mushroom (*Agaricus bisporus*, *A. bisporus*), elucidate the roles of glucans in such composites in a study by Wan Nawawi et al.<sup>211</sup> (see Figure 8B). *C. pagurus* extracts provide a high chitin/glucan ratio (in fact it lacks glucans), while fungal-extracts from *A. bisporus* stalk have a 50/50 ratio and extracts from *A. bisporus* cap have a 35/65 ratio. Samples from mushroom extracts (either stalks or caps) result in composites with the maximum density, strength, modulus and elongation to break (and subsequently toughness too). The samples with no glucans, from *C. pagurus*, have the lowest density, stiffness, strength and toughness. The amorphous glucan phase serves as a binder for the ChNFs—just as it does in the native state—thus enabling exceptional tensile strength and modulus of the composite films which in the case of 50%–65% glucans in ChNFs reach 200 MPa and 7 GPa, respectively. The presence of amorphous glucans leads also to a substantially lower degree of crystallinity, around 65% as opposed to the chitin samples, which have 85% crystallinity. This contrast of having composite samples with lower crystallinity but higher mechanical properties compared to more crystalline pure chitin nanopapers, suggests that having the glucans in an “optimum” amount to serve as plasticizers and



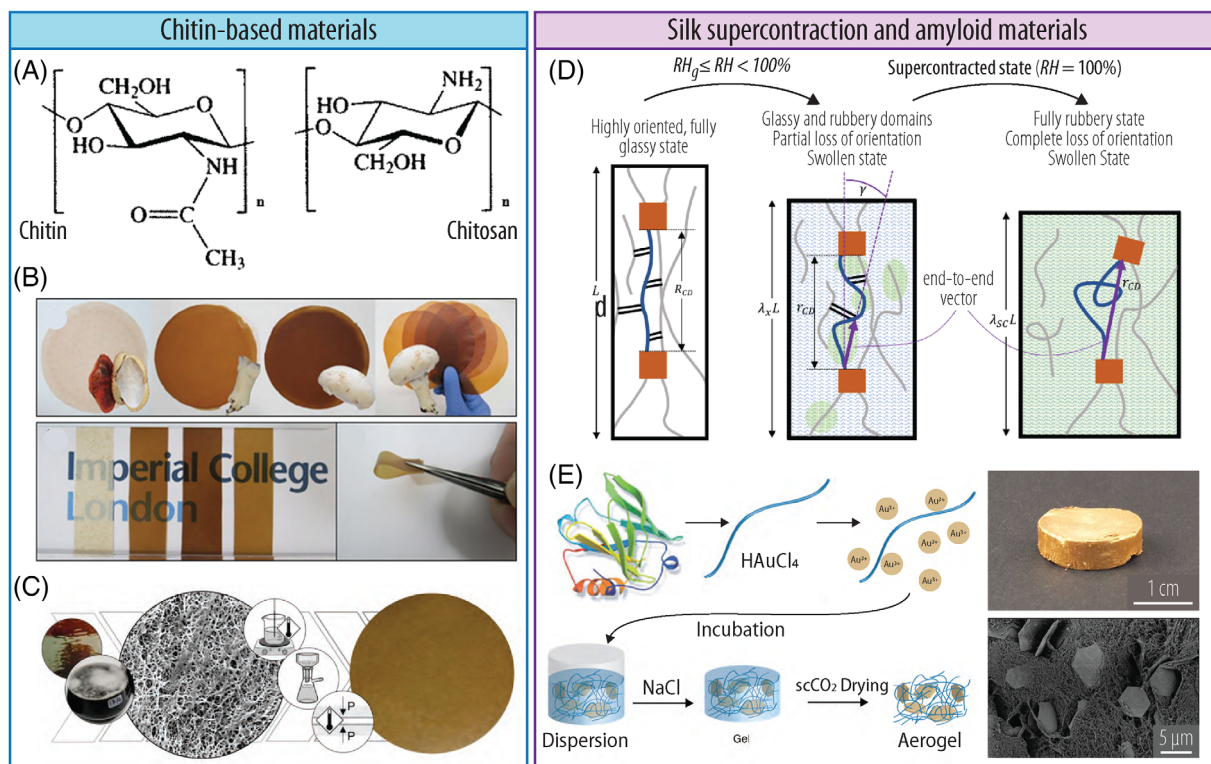


**FIGURE 8** Materials using chitin and protein  $\beta$ -sheet structures. (A) Molecular structure of chitin (left) and chitosan (right). Reproduced from Reference 103 Copyright 2006, with permission from Elsevier. (B) Chitin nanopapers produced from mushroom extract. Reproduced from Reference 211 (Creative commons CC BY). (C) Chitinous nanopapers using waste-derived mycelium. Reprinted with permission from Reference 212 Copyright 2019 American Chemical Society. (D) Mechanism responsible for the supercontraction of silk under saturated humidity conditions. Reprinted with permission from Reference 213 Copyright 2021 American Chemical Society. (E) Example of amyloid-based functional material where gold nanoflakes are embedded in an amyloid aerogel. Adapted from Reference 214.

crosslinking agents promotes load transfer, as seen in the example discussed above that involved proteins instead of glucans.<sup>217</sup>

Jones et al.<sup>212</sup> studied the mechanical properties of nanopapers obtained through by hot-pressing different fungal sources (see Figure 8C). Specifically, the contributions from glucans, chitosan and ChNFs were studied using four different model fungal systems: *Trametes versicolor* (*T. versicolor*) composed primarily of chitosan and glucan fibrils, *Allomyces arbuscula* (*A. arbuscula*) with slightly higher chitin content but lower glucans amount and only 2.3% chitosan, *Mucor genevensis* (*M. genevensis*), containing higher chitin content and 10% chitosan, and *A. bisporus* with maximum amount of chitosan and chitin as well as the second maximum glucans amount (*T. versicolor* has the maximum glucans amount).<sup>212</sup> Nanopapers of *A. bisporus* show the highest tensile strength and modulus from all prepared materials, at a density of  $1.7 \text{ g/cm}^3$ , they have a Young's modulus of 6.5 GPa and a strength of 98 MPa. These nanopapers have the highest amount of chitin and chitosan (30.8% and 11.5% of the sugars, respectively) but relatively high amount of

glucans, as well and a low, compared to other tested nanopapers, degree of acetylation (72.8%). *M. genevensis* nanopapers have the second highest strength (24.7 MPa) and they share the same elastic modulus of 1.9 GPa, low density ( $1.3\text{--}1.4 \text{ g/cm}^3$ ) and glucans content with nanopapers from *A. arbuscula*. *M. genevensis* nanopapers have a slightly higher chitin content compared to *A. arbuscula* but also higher overall chitosan amount, which may account for their difference in strength compared to *A. arbuscula*. Both *M. genevensis* and *A. arbuscula* nanopapers are over 2 times stiffer compared to *T. versicolor* nanopapers, and their strength, which ranges between 14 and 25 MPa, is 16–27 times higher. Interestingly the latter presents the lowest stiffness, strength and strain to break values at the maximum density ( $2.0 \text{ g/cm}^3$ ) out of all discussed nanopapers of that report. However, the biomatter of *T. versicolor* presents the lowest chitin and highest glucans content out of all the tested samples. From the presented sugar analysis results, there is a positive correlation between the total amount of chitin and chitosan (collectively) and the obtained mechanical properties of the nanopapers. There appears to be a delicate

balance between the glucans and chitin/chitosan amounts when optimizing for strength and stiffness. Indeed, there is a threshold for glucans concentration below which they act as plasticizers and crosslinking agents (seen also in Reference 211), but for higher values, glucans hinder chitin/chitosan chain interactions, thereby negatively affecting the mechanical properties of the composite films. Note that the actual numerical value of that threshold cannot be defined by the very limited existing literature.

### 3.3 | Protein $\beta$ -sheet structure-based materials and composites

The attractive properties of silks and amyloid fibers have been leveraged to design functional macroscopic materials. In this section, we review some of the methods to tune and take advantage of these protein building blocks. Namely, we focus on the effects of drawing and supercontraction, the effect of temperature and humidity, and, finally, we review some of the recent work on amyloid composites.

#### 3.3.1 | Effects of drawing and supercontraction

A common method to process silk materials under artificial conditions is wet-spinning, whereby a dope or suspension of silk fibroin is extruded through a small opening through coagulating or stabilizing baths. Wet-spinning mimics the natural process by which silkworms or spiders produce silk fibers. However, extruded fibers can be additionally processed in a wet-spinning set-up to modify their properties. One such additional processing step is post-drawing the produced fibers in solution.<sup>218,219</sup> Luo et al.<sup>218</sup> showed that drawing fibers from a regenerated silk fibroin (RSF) suspension by a factor of 2, dramatically changes their secondary structure. A clear conformational transition from the disordered random coil,  $\alpha$ -helix and intermediate states to ordered  $\beta$ -sheets was revealed from Raman spectra. Specifically, the increase of ordered phase in tested filaments, as a result of the drawing process was over 130%. The fiber post-drawn from a 100- $\mu\text{m}$  wide channel (PD-100) shows higher amount of  $\beta$ -sheet (and lower amount of the disordered phases) compared to fiber post-drawn from a 250  $\mu\text{m}$  wide channel (PD-250), which may be related to the smaller mean fiber diameter of that bundle, 2 versus 6.5  $\mu\text{m}$  for PD-100 and PD-250, respectively. This increase of  $\beta$ -sheet content in the drawn fibers results in a substantial increase of the mechanical properties of the

fibers. The PD-250 fibers have a strength of  $\sim 50$  MPa, which increases 4-fold to 210 MPa post drawing. The PD-100 fibers show a further strengthening to 614 MPa. PD-100 is reported to have a Young's modulus as high as 19 GPa, which exceeds those of natural spider dragline silk (11–17 GPa) and degummed cocoon silk (5 GPa). Thus, a remarkable drawing-induced strengthening and stiffening (surpassing natural silk properties) is possible as a consequence of conformational changes of silk ultrastructure and specifically of the increase of  $\beta$ -sheet structures, and the effects are more pronounced in the smaller fiber diameter.

In a two-step stretching setup, with a coagulation bath in which the fiber is pulled by a roller after its extrusion, followed by a water-immersion step driven by another roller, which is introduced to cause drawing on the spun fibers, the impact of roller speed in steps 1 and 2 was studied.<sup>219</sup> Using a parameter DR defined as the ratio between take-up speed and extrusion speed for each of the rollers, 1 or 2, this study demonstrates that conditions of high DR<sub>1</sub> with high DR<sub>2</sub> are untestable as fibers break before the end of processing. High DR<sub>1</sub> necessarily implies low contact time with the coagulation bath, while high DR<sub>2</sub> implies a greater degree of wet-stretching. Tensile tests show optima for fracture strength and extensibility, with maximum values of 360 MPa and 9%, at high DR<sub>2</sub>, but only when DR<sub>1</sub> is sufficiently high. Combinations of one high and one low DR parameter generally result in lower fracture strain, though higher DR<sub>2</sub> correlates to higher fracture strength and stiffness in general. Unsurprisingly, higher DR<sub>1</sub> correlates to smaller fiber diameters, though no clear trend is observed.

The same setup allows studying the effects of supercontraction on the spun silk fiber's mechanical properties.<sup>219</sup> Supercontraction describes a process observed in natural silk fibers in response to a polar solvent (e.g., water) which causes them to soften and reduce their length up to 60%<sup>213</sup> (see Figure 8D). This process reflects an ultrastructural transition in silk from an oriented glassy phase to a disoriented rubbery phase.<sup>213</sup> In effect, a supercontractable material differs from a contractable material by the existence of a “ground state” which erases loading history and allows the material to perform as if it were pristine when returned to the original length.<sup>219</sup> Examples in spider dragline silk show that when a fiber is supercontracted and then stretched back to its original length, the tensile properties remain almost unchanged, even though the two states differ in their ultrastructure (amount and distribution of  $\beta$ -sheet,  $\alpha$ -helix, and random coil conformations) significantly.<sup>213,220,221</sup>

Regenerated silk fibers also demonstrate this behavior, with sample length measurements showing that wet-stretched samples that are kept immersed in water for

24 h before drying, to allow their contraction, shrink by approximately 12% of their length immediately after stretching and immersion in water, or by a maximum of 24% after drying.<sup>219</sup> In fact, fibers loaded in tension and unloaded before failure, when reimmersed in water can reach full length recovery which due to the ground state recovery allows them, when they are tensile tested for the second time, to produce identical stress–strain curves as their first-time loading. Intermediate stress–strain profiles between those obtained from uncontracted and fully supercontracted samples could be achieved by controlling the degree of supercontraction.<sup>219</sup> The proposed deformation behavior of supercontracted samples includes (1) breaking of hydrogen bonds, (2) unfolding of secondary structures, and (3) nanocrystals and ordered regions surrounding them carrying the supplied load, in agreement to pure silk fracture behavior reported in Section 2.3.<sup>123,147,222</sup>

The ultrastructural changes during supercontraction in natural spider silk include a notable  $\beta$ -sheet content increase and random coil and  $\alpha$ -helix structures decrease, while their orientation remains almost unchanged.<sup>220</sup> The random coil and helix conformations are considered to extend and form thermodynamically favorable  $\beta$ -sheets upon supercontraction and subsequent stretching, and then spatially rearrange to form clusters of  $\beta$ -sheet crystals. AFM studies show  $\beta$ -sheet clustering which would lead to sub-optimal load-transfer throughout the fibers, explaining why properties do not change while crystal content increases.

### 3.3.2 | Effects of temperature and humidity

Another physical processing method to alter the ultrastructure of silk fibroin proteins, coined as temperature-controlled water vapor annealing (TCWVA),<sup>223</sup> includes heating silk fibers in presence of humidity. Higher annealing temperatures or times promote  $\beta$ -sheet crystallization so that the silk fiber's crystalline ( $\beta$ -sheet) versus amorphous ( $\alpha$ -helix, random coil) content can be tuned. Crystallinity can vary from 14% to 60% by varying the annealing temperature from 4 to 100°C.<sup>223</sup> Following the  $\beta$ -sheet content increase with increasing annealing time and temperature, the tensile modulus and strength also drastically increase from about 10 to over 70 MPa and from 2 to almost 8 MPa, respectively (minimum value for non-annealed sample and maximum value for the 95°C-annealed sample). The gradual increase in stiffness and strength, as well as  $\beta$ -sheet amount as a function of annealing temperature, demonstrates the phase transition between  $\alpha$ -helix and random coil to  $\beta$ -sheet (crystallization).

The same method in nacre-like graphene oxide (GO)-silk composites essentially utilizes the presence of GO nanoflakes as hydrophobic nucleation sites to promote the  $\beta$ -sheet crystallization of silk fibers.<sup>224</sup> In presence of GO, the effects of TCWVA on silk crystallization are higher than when no GO is present, demonstrating the catalytic activity of GO platelets. As a consequence of the higher  $\beta$ -sheet content, the annealed GO-silk nanocomposites also demonstrate significantly higher stiffness, strength and toughness compared to the pure SF control materials. A progressive increase with GO amount is seen for the Young's modulus, from 13 to 95 GPa, and the ultimate strength, which goes from 120 to 326 MPa—in both cases the highest value is at the highest GO concentration (53.7 vol% GO). As expected with the reduction of amorphous content, the elongation to break is decreased with increasing GO amount, from about 1.2% to about 0.5%.

### 3.3.3 | Amyloid composites

Using amyloid fibrils to mechanically reinforce alginate hydrogels was recently reported.<sup>225</sup> Genetically engineered *E. coli* was used to express CsgA-TFF2 curli fibers, which had a Young's modulus of  $1508 \pm 882$  MPa. The curli fibers were introduced into an alginate solution before crosslinking with calcium salt and then swelling in water. The alginate matrix alone has a Young's modulus of about 40 kPa. 10% of curly fibers result in a nearly triple Young's modulus, compared to the pure alginate hydrogel, while increasing curli fiber content up to 40% leads to a stiffness of about 160 kPa, or a 4-fold increase, over the alginate matrix. Furthermore, swelling ratio tests of the hydrogels showed that addition of amyloids does not interfere with water absorption or disrupt the crosslinking process of the hydrogel, making amyloids a successful reinforcing agent for alginate hydrogels.

An interesting use of amyloid fibers is their serving as a protein matrix binding inorganic nanoplatelets such as gold<sup>214</sup> (see Figure 8E) or graphene in nacre-like hierarchical nanocomposites.<sup>226,227</sup> Inspired by human bone being primarily composed of an organic matrix of strong hydroxyapatite (HA) crystals and tough collagen fibers, biomimetic, bone-like composites by replacing collagen with amyloid fibers were proposed.<sup>226</sup> Amyloids synthesized using  $\beta$ -lactoglobulin and lysozyme proteins, were solution-mixed with nanoplatelets of brushite or HA and converted into a film by vacuum filtering and air-drying. The incorporation of amyloid fibrils in the HA or brushite aqueous suspension stabilizes the solution, which otherwise would precipitate. Using either negatively charged  $\beta$ -lactoglobulin or positively charged lysozyme results in stable composites in suspension, which enabled the

fabrication of stable nanocomposite films with amyloid concentrations of 10–60 wt%. The films have a nacre-like hierarchical structure with layers of platelets separated by the organic amyloid filler. This structure resulted from the preferential lamellar stacking of inorganic platelets during the filtration process. The lamellar stacking was more uniform with brushite platelets due to their larger aspect ratios. Tensile testing of the nanocomposite films showed that increasing amyloid content results in decreasing void fraction and progressively increasing stiffness due to better adhesion between plates. Both density and Young's modulus peaked around 40 wt% amyloid content for both HA and brushite composites, at 1.16 g/cm<sup>3</sup> and 1.35 GPa for brushite-amyloid and 1.02 g/cm<sup>3</sup> and 0.8 GPa for HA-amyloid composites, respectively. In context, these bone-mimicking amyloid composites achieve the same stiffnesses at lower densities compared to artificial bone cements and overlap in properties with natural cancellous bone. For amyloid concentrations higher than 40 wt%, the elastic modulus drops, as expected by the rule of mixtures.

Replacing the mineral platelets with graphene sheets and using  $\beta$ -lactoglobulin fibers, at concentrations from 0.5 to 8 times the GO amount,<sup>227</sup> confirmed the same effects as when the amyloid fibers were introduced in HA and brushite.<sup>226</sup> Increasing amounts of amyloids improves the stability of the solution and prevents GO aggregation and subsequent precipitation. The lamellar microstructures comprise of stacked GO sheets separated by amyloid fibrils, similar to that seen in their previous amyloid-HA/brushite composites, and they were able to be formed up to composites with 1:5 (GO:amyloid) ratio. Tensile testing showed a maximum Young's modulus of 7.6 GPa for the 1:2 ratio composites, which dropped to 2.5 GPa for the 1:5 and 1:8 composites. Therefore, the tested higher amounts of amyloid fibers result in weaker lamellar structures. Finally, the plasticizing effects of water uptaken by the amyloid fibers were demonstrated through tests conducted at samples preconditioned at different relative humidity levels. A gradual increase in the strain to break with a simultaneous decrease of elastic modulus are presented in the tensile results, consistent with water plasticizing effects in the amorphous protein domains.

## 4 | UNTREATED BIOMATTER IN MATERIALS AND COMPOSITES

An emerging strategy in creating sustainable biocomposite materials consists in utilizing the whole microorganism (genetically engineered or not) as a material building block. Such hybrid bottom-up approaches create

hierarchical biocomposite materials effectively utilizing the natural molecular engineering provided from biosynthesis processes. This class of *Biomatter-based Materials* of a microorganism assembly serving as a heterogeneous biopolymer matrix. Using the whole microorganism allows for less harsh and environmentally friendlier processing methods, since no extraction or purification processes are required. As a result, no biomatter is wasted and in the literature-reported examples, there is minimal solvent waste.<sup>228–231</sup> In addition, microorganisms can be cultured in-situ, without requiring large or arable land usage, and allow the flexibility of tuning composition and microstructure on site.

### 4.1 | Plant-cell based materials

Combining entire cultured plant cells to make hybrid biological matrix materials was first demonstrated for tobacco plant cells.<sup>232,233</sup> The cells were solution-mixed with carbon nanotubes (CNTs) and cast into films. The resulting biocomposite films have a tensile modulus of about 91 MPa and a tensile strength of 3 MPa. It is important to note that the plant cells used in these studies are undifferentiated, un lignified and they are obtained from an in-vitro, fast-growing unicellular lab culture.

Follow-up work on the same type of plant cells<sup>230</sup> showed that by changing the processing method from casting and air drying to cold compression molding, bulk, three-dimensional biocomposites can be obtained that are able to self-bind without requiring the use of surfactants, adhesives or additive particles to assemble structures (see Figure 9A). These cultured, self-binding, biomatter-based composites reach a tensile modulus of 2.5 GPa and an ultimate strength of 21 MPa, at a density of about 1 g/cm<sup>3</sup>. Comparing the properties of this pure cell material with the films made of the same cells with a surfactant and CNTs,<sup>232,233</sup> we note a 27 times improvement in modulus and 7 times increase in strength, which arises from the ability to facilitate higher inter-cellular adhesion from the applied compaction process. The cultured tobacco cells, used in both cases, develop a thin primary cell wall composed of about 15 wt% cellulose fibrils, immersed in a heterogeneous matrix of hemicellulose, pectins, phenolics and proteins. When the cultured cells are compressed inside a permeable mold, at a rate that is determined from the cell dehydration rate, the water is progressively removed, and the cells get compacted. This compaction in presence of water activates a set of self-binding mechanisms. As the hydrated cells are compacted, polymer chain diffusion between the adjacent cell walls causes a fibrillar interlocking. As a result, the interpenetrating polymer nanofibrils of neighboring cell walls

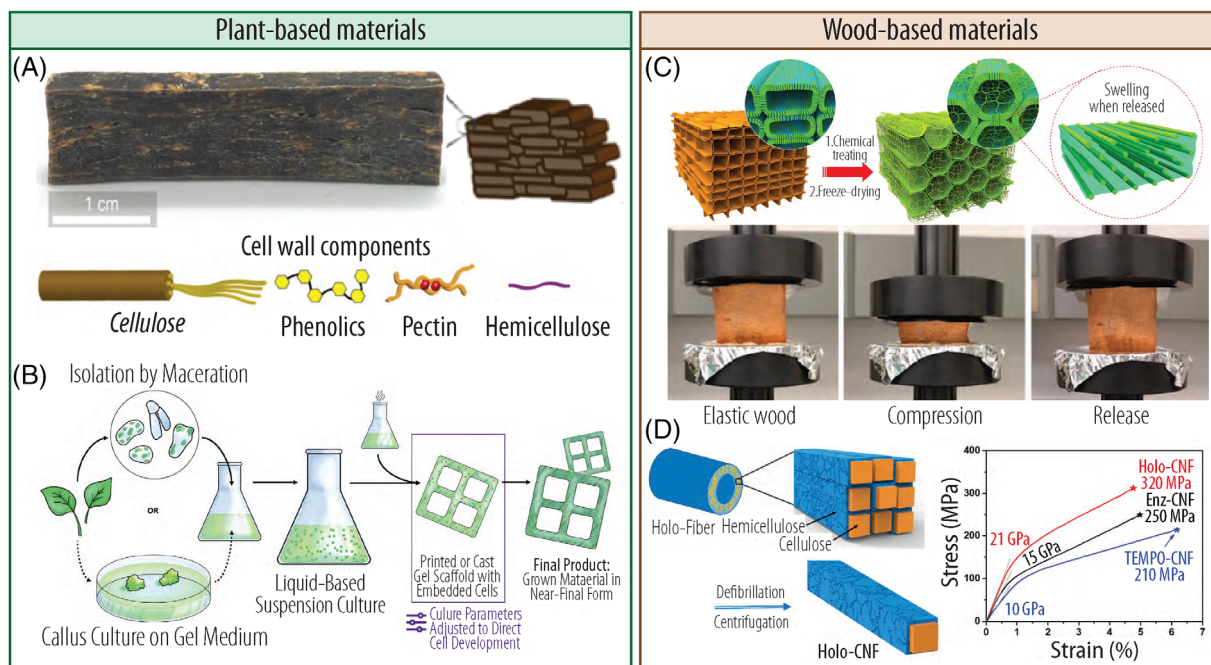


**FIGURE 9** Plant-cell and wood-based materials. (A) Plant cell-based beam produced by slow-pressing of tobacco cells. The native cell wall components enable the bonding and resulting appealing mechanical properties of the produced materials. Adapted from Reference 230. (B) Growing plant tissues into the target near-final form using 3D-printed solid culture medium containing *Zinnia elegans* cells. Reproduced from Reference 234 (CC BY). (C) Chemical treatment enabling the fabrication of elastic wood. Upon compression, the resulting wood cells do not rupture, but instead recover upon unloading. Adapted with permission from Reference 235 Copyright 2020 American Chemical Society. (D) Eco-friendly lignin extraction of wood fibers to produce holo-cellulose (containing cellulose and hemicellulose), to fabricate strong materials. Adapted from Reference 236.

interact with each other through hydrogen bonding and van der Waals bonding. These two mechanisms ultimately create a bulk, self-bonded heterogeneous polymer matrix. On the contrary, when the same cells are cast and air dried in absence of an external compaction force, they form weakly bonded, porous networks, with less cell contact area which is not able to activate those self-binding mechanisms seen upon application of a compression force. Even though the added CNTs facilitate binding in the thin films case, the obtained mechanical performance is inferior compared to the self-bonded materials. The pure plant cell biocomposites demonstrate a strategy to utilize in-situ, fast grown biomatter, that requires no chemical treatments, no extraction processes, and creates no waste (the entire grown biomatter is used) to produce bulk polymers with commodity plastic-like mechanical properties in terms of stiffness, strength and density.<sup>230</sup> The presence of other cell wall biopolymers (pectin, hemicellulose, phenolics, and proteins) leads to the lower strength and stiffness values compared to pure nanocellulose materials.

Another approach proposed by Beckwith et al.<sup>234</sup> consists in growing plant tissues directly into the target near-final form (see Figure 9B). Using 3D printing, *Zinnia*

*elegans* cells and their solid culture medium were extruded in a 3D-pattern and were able to maintain a cell viability over 70% after 10 days of incubation. After the printing process, the viable cells grow and multiply into clusters, filling the 3D-printed forms. The possibility or retaining cell differentiation enables also tissue-like formations, as demonstrated in that work. One advantage of this technique is the possibility to tune the culture parameters to improve the target properties. Natalio<sup>237</sup> showcased a plant cell culture technique that permits adjusting the ultimate material properties by assimilating functional additives straight from the culture medium. For example, the synthesized cellulose fibers from cultured ovules could acquire properties like fluorescence and magnetism depending on the functional molecule used.

## 4.2 | Wood-based materials

Wood derivatives are also commonly used to fabricate sustainable alternatives to petroleum-derived materials. As described in Section 3.1, cellulose extracted from wood can be shaped or blended into functional materials.

Alternatively, milder extraction approaches have been recently suggested allowing the preservation of the structure and some of the native constituents of wood feedstocks, for example, hemicelluloses or lignin.

A first approach is to preserve the native cellular structure of wood and apply treatments to induce additional functions. Chen et al.<sup>235</sup> fabricated an “elastic” wood by partially removing lignin and hemicellulose from natural wood (see Figure 9C). Upon mechanical loading and unloading, this material recovers its original shape (height loss close to 0% after uni-axial loading). In another study, by Li et al.,<sup>238</sup> the authors fabricate a cellular cellulose material by completely delignifying native wood while preserving only a small proportion of hemicellulose (~3%). The resulting light-weight material, coined *nanowood*, has extremely low thermal conductivity, 0.03 W/mK in the transverse direction (even rivaling the low thermal conductivity of styrofoam). On the other hand, high-density woods were produced by first partially removing lignin and hemicellulose, and subsequently hot-pressing to obtain densified woods showing strength values as high as 587 MPa.<sup>239</sup> The optical properties of woods can also be enhanced to modify color and enable photonic applications as suggested in a study by Xia et al.<sup>240</sup> The authors describe a process to remove the chromophore groups of lignin, responsible for wood's brown color. The decolored wood contains 80% of its original lignin content, thereby preserving its strength and water-repellent properties. Recent reviews will provide further information about modified woods.<sup>241,242</sup>

Another approach to leverage the good properties of wood consists in casting or pressing modified wood powders into functional shapes. For example, Yang et al.<sup>236</sup> made use of delignified wood fibers in which the native hemicellulose is conserved (see Figure 9D). After mechanical defibrillation, the resulting holocellulose nanofibers are cast into films, which show appealing transparent properties, and relevant mechanical properties (Young's Modulus of 21 GPa and tensile strength of 320 MPa with an elongation to break around 4.5%). The authors argue that the natural hemicellulose coating the CNFs enables for more stable aqueous suspensions. Another article further showed the value of maintaining native wood constituents in hot-pressed cellulosic films.<sup>243</sup> In this study, the authors intentionally preserved a controlled fraction of the lignin present in wood feedstocks by adapting the Kraft pulping and bleaching stages. Despite the presence of lignin, they reported good mechanical properties of hot-pressed films of microfibrillated lignocellulose. The best performance was obtained for the composition with 5.1 wt% lignin; the film had a Young's Modulus of  $18.9 \pm 0.8$  GPa and tensile strength of  $263 \pm 17$  MPa with an elongation to break

$3.9 \pm 0.1\%$ . More importantly, the authors showed that the presence of lignin conferred water resistant properties to the natural composites, as exemplified by the 83 MPa strength after 8-day immersion in water of a film containing 16.9 wt% lignin (in contrast to the ~30 MPa strength of an immersed film containing only 1.8 wt% of lignin). A recent review on pressed wood materials with all-natural compositions will provide the interested reader with extensive information.<sup>244</sup> In a recent study, Pascoli et al.<sup>245</sup> turned to wheat straw as lignocellulosic feedstock. To partially remove lignin and hemicellulose, the authors made use of an alkaline peroxide treatment combined with a mild peracetic acid (PAA) pretreatment, thereby producing lignocellulosic fibrous nanomaterials. They showed that the resulting nano and microfibrils can have different amounts of residual lignin and hemicellulose which could be controlled by the processing. Additionally, the resulting heterogeneous lignocellulosic fibrils were demonstrated as a reinforcing filler in a biodegradable hydrophilic polymer matrix such as poly(vinyl alcohol) (PVA). Specifically, the authors produced PVA-lignocellulose nanocomposites with specific elastic modulus and specific strength of 2.6 GPa/(g cm<sup>-3</sup>) and 59.5 MPa/(g cm<sup>-3</sup>), respectively, and an elongation to break of 138%, which respectively marked 34%, 61%, and 91% improvements in modulus, strength and elongation to break over pure PVA.

### 4.3 | Bacteria cell-based materials

Bacterial cellulose (BC) composites in which the cultured bacteria are maintained in the produced cellulose network have recently been reported by Wan et al.<sup>246</sup> (see Figure 10A). This bacteria/BC (BA/BC) biomatter-based composite material was characterized after freeze-drying to create an aerogel. The reported mechanical properties include a tensile strength of 550 kPa, compared to 440 kPa for the pure BC aerogel, and a compressive strength (to 60% deformation, not to break) of 31.5 versus 17.8 MPa for the BA/BC and BC, respectively. Both tension and compression tests show that the BA/BC is still able to experience very large strains before failure, for tensile tests—about 35% (vs. about 43% for pure BC). A mechanism in which the cellulose nanofibrils use the bacteria cells as reinforcing particles/junctions, a result that overcomes the reduced crystallinity of the composite with respect to the BC (85% and 91%, respectively) to yield stronger and stiffer composites is proposed to govern the performance of BA/BC composites.<sup>246</sup>

Research on engineered living materials (ELMs) continues to grow beyond the soft material nature of living cells, particularly through the use of bacteria-based

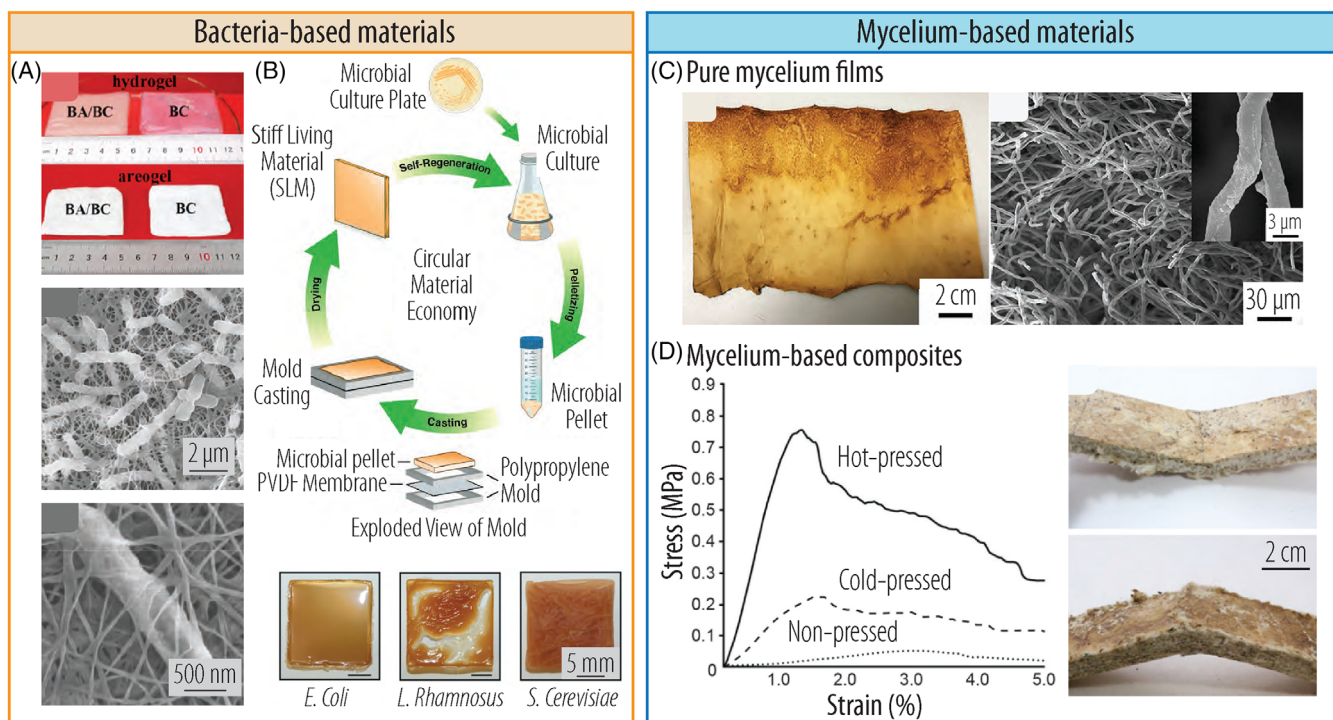


**FIGURE 10** Bacteria and mycelium-based materials. (A) Bacteria/bacterial cellulose (BA/BC) composites. The bacteria (*K. xylinus* X-2) remain in the fibrous matrix and provide reinforcement by serving as a junction, thus interlocking the BC nanofibers. Reprinted from Reference 246 Copyright 2019, with permission from Elsevier. (B) Fabrication of stiff living materials (SLMs) using different strains of bacteria following a circular material economy. Reproduced from Reference 228. (C) Vegan mushroom-based leather using the fruiting body of *P. ellipsoideus*. Adapted with permission from Reference 247 Copyright 2020 American Chemical Society. (D) Three-point bending stress-strain curves for *P. ostreatus* mycelium grown on rapeseed straw without pressing (dotted line), and cold (striped line) or hot (solid line) pressing. The photographs correspond to *P. ostreatus* grown on cotton and hot-pressed. Reprinted from Reference 248 Copyright 2019, with permission from Elsevier.

composites. A new category of ELMs, stiff living materials (SLM), was recently coined to include biocomposites created by drying out the cultured bacteria and their produced biofilms. In the first demonstration of the SLM class, *E. coli* (EC), *Lactobacillus rhamnosus* (LR) or *S. cerevisiae* (SC) suspensions were used by Manjula-Basavanna et al.<sup>228</sup> (see Figure 10B). These bacteria cell-based materials are the stiffest presented ELMs, and maintain the ability of self-regeneration, as a population of living cells remains embedded in the matrix for more than 1 month after their fabrication. Nanoindentation-extracted Young's modulus values range for EC-SLM between 5 and 42 GPa, for LR-SLM between 5 and 30 GPa and for SC-SLM between 1 and 30 GPa. The wide variation in modulus highlights the heterogeneity of the materials when tested locally. The ability to regenerate these materials upon immersion in growth media is demonstrated for the EC-SLM samples, and the authors note that the material disperses in the media and creates a new turbid culture, therefore loses its structural integrity and dissociates back to individual cells, which can then be re-assembled for a subsequent generation of

SLMs. The mechanical properties of the second and third generations of EC-SLMs were identical to the first generation (with the same large variation 5–41 GPa), demonstrating the robustness of these cell-based materials.

In a similar approach by Duraj-Thatte et al.<sup>229</sup> biofilms created from genetically engineered EC, coined *aquaplastics* as they are water-processable and able to be shaped through molding in presence of water, were reported. The engineered EC synthesize CsgA-based curli fibers in a hydrogel mesh, which is harvested, mixed with sodium dodecyl sulfate (SDS) to induce gelation, cast in a mold and dried in ambient conditions, finally resulting in aquaplastics with the shape of the selected mold. The authors compare the properties of the native biofilms, in which the microbial cells (some of which are still viable) remain embedded in an extracellular curli matrix, with pure curli biofilms, which are the remaining gels after the cells have been removed from the matrix. As expected, when the cells remain embedded in the matrix, the “native” biofilm is weaker than the pure curli fiber control. Through nanoindentation, the authors find a 2.2 GPa elastic modulus for the native biofilm versus

4.3 GPa for the pure protein film. Tensile testing shows the native film having a modulus of 1 GPa and ultimate strength of 18 MPa, thus classifying these cell-based bacterial composites in the SLM category. The pure curli films have a modulus of 1.2 GPa and strength 29 MPa in tension, higher than the native film, as expected. A critical advantage of these cell-based materials is their self-healing ability, demonstrated in this work upon rehydration of the damaged region. Scratches and full thickness cuts made on the native biofilm are completely repaired by spraying water onto the damaged region and followed by ambient drying. Curli biofilm controls also have water-healing abilities but the resulting films are slightly less smooth, with some “marks” of the scar remaining on the film. Tensile tests on damaged and water-healed native films show a 40% reduced modulus (605 MPa) and a 33% reduced strength (12 MPa) indicating that the native films post-healing lose some of their strength and stiffness but still are able to have a performance comparable to commodity synthetic plastics.

Bacteria-driven biomineralization is another fast-growing field of research for biomatter-based materials and composites. For example,  $\text{CaCO}_3$  precipitation of certain bacterial strains when grown in favorable conditions, is an emerging research field with applications in self-healing materials, such as bioconcrete, other structural applications, as well as heavy metal removal.<sup>249</sup> We refer the reader to recent reviews on this topic<sup>250–252</sup> as these works focus on utilizing the inorganic product catalyzed by the bacterial activity rather than the actual microorganism as a building block by itself, which is the thesis of our review. In the same trajectory, the emerging class of living building materials (LBMs), which combine photosynthetic cyanobacteria that precipitate  $\text{CaCO}_3$  in the presence of structural scaffolds, paves the way towards integrating living microorganisms in the built environment.<sup>253</sup> Again, this goes beyond the scope of our review and the reader is referred to other reports on this topic.<sup>254,255</sup>

## 4.4 | Fungal materials

Mycelium-based materials can be tuned over a wide range of mechanical properties and density, which, combined with fast (compared to other microorganisms) growth times and low cost fabrication, makes this particular class of biomatter-based materials highly attractive to a plethora of commercial applications. The remarkable range of mechanical properties offered by mycelium-based materials is summarized graphically in the diagrams of Figure 11. For densities ranging between 0.06 and 2  $\text{g/cm}^3$ , literature reports elastic moduli in the range 0.02–3000 MPa and strengths in the range 0.05–40 MPa.

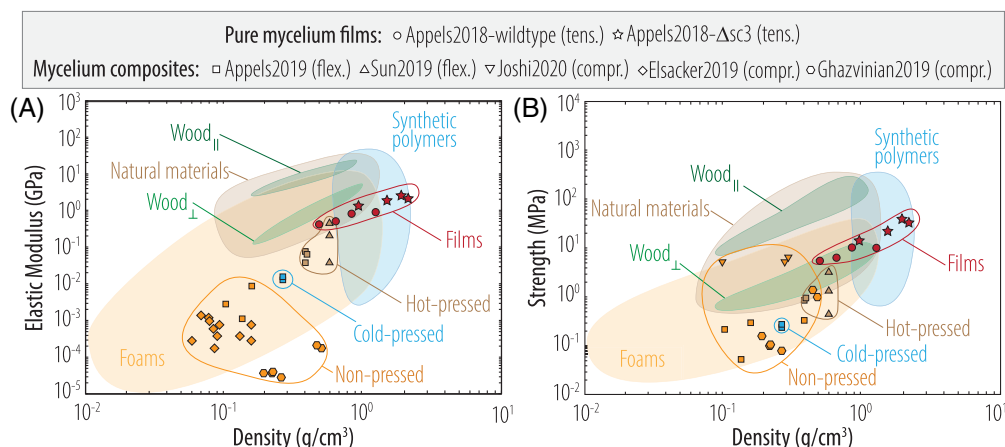
Fungi are attractive as a biobased material platform not only because of their fast growth, but also for their ability to grow by degrading lignocellulosic waste such as sawdust and straw (among other materials)—all considered agricultural waste or biomatter-processing waste.<sup>248</sup> Mushroom fungi are known to colonize their substrate by growing filamentous cells, called hyphae, which typically measure about 2–10  $\mu\text{m}$  in width. Hyphal cells grow by consuming lignocellulosic feedstock material, resulting in a three-dimensional fibrous network comprised of cells branched with their feedstock material essentially “molded” into the shape of feedstock material. As mentioned in Section 2.2, the main cell wall components of hypha cells are chitin,  $\beta$ -glucans and proteins, with  $\beta$ -glucans serving as mucilage in the outer part of the cell walls and the chitin fibrils covalently cross-linked or hydrogen-bonded with other biopolymer matrix components in the inner part of the wall.<sup>106,261</sup> Mycelium-based materials have properties that are defined by the individual cell-based filaments as well as their network-based organization, connectivity (interactions between filaments) and, in case of composites in which the feedstock material remains in the product, the type and amount of feedstock. Independently of whether the feedstock is maintained in the final product, mycelium-based materials, after their growth or culture phase, are subjected to a final heating step to cease growth. That step results either in preserving the fungus in a “hibernated” state, which allows for the possibility of a subsequent regrowing cycle when survival moisture conditions are met, or in permanent ceasing of the fungus, depending on the temperature and heating duration.<sup>248</sup> In this section, we present examples in which the growth substrate and processing method allow for a modulation of the microstructure and mechanical properties of mycelium-based materials and composites. We first focus on pure mycelium films before discussing mycelium-based composites. For comprehensive reviews focusing on mycelium-based materials, we direct the reader to References 262–264.

### 4.4.1 | Pure mycelium films: Effects of culture conditions

The growth media and environmental conditions have an important effect on the resulting mycelium-based materials films. For example, culturing *Ganoderma lucidum* (*G. lucidum*) and *Pleurotus ostreatus* (*P. ostreatus*) in either pure cellulose or cellulose-potato dextrose broth (PDB) substrates shows that both types of fungi contain higher chitin content and lower amount of lipids when grown in pure cellulose substrates.<sup>265</sup> In accordance to these differences, since chitin is the main structural



**FIGURE 11** Mycelium-based materials in the context of commercial low density materials. (A) Elastic modulus and (B) strength. The type of mechanical test is described in the legend (tens. for tensile, flex. for flexural, and compr. for compressive test). Data extracted from References 248,256–260.



biopolymer on the fungal cell wall while amorphous lipids provide extensibility via plasticizing the walls, the mycelia films grown in pure cellulose media are consistently stiffer, stronger and less ductile compared to those grown in cellulose/PDB. Specifically for *G. lucidum*, the cellulose-grown films show a 200% increase in elastic modulus (from 4 to 12 MPa), 38% higher tensile strength (0.8–1.1 MPa) and 58% lower elongation to break compared to cellulose-PDB-grown films (from 33% to 14%), while for *P. ostreatus* the elastic modulus is increased by 65% (17–28 MPa), the strength is reduced by 36% (1.1–0.7 MPa), and elongation to break is reduced by 55% (9%–4%). In another study from the same group, Antinori et al.<sup>266</sup> reported the effect of adding either glucose or lignin to the PDB on the growth and morphology of *G. lucidum*. They showed that the D-glucose-enriched medium (44.4 wt% PDB and 55.6 wt% D-glucose) accelerated the mycelium growth by a factor 2.5 in mass compared to pure PDB. On the other hand, the study shows that the lignin-enriched medium (92.3 wt% PDB with 7.7 wt% alkali lignin) favors a concentric growth of a dense mycelium film, in contrast to the growth of sparse colonies in the two other cases.

The effects of light and CO<sub>2</sub> levels in mycelium culturing were studied for *Schizophyllum commune* (*S. commune*)<sup>256</sup> in wild type and upon deletion of the hydrophobin gene (*sc3*), which is known to impact the amount of cell wall glucans. When either the wild type or mutant mycelia are cultured in dark, those with low supplies of CO<sub>2</sub> produce films of higher density and better mechanical properties. When grown under light, high CO<sub>2</sub> results in higher density and mechanical properties for both strains tested. The highest difference for the mutant is noted when it is cultured in dark in high versus low CO<sub>2</sub> flows, with resulting films showing a modulus of 1.2 versus 2.5 GPa and strength 15.6 versus 33.9 MPa for high and low flows, respectively. For the wild type, the differences are smaller but still the CO<sub>2</sub> flows cause

the biggest impact, with films cultured in light having a modulus of 438 versus 913 MPa and strength 5.1 versus 9.5 MPa for low and high flows, respectively. Thus, the different light conditions and CO<sub>2</sub> supplies allow a large variation of mycelium film density and mechanical properties in *S. commune* wild type and the tested mutant. The *sc3* gene deletion in *S. commune* results in the highest reported density and mechanical properties among all pure mycelium films.

In a study by Bustillos et al.,<sup>247</sup> the fabrication method of a vegan leather is proposed, containing only *Phellinus ellipsoideus* (see Figure 10C). This material combines thermal stability up to 250°C, mechanical robustness (elastic modulus of 1.2 MPa, ultimate tensile strength of 572.5 kPa and strain to failure of 101%) and scratch resistance. Interestingly, the high strain to failure is attributed to the natural balance between (hard) chitin and the (soft) protein content in the mycelium. The authors also report enhanced damping capabilities in the frequency range 5–20 Hz, which they attribute to the alignment of mycelium fibers under loading.

#### 4.4.2 | Mycelium-based composites: Effects of feedstock substrates, additives and processing methods

We now highlight selected results that help establish a fundamental understanding of the impact of processing method and substrate on the mechanical properties of mycelium-based composite materials.

Appels et al.<sup>248</sup> compared the compression method in mycelium-based composite foams on *P. ostreatus* and *Trametes multicolor* (*T. multicolor*) grown in straw, sawdust or cotton substrates and formed using no pressure versus cold or hot pressing. Their results clearly show that hot pressing results in more homogeneous composites with higher density and mechanical properties at all

tested conditions—both in tension and bending (see examples in Figure 10D). Specifically, the elastic modulus and flexural strength for the hot pressed composites are 5–35 and 3–8 times higher than unpressed or cold-pressed foams in all tested conditions. Between *P. ostreatus* and *T. multicolor*, in non-pressed as well as in hot-pressed samples, *T. multicolor* composites have higher mechanical properties compared to the *P. ostreatus* ones even at similar densities (within maximum  $\pm 0.03 \text{ g/cm}^3$  uncertainty).<sup>248</sup> The range of densities in that study was 0.1–0.39  $\text{g/cm}^3$ , resulting in Young's modulus 2–100 MPa, tensile strength 10–240 kPa, at elongations 0.5%–4.7%, flexural modulus 1–80 MPa and flexural strength 50–870 kPa. These results confirm that fungal materials are more resistant to bending compared to tension, which is seen also in plant cell biocomposites.<sup>230</sup> Comparative tests on foams from *Coriulus versicolor* (*C. versicolor*) and *P. ostreatus* with wood chips, hemp hurd, loose hemp fiber and non-woven mats of hemp fiber substrates,<sup>267</sup> show that on the same substrate, *C. versicolor* gives stronger and stiffer composites compared to *P. ostreatus*.

Comparing the effects of cotton versus straw as the substrate material in *P. ostreatus* hot pressed foams,<sup>248</sup> shows that cotton results in foams with lowest Young's modulus (34 vs. 97 MPa), strength (130 vs. 240 kPa), flexural modulus (34 vs. 72 MPa) and flexural strength (620 vs. 870 kPa), at similar densities of 0.35 versus 0.39  $\text{g/cm}^3$ , compared to same species grown in straw. This difference is consistent with the composition of the natural fibers, with straw having higher lignin and similar cellulose content compared to cotton.<sup>268–270</sup> For the same species and growth conditions, cold pressing practically eliminates any difference between the cotton versus straw substrate in terms of composite performance. This can be related to the lower density (0.24  $\text{g/cm}^3$  for cold-pressed samples grown in either substrate, versus 0.35 and 0.39  $\text{g/cm}^3$  for hot-pressed samples grown in cotton and straw, respectively) and thus lower cohesion of the cold pressed versus hot pressed samples. Non-pressed films of *T. multicolor* grown on sawdust have higher properties than those grown on straw,<sup>248</sup> which can be related to the beech sawdust's higher lignin content compared to rapeseed straw.<sup>271,272</sup>

Another important factor in mycelium-based composites is how the non-mycelium materials are incorporated in the composite. In composites of basidiomycete mycelium with wood particles (mixture of spruce, pine, and fir [SPF] particleboard particles),<sup>257</sup> it has been shown that when the mycelium first is grown on culture media and is then subsequently mixed with wood particles (“passive” mixing), the produced composite is weaker and softer compared to the same species grown directly on the wood particles. Specifically, the wood particle-grown

mycelium is 6.2 stiffer (from 36 to 223 MPa in flexural modulus) and 2.66 times stronger (from 0.45 to 1.2 MPa in flexural strength) compared to passively mixed mycelium with wood particles, at the same composite density (0.6  $\text{g/cm}^3$ ). The same work shows that the incorporation of just 2.5 wt% CNFs induces a significant enhancement of mechanical performance (modulus increase from 223 to 514 MPa and strength increase from 1.2 to 3.5 MPa for the wood particle-grown mycelium), still at a sample density of 0.6  $\text{g/cm}^3$ . Further increase in CNF content only slightly improves the modulus of rupture of the composites and the rest of the composites maintain the same properties. These unaltered properties demonstrates that the optimum level of CNF to promote better interfacial bonding is no more than 2.5 wt% for these systems.

Similarly, the effects of another organic additive, carbohydrate fillers (proprietary composition) when incorporated at different stages of the composite processing cycle are also able to drive significant changes in the mechanical properties of the composite foams.<sup>273</sup> The comparison of samples in which varying amounts of carbohydrate fillers are introduced in corn stover substrates either during the initial inoculation or after a homogenization step that happens at the middle of the growth cycle, shows that when the nutrition change happens during homogenization step, it notably enhances the mechanical properties of the composites regardless of the size of the stover particles. Increasing amounts of carbohydrates ensuring the homogenization step from 0 to 35 wt% leads to a significant increase in specific flexural modulus (from 14 to 22  $\text{kPa}/(\text{g cm}^{-3})$ ) and strength (from 2 to 4.5  $\text{kPa}/(\text{g cm}^{-3})$ ). On the other hand, a similar carbohydrate addition during the inoculation step does not drive a similar correlation. A positive correlation between the filament branch density and the mechanical properties of the composites is only possible when nutrients are added in the homogenization step. Indeed, when carbohydrates are added at the homogenization stage a denser hyphal branching is observed, which supports the improved mechanical properties. When the same fillers are added in the inoculation but subjected to homogenization at the middle of the growth cycle, the networks they have formed break up, resulting in inferior mechanical properties. Furthermore, we propose that the effects of the carbohydrates as “intact fillers” ought to be considered for this particular case. Introducing carbohydrates in the homogenization step leaves less time for the mycelium to digest them, so they serve primarily as fillers and improve the mechanical properties of the composite, whereas when they are introduced during inoculation a higher amount of them can be digested.

Another study on the effects of carbohydrate-rich additives when introduced at the beginning of the growth

cycle in *P. ostreatus* composite foams<sup>260</sup> shows that there are additives able to drive changes in mechanical properties even when added during inoculation. In that case study, sawdust, straw and 1:1 sawdust:straw mixture substrates were supplemented with 10 wt% wheat bran. The saw dust composites, with and without the supplement, result in the denser foams (density about 0.5 g/cm<sup>3</sup>), while the straw composites result in the lowest density (about 0.2 g/cm<sup>3</sup>), and their mixtures lie in between. The supplement causes a 10% and 30% reduction in the density of the saw dust and straw foams, respectively. When introduced in the composite substrate, the supplement leads to a 7% reduction in density. Remarkably, the compressive strength follows the opposite trend as density. When the supplement is added, the compressive strength of the sawdust composites is increased by almost 35% (from 1018.4 to 1380.6 kPa), that of the straw composites by 130% (from 72.7 to 169.2 kPa). Interestingly, the mixed composite has almost no change in density and only a 9.5% improved compressive strength (from 105.9 to 116.1 MPa) with the addition of the supplement. Moreover, the authors highlight that the supplement improves the foam homogeneity within the saw dust samples. Indeed, without the supplement, samples were disintegrated upon compression, indicating inhomogeneous cultivation, while samples with the supplement deformed but did not disintegrate.

Composites of *P. ostreatus* grown on sawdust, sugarcane and mixture of these substrates<sup>258</sup> show that the sawdust and the mixed substrates result in foams with the highest density and strength, 0.29–0.33 g/cm<sup>3</sup> and 6.7–7.5 MPa, respectively. The sugarcane-grown foams had the lowest density and strength, 0.11 g/cm<sup>3</sup> and 6.0 MPa, among the studied composites. The results confirm the ability of sawdust to promote denser and stronger *P. ostreatus* foam formation, as found also by the previously mentioned reports.<sup>248,260</sup>

The fibrous substrate physical form is another important consideration in mycelium composite foams. It has been shown that when hemp, flax and flax waste fibers are used in loose, chopped, dust, pre-compressed or tow forms, in *T. versicolor*-based composites, the obtained mechanical properties vary significantly.<sup>259</sup> Pre-compressed substrates result in significantly higher compressive modulus values for all types of substrates, while loose natural fibers consistently give the weakest foams. When the elastic modulus of loose fiber composites is compared to the rest, a 4.7 times increase is achieved by pre-compressing the flax substrate, a 3.7 times increase in flax waste and 2.3 times increase in hemp, at the same densities. Interestingly, introducing chopped fibers seems to also improve the performance of the foams compared to loose fibers, but does not exceed that of pre-

compressed fibers. Specifically, chopped flax substrates give 4.2 times stiffer composites compared to loose flax, and chopped hemp 1.5 times stiffer composites than loose flax. When comparing the loose fiber composites from hemp, flax and pine wood, we observe a consistently higher performance of flax and hemp which can be related to the notably higher cellulose content on these two fibers (in their initial form) compared to softwood, as discussed in Reference 265. The size of feedstock particles on the other hand, is not able to influence the composites' performance by itself. A study on a proprietary fungal/agro-waste particle system, scanning the effects of varying the size of agro-waste particles between 0.4 and 6.7 mm,<sup>261</sup> shows that all foams, regardless of the substrate particle size, when prepared with the same method, have approximately the same density and their compressive stress–strain curves are almost coinciding. Therefore, the density as well as the calculated compressive modulus appears to be insensitive to the feedstock particle size for this particular system.

Yeast cells have also been shown to be an alternative biomatter matrix material of the fungal kingdom, with *S. cerevisiae* being the only type of yeast reported for such biocomposites so far.<sup>274</sup> The limited literature focuses on *S. cerevisiae*-based hierarchical composites created through yeast fermentation in presence of silk fibers, CNTs, graphene nanoplatelets (GNPs) or synthetic polymers highlights the potential of this material class.<sup>274–277</sup> Porous structures obtained from CO<sub>2</sub> production during yeast fermentation have also been utilized, alone or in conjunction with introducing synthetic nanoparticles, to alter the density and mechanical properties of such composites.<sup>274</sup>

## 4.5 | Algae-based bioplastics

The rapid growth of algae compared to land plants combined with high yields, the absence of competition with agricultural land, the possibility to cultivate without intensive agricultural requirements such as fertilizers and irrigation, and the extensive environmental tolerance of algal species,<sup>278,279</sup> make algae a promising candidate for natural biomatter feedstocks. Even though the potential of algae as a source to extract a variety of individual compounds (polysaccharides, fatty acids, lipids, pigments, and proteins) is significant, the intensive pre-treatments which include lengthy wet processing in harsh chemicals and often high temperatures, mark the need for new processing methods, for this biomatter source to reach its full potential.<sup>35</sup> For literature on biocomposites with cellulose fibers extracted from algae biomatter and subsequently used as a filler in other polymer matrices, we direct the reader to References 278–280.

In this section, we first detail the biopolymers present in algal cell walls before reviewing applications where algae biomatter is used with little or no pre-processing to fabricate functional materials such as plastics alternatives using different methods. Note that, according to the International Union of Pure and Applied Chemistry (IUPAC),<sup>281</sup> “bioplastic” is a plastic that is “derived from the biomatter or issued from monomers derived from the biomatter and which, at some stage in its processing into finished products, can be shaped by flow.” Although the IUPAC discourages the use of the term bioplastic and proposes “biobased polymer” instead, which is defined as “composed or derived in whole or in part of biological products issued from the biomatter (including plant, animal, and marine or forestry materials),” in the following we will be using the term bioplastic as mentioned originally in the featured papers, and in all these cases, the term refers to algae-comprised biomatter that at one stage of its processing life can be shaped by flow.

#### 4.5.1 | Algal cell wall biopolymers

As mentioned in Section 2.1, algae species with organic cell walls have structural polysaccharides such as cellulose, alginate, agar and carrageenan.<sup>279,287</sup> There is a general classification of algal species based on their color and sizes, resulting in green algae (Chlorophyta), brown algae (Phaeophyta), and red algae (Rhodophyta) when color-classified. Size classification of algal species divides them to macroalgae (seaweed), which are multicellular, above micron sized organisms, and microalgae which are microscopic single-celled organisms, which may be prokaryotic, similar to cyanobacteria, or eukaryotic, similar to green algae (Chlorophyta).<sup>288</sup> In green macroalgal species (size ranges from microscopic up to tens of meters<sup>278</sup>), the cell wall consists of mainly sulphated polysaccharides such as ulvans and sulphated galactans, xylans, and mannans immersed in a primarily starch-based matrix.<sup>289</sup> The cellulose content in some filamentous green algae can be as high as 20–45 wt%.<sup>279</sup> In brown algae, cellulose microfibrils are immersed in an alginate and fucose-containing sulfated polysaccharide matrix.<sup>290</sup> In species such as *Macrocystis pyrifera*, *Laminaria hyperborean* and *Phaeophyta* sp., alginate is produced in amounts as high as 22%–44% of the dry cells weight.<sup>278</sup> In red algae, a sulphated galactan polymer matrix, of agar, funoran, furcellaran or porphyran hosts the cellulose, mannan or xylan microfibrils.<sup>34</sup> In red algae species such as *Chondrus crispus* and *Mastocarpus stellate* carrageenans are produced in amounts ranging between 30% and 50%.<sup>278</sup> The wide range of biopolymers produced in macroalgae, and in particular alginates, carrageenans,

fucoidans, ulvans and laminarins have long been utilized in the food, pharmaceutical, and cosmetics industries, after extraction and purification.<sup>291,292</sup> In addition, as will be discussed in this section, macroalgae has been used as a filler material upon drying and grinding. On the other hand, microalgae are used as a source of cytoplasmic proteins, lipids, pigments and cell wall polysaccharides.<sup>293–295</sup> In addition, as described in Section 3.1.4, microalgal species have been introduced in symbiotic cultures with bacteria to create hybrid and living composites, which opens up possibilities for the integration of microalgae in ELMs.<sup>177,296,297</sup>

#### 4.5.2 | Algal biomatter-based materials and composites

Devadas et al.<sup>298</sup> and Onen Cinar et al.<sup>299</sup> recently reviewed literature on algae-based biomatter materials, highlighting that in the majority of cases harvested algae is dried, pulverized and used either as a powder filler material in synthetic polymer matrices, or are further treated to remove proteins, lipids and other components and retrieve the main carbohydrates, or mixed with plasticizers/additives to create bioplastics. Below, we feature cases in which algae biomatter has not been disintegrated so that the cell structure is present in the final products and composites, as well as examples of pulverized biomatter where algal cell structure is no longer present in the final material.

*Chlorella* biocomposites with polyethylene (PE) were the first algae bioplastics reported in literature by Otsuki et al.<sup>284</sup> (see Figure 12D). Processed through melt mixing powdered algae with PE, these bioplastics pave the way towards biomatter-commodity plastic composites processable with industrially available methods. In this study, the matrix was modified using a compatibilizing agent to produce maleic anhydride grafted PE (MA-g-PE), to improve the filler-matrix adhesion.<sup>284</sup> Comparing biocomposites with and without compatibilizer, the tensile strength and modulus in all cases is notably higher when MA-g-PE is present. A monotonic decrease in strength, modulus and elongation to break with increasing microalgae amount is seen when no MA-g-PE is introduced, with both modulus and strength seeing more than a 50% reduction at the maximum attempted algae content (40%). However, when MA-g-PE is employed, the composites have a constant tensile strength of about 20 MPa which is about 5 MPa lower than pure PE, and the elongation to break, though incomparably lower to pure PE, is almost 10% higher for the same *Chlorella* amount without MA-g-PE. On the other hand, the elastic modulus sees a progressive increase with increasing algae amount

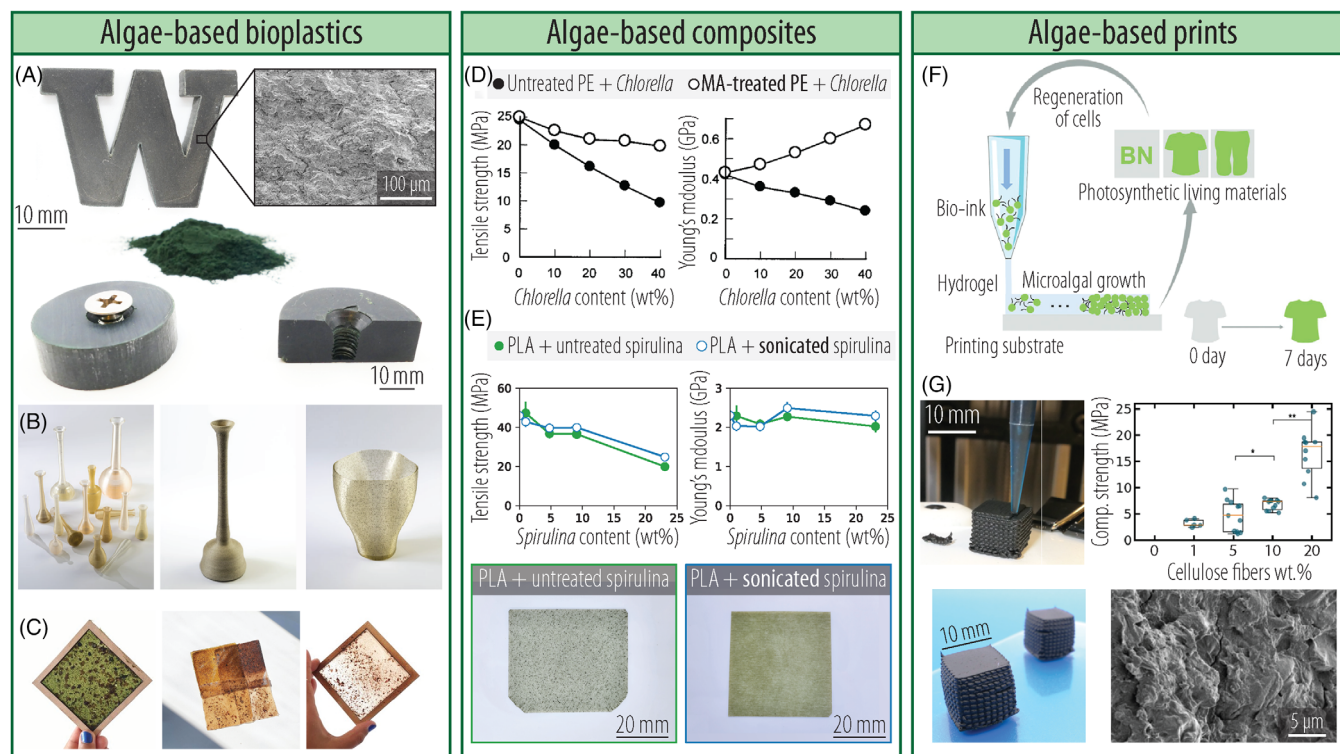


**FIGURE 12** Algae-based materials. (A) Bioplastics from hot-pressed algae (ongoing research from the authors). (B) 3D-printed biopolymer plastics from the Algae Lab (By Erik Klarenbeek And Maartje Dros).<sup>282</sup> (C) Bioplastics made from algae by Kathryn Larsen.<sup>283</sup> (Creative Commons CC BY). (D) Mechanical properties of polyethylene-chlorella biocomposites with and without maleic anhydride treatment. Reproduced from Reference 284. (E) Mechanical properties of PLA-spirulina biocomposites with and without sonication pretreatment to the spirulina filler.<sup>285</sup> (F) Printing photosynthetic living materials using bio-ink containing microalgae encapsulated within an alginate hydrogel matrix. Reproduced from Reference 286 (Creative Commons CC BY). (G) 3D-printing of spirulina-based slurries. The introduction of cellulose fibers drastically enhances the compressive strength of the 3D-printed cube. Reproduced from Reference 231.

in presence of MA-g-PE, exceeding the value for pristine PE. The maximum enhancement of about 75% is achieved in the 40% *Chlorella* composite. The paper documents the ester bond formation between the MA-g-PE and *Chlorella*, in agreement with the improved compounding of the composite and the significantly higher mechanical performance of the compatibilized samples.

Similar effects regarding the use of a compatibilizing agent for microalgae in thermoplastic matrices were reported also for spirulina/poly(butylene succinate) (PBS) composites with MA-grafted PBS (PBS-g-MA) as the compatibilizer.<sup>300</sup> Composites with 15–50 wt% spirulina, plasticized with 15 wt% water and 10 wt% glycerol, and melt mixed in the PBS matrix with and without the compatibilizer show that the introduction of an MA-based compatibilizer improves the interfacial adhesion between the two phases. This improvement is documented from morphological observations and the formation of an ester bond between the two components, in addition to the mechanical tests showing a higher strength and modulus of the compatibilized composites. Specifically, increasing amounts of spirulina gradually increase the modulus

which, at the maximum spirulina amount of 50 wt%, is enhanced by 150% in the compatibilized samples and 100% in the non-compatibilized samples. The tensile strength decreases progressively to a maximum loss of 30% and 67%, respectively for the compatibilized and not samples. At the maximum spirulina content, both samples, with and without PBS-g-MA have an elongation to break below 10%, when pure PBS has over 1000%.

Bioplastics from 100% *Chlorella vulgaris* (CV) and *Spirulina platensis* (SP) biomatter, have also been demonstrated through heated compression molding.<sup>301</sup> The tensile properties of the molded bioplastics show a 200–300 MPa Young's modulus and a 2–7 MPa tensile strength and 1%–3% elongation to break, with slightly higher values for all properties for the pure CV compared to SP. Because these fully biomatter-based materials do not melt upon heating like synthetic thermoplastics, the use of either a plasticizer or a thermoplastic host matrix is necessary to process them by only melt mixing (without the pressure element). In this example of pure microalgae bioplastics, it was demonstrated that blending these two types of cell biomatter with glycerol to create

plasticized composites allows for an increase in the extensibility but reduction of modulus and strength in both types of biomatter. The glycerol-plasticized samples with the best properties for *CV* have 72% lower modulus, 80% lower strength and 53% higher elongation to break compared to un-plasticized samples, while for *SP* the modulus and strength reductions are 37% and 61%, respectively, and the strain to break is almost 80% higher. Introducing biomatter with and without glycerol at 20%–80% in polyethylene (PE) shows that a 4:1 ratio of biomatter to glycerol leads to more homogeneous composites and the mechanical properties follow roughly (not exactly) the rule of mixtures with higher PE content leading to higher strength, modulus and elongation to break. The 65:24 wt% PE to *CV* with 12.5% glycerol has the highest mechanical properties in the *CV* biocomposites while for *SP* the 50:37.5:12.5 PE to *SP* to glycerol are the optimal loading for maximizing mechanical performance and processability at minimum PE amount.

A recent report shows that the cell wall starch of some microalgal species can be utilized to bind together the cell biomatter, eliminating the need for a thermoplastic host matrix to create algae bioplastics with extrusion.<sup>302</sup> Screening 10 green microalgae species, the authors found that *C. reinhardtii* was able to produce the maximum amount of starch, up to 49 wt%, after being cultured in a sulfur-deprived medium. The high starch amount in presence of glycerol (30 wt% used in this case) is found to demonstrate a plasticization behavior, only when a sufficient amount of energy is supplied to disrupt the cell walls and release the cell contents. A twin-screw extruder operating at 120°C was able to provide the necessary conditions for such a plasticization as demonstrated through observations of the homogeneous morphology of the extruded filaments.

Macroalgae species have also been used to create bioplastics.<sup>303–305</sup> Powderized *Ulva armoricana* (*Ulva*) mixed with poly(vinyl alcohol) (PVA) at concentration up to 50 wt% has been reported,<sup>303</sup> in which a progressive significant increase in Young's modulus with the increase of *Ulva* concentration is noted. Specifically, the modulus increases up to 12 times (from 50 to almost 600 MPa) for *Ulva* contents up to 30 wt%. For higher concentrations modulus is reduced to 250 MPa (still higher than pure PVA). The tensile strength is not affected for concentrations up to 30 wt% and decreases for higher *Ulva* content. The extensibility of PVA is significantly (and progressively) reduced with the increasing algae filler amount. The effects of plasticizing the mixtures with glycerol shows an increase in the extensibility of the composites, nearly doubling it when incorporated to amounts lower than 10%. The introduction of starch, which acts as a reinforcement or compatibilizer between PVA and *Ulva*,

improves the strength and modulus progressively when introduced in amounts up to 20 wt%. Higher starch concentrations lead to decreased properties. When *Ulva* is introduced in polypropylene (PP) at concentrations up to 50 wt%, similar results are reported.<sup>305</sup> The algae fillers improve the tensile and bending modulus of PP, which progressively increase up to 80% higher values than pure PP for the 50:50 composite, however they do not affect the tensile strength. Including a 2% of urethane-based thermoplastic elastomer (TPE) as a compatibilizer between the biomatter and PP does not affect strength and stiffness but greatly improves the extensibility of the composite (from about 10% without TPE to 110% with TPE). The morphology of the compatibilized blends is more homogeneous, which is not really reflected on their strength and stiffness properties. However, the better adhesion between the biomatter and PP in presence of TPE is demonstrated in the significantly reduced water uptake of that composite, which after 120 h of soaking only uptakes about 0.4% water versus the uncompatibilized composite which uptakes 1.2%–1.6%.

Different types of algae (green, red and brown—species not reported, but all were ocean harvested) powdered and used as filler on PLA at concentrations 2, 20 and 40 wt%, interestingly show the same effects in terms of influencing the mechanical properties of PLA—even the numerical values are almost indistinguishable.<sup>304</sup> The PLA/algae composites show a progressive decrease of tensile strength, which at the 40 wt% algae is about half the value of pure PLA. An initial decrease in elastic modulus for 2 and 20 wt% of algae, is followed by an increase of about 40% for the 40 wt% composite. The elongation to break progressively decreases from 3.5% to 1%–1.5% as algae content increases. The poor interfacial adhesion between the two phases is evident from the morphological observations presented in this work, which supports the reduction in strength for the majority of the composites.

Jantasrirad et al.<sup>306</sup> recently showed that the use of sonicated brown algae filler in a starch biopolymer matrix at 10 wt% filler concentration led to 330% and 230% improvements in the strength compared to neat starch biopolymer and the equivalent biocomposite with non-sonicated filler, respectively. The improvements in reinforcing effects following sonication of the algal filler suggests that physical processing to the filler can offer an alternative viable strategy to improve the performance of biocomposites. This effect was further studied by Liao et al.<sup>285</sup> in spirulina-PLA composites (see Figure 12E). The authors of this study showed that the use of sonicated spirulina filler in PLA, at PLA-spirulina proportions from 100:5 to 100:30, increased the strength of composites from 8% to 25% compared to their control

biocomposite counterparts with non-sonicated filler. The paper also reported different responses to water/moisture uptake by composites with and without sonicated filler. Water-induced filler plasticization following 24 h of water immersion resulted in 65% and 94% improvements in elongation to break and toughness in the spirulina-PLA composite with sonicated filler at 100:10 filler concentration, while only amounted to 10.6% and 18% corresponding improvements in the composite with the same concentration of non-sonicated filler.<sup>285</sup> The incompatibility of algal biomatter with the (non-compatibilized) hydrophobic thermoplastics is demonstrated through the poor interfacial adhesion seen through SEM images in the featured papers.

In summary, even without improving the filler-matrix adhesion via compatibilization, the incorporation of cellulose-rich macroalgae improve the elastic modulus in low-modulus thermoplastics such as poly(vinyl alcohol) (PVA), polypropylene (PP), and thermoplastic starch (TPS), while this improvement is not observed in high-modulus thermoplastics such as PLA until a significant amount of algae filler is introduced. On the other hand, microalgae tend to reduce the elastic modulus in thermoplastics without any compatibilization. In general, a decrease in strength is expected with the incorporation of algal filler into a thermoplastic, irrespective of the species of algae used. When the bonding between the matrix and biomatter is promoted through the use of a compatibilizer, unicellular algae also improve the modulus of the thermoplastics discussed here, while reducing the strength and extensibility. Case studies agree that if interfacial adhesion is improved, through the use of compatibilizing agents, all mechanical properties are generally improved compared to the non-compatibilized systems. Small polyols such as glycerol have been widely used in algae-polymer systems as plasticizer to improve the extensibility of composites, while maleic anhydride has been the most popular compatibilizer to improve the filler-matrix adhesion. Physical processing such as sonication has been explored as another approach to improve the properties of algae biocomposites, and has been shown to dramatically enhance certain effects/mechanisms imparted on the matrix material by the incorporation of algal filler.

#### 4.5.3 | Printing with algae

Two-dimensional and three-dimensional printing options offer solutions to fabricate algae-based materials in complex geometrical shapes. For example, Balasubramanian et al.<sup>286</sup> propose a printing process of a bio-ink composed of microalgae encapsulated within an alginate hydrogel

matrix (presented in Figure 12F). To improve the mechanical robustness of these millimetrically-resolved samples, bacterial cellulose is used as a substrate to ensure physical integrity under loading by conferring strength, toughness, and flexibility. Interestingly, the authors report an improvement of mechanical properties after the bioprinting: the tensile strength reaches up to ~110 MPa for the bacterial cellulose substrate with microalgae-alginate bioprint, whereas the neat-bacterial cellulose substrate has a strength of 80 MPa. Using this approach, regeneration is also made possible by reusing an existing sample to print additional living materials.

In another study, Fredricks et al.<sup>231</sup> made use of pneumatic direct ink writing (DIW) to 3D-print pure biomatter-based samples (see Figure 12G). They printed and dried slurries composed only of (ceased) *Spirulina platensis* (spirulina) microalgae powder, water, and microcrystalline  $\alpha$ -cellulose (CF). Slurries were prepared with 1.2–2.0 weight ratio of water:spirulina and printed into 1.5 cm length cubes. The printed wet samples were then dried following three different approaches: (i) oven-drying (60°C), (ii) frozen and then lyophilized (freeze-dried), or (iii) desiccated in a chamber at 0% relative humidity. Only lyophilized samples remained uncracked after drying due to increased warping stresses inherent in the other drying processes. They found that introducing as little as 1 wt% CF into the slurry prevented the drying-induced cracking in all samples and reduced post-drying shrinkage. Increased filler weight fraction improved the mechanical performance of all samples. For example, at 20 wt% CF addition, the compressive strength and strain to break improved by a factor 8.2 and almost 4, respectively, compared to the base values of pure spirulina freeze-dried samples (base strength of 0.8 MPa and elongation to break of 12.1%). The increased compressive strengths from 1 to 20 wt% CF were remarkable in the oven-dried (OD) and desiccated (DD) samples as well; OD: 0.7  $\rightarrow$  10.3 MPa, DD: 3.2  $\rightarrow$  16.4 MPa. Overall, the composite structures had densities ranging from 0.5 to 1.0 g/cm<sup>3</sup> with compressive strengths ranging from 1 to 15 MPa and strains to break of 15%–50%.

## 5 | CIRCULAR AND SUSTAINABLE BIOECONOMY

While the idea of sustainability has surged with the advent of the United Nations Sustainable Development Goals (UNSDGs), global climate commitments and the rise in environmental, social, and governance (ESGs), the concept of sustainability dates back 30 years and has its roots in social justice, conservationism, internationalism and other past movements.<sup>307</sup> By the end of the

twentieth century, many of these ideas had culminated in what today is known as “sustainable development,” as defined in the 1987 Brundtland Report for the United Nations: Fulfilling the needs of current generations without compromising the needs of future generations.<sup>308</sup>

Although the actual principles of sustainability encompass a wide array of environmental, social, and economic factors, the general understanding and application of sustainability has primarily centered on a narrow subset of environmental aspects within a contracted life cycle boundary (e.g., CO<sub>2</sub> emissions during the manufacturing phase). Sustainability in its purest sense evaluates, quantifies and balances all three foundational pillars—environment, society and economy. Absent an understanding of the relationship to the complete system, objects or actions in isolation cannot be deemed sustainable. The development and introduction of biopolymers into the market, for instance, is not sustainable without a complete assessment of the social, environmental and economic implications across the material's entire life cycle from “cradle to grave” or “cradle to cradle” in a circular, regenerative future. This comprehensive understanding of the risks, trade-offs and unintended consequences, from a life cycle perspective, across the entire value chain, is what provides insights of a material's sustainability profile.

When researching and developing biopolymers, it is critical to design with the full life cycle in mind, in particular end-of-life pathways, a commonly overlooked aspect. Ideally, early stages of development should involve research and collaboration with downstream entities to understand end-of-life recovery options and applications in secondary markets, reprocessing or recycling systems. Mechanical performance and structural properties are important features when designing biopolymers. However, other facets require equal consideration as biomaterials are developed and scaled, such as land use from sourcing, water and energy requirements, water quality, chemical inputs for processing and purification, waste generation and transportation across every segment of the value chain, biodiversity loss, geopolitics, supply chain risks, worker health and safety, quality of life, fair trade, and so forth. Appropriately scoped life cycle assessments, that combine a “cradle-to-cradle” boundary and include a wider range of environmental considerations, life cycle costing and social assessment will provide a more holistic view of sustainability. Sustainability approached from this broad and fundamental lens can expose potential risk-shifting and lead to greater resilience and long-term system balance.

Another concept coming into focus and integrated into sustainability discussions is the circular economy, an economic system based on resource efficiency and the

reuse and regeneration of materials or products.<sup>309</sup> In a bio-based economy, economic activity involves the use of biological resources, technologies, processes and methods to provide value-added products, goods, services and energy in a sustainable manner to all economic sectors.<sup>310</sup> In a circular bioeconomy, natural capital is renewable and sustainably sourced, produced, managed, recovered and reused as much as possible across its entire life cycle.<sup>311</sup> Circular biopolymers are one probable pathway for decoupling economic growth from the consumption of finite resources by sustainably sourcing feedstocks and building end-of-life recovery pathways that recapture polymer material value after use.<sup>312</sup> This approach includes bio-based material innovations sourced from renewable feedstocks that are waste byproducts and coupling material innovations with complementary end-of-life “waste” management and recycling systems that create added value in organics processing infrastructure. A circular bioeconomy is most effective when working symbiotically across the supply chain to create value. Connecting R&D activities with downstream entities provides opportunities for biopolymers to be kept in circulation as a resource and at an economic value, creating the demand pull for material integration into circular secondary markets (life extension pathways through high-value reuse and recycling, remanufacture, upgrading, etc.). A circular bioeconomy is not sustainable by default. Therefore, circular materials and innovations must be measured across the entire life cycle to ensure it does not offset social, environmental or economic gains.

## 6 | CHALLENGES AND FUTURE DIRECTIONS

Hierarchical biopolymer-based materials provide a versatile platform for manufacturing new biocomposite materials with controllable mechanical performance and reduced environmental, social, and economic impacts. Structural biopolymers such as cellulose, chitin and protein-based  $\beta$ -sheet structured polymers, have been explored both as fillers in biocomposite materials, as well as main matrix materials, capitalizing on their vast network of macromolecular interactions. When used as a matrix, such biopolymers can effectively utilize their interactions to establish a hierarchical self-bonded backbone of exceptionally high stiffness, strength and toughness that is comparable to engineering polymers. Controlling the biopolymer morphology (aspect ratio), degree of polymerization, and orientation, allows tuning of their interactions at the molecular- and nano-scales, which ultimately governs the macroscopic behavior and fracture of those entirely biobased materials.



Structural biopolymers are obtained from biomatter through extraction and homogenization processes, which often require excessive chemical and thermo-mechanical treatments, which need to be taken into consideration when discussing the environmental impact of such materials. In addition, the effects of each processing step on the composition and morphology of the extracted biopolymers are critical, and should be carefully evaluated. For example, we discussed literature-reported results which demonstrate that extraction processes effectively reduce the polymer chain length and aspect ratio, which leads to inferior performance, compared to the native biopolymer state.

Another aspect that requires consideration, and impacts the sustainability of biopolymer-based materials, is the biomatter sourcing, logging and transportation. The biopolymer extraction and processing yield and associated costs constitute another set of considerations, which currently limit the applicability of biopolymers in industrial-scale applications. Examples like bacterial cellulose which show incredible promise as a high purity, high aspect ratio and, subsequently, high strength, stiffness and toughness nanocellulose, are yet to be produced at scale due to prohibiting manufacturing and processing costs and low yield considerations.

When used as fillers, the inherent hydrophilicity of biopolymers often leads to poor surface interactions and adhesion with common synthetic matrix materials like hydrophobic plastics, or to detrimental biopolymer aggregation. This can and has been compensated by surface treatments of biopolymers or the use of compatibilizing agents, which creates the need for yet another processing step. Another effect of the natural hydrophilicity of unprocessed biopolymers, is the often undesirable water sensitivity they impart to any biocomposite material they are introduced into. If that property is indeed undesirable, surface treatments or the use of other additives or coatings ought to be considered. For example, literature reports demonstrate the significant effects of humidity on cellulose films, with strength variations reaching approximately 1 order of magnitude as the same film is tested wet or entirely dry. Moreover, understanding the biodegradation pathways enabled from the use of biopolymers in biocomposites requires attention. The non-standardized results reported in literature, create the need for systematic characterization procedures to assess the positive effects of biopolymers in improving the biodegradation profiles of biocomposite materials.

Finally, a new class of biomatter-based biocomposite materials is discussed in this review. Unprocessed biomatter from plants, algae, fungi, or microbes contains the structural biopolymers mixed with non-structural organic materials, organized in hierarchical structures. Such

unprocessed natural biocomposites can be used as matrix materials, utilizing self-bonding based on similar principles as discussed above. In addition, biomatter can be used as a filler offering less significant mechanical reinforcement compared to the extracted pure biopolymers, but at an advantage of less energy-intensive processing. Cell-based materials in particular show incredible promise as they can serve as a platform to create tunable, entirely biobased materials and biocomposites. Examples such as mycelium foams have already reached the market, especially in insulation and low strength packaging, demonstrating the potential of this new biopolymer matrix materials class. Bacteria and plant cell based matrix materials have been able to reach higher densities and mechanical properties compared to mycelium foams, aiming to expand the target applications to potentially structural polymers and commodity plastic alternatives. Open challenges include providing a systematic understanding of the roles of each biopolymer component in raw biomatter and how their structure and functionality (in terms of role serving in the final material) can be altered by design via processing methods, in order to control the final macroscopic behavior of the obtained biomatter-based material.


## ACKNOWLEDGMENTS

The authors thank Kuotian Liao for the discussions and evaluation of the algae-based biocomposites section, Dallas Warren and Will Gottsch for their assistance with collecting mechanical property data of cellulose from literature.

## ORCID

Andrew M. Jimenez  <https://orcid.org/0000-0001-7696-9705>

Paul Grandgeorge  <https://orcid.org/0000-0002-1140-7557>

Eleftheria Roumeli  <https://orcid.org/0000-0002-2828-1428>

## REFERENCES

- [1] C. M. Rochman, M. A. Browne, B. S. Halpern, B. T. Hentschel, E. Hoh, H. K. Karapanagioti, L. M. Rios-Mendoza, H. Takada, S. Teh, R. C. Thompson, *Nature* **2013**, *494*, 169.
- [2] H. A. Leslie, M. J. M. van Velzen, S. H. Brandsma, A. D. Vethaak, J. J. Garcia-Vallejo, M. H. Lamoree, *Environ. Int.* **2022**, *163*, 107199.
- [3] S. Ling, W. Chen, Y. Fan, K. Zheng, K. Jin, H. Yu, M. J. Buehler, D. L. Kaplan, *Prog. Polym. Sci.* **2018**, *85*, 1.
- [4] A. K. Mohanty, M. Misra, L. T. Drzal Eds., *Natural Fibers, Biopolymers, and Biocomposites*, CRC Press, Boca Raton **2005**.
- [5] O. Faruk, A. K. Bledzki, H.-P. Fink, M. Sain, *Prog. Polym. Sci.* **2012**, *37*, 1552.

- [6] A. K. Mohanty, M. Misra, G. Hinrichsen, *Macromol. Mater. Eng.* **2000**, 276-277, 1.
- [7] A. K. Mohanty, S. Vivekanandhan, J.-M. Pin, M. Misra, *Science* **2018**, 362, 536.
- [8] Y. Shireesha, G. Nandipati, *Mater. Today: Proc.* **2019**, 18, 15.
- [9] P. Q. Nguyen, N.-M. D. Courchesne, A. Duraj-Thatte, P. Praveschotinunt, N. S. Joshi, *Adv. Mater.* **2018**, 30, 1704847.
- [10] B. L. Tardy, B. D. Mattos, C. G. Otoni, M. Beaumont, J. Majoinen, T. Kämäräinen, O. J. Rojas, *Chem. Rev.* **2021**, 121, 14088.
- [11] D. Nepal, S. Kang, K. M. Adstedt, K. Kanhaiya, M. R. Bockstaller, L. C. Brinson, M. J. Buehler, P. V. Coveney, K. Dayal, J. A. El-Awady, L. C. Henderson, D. L. Kaplan, S. Ketten, N. A. Kotov, G. C. Schatz, S. Vignolini, F. Vollrath, Y. Wang, B. I. Yakobson, V. V. Tsukruk, H. Heinz, *Nat. Mater.* **2023**, 22, 18.
- [12] R. J. Moon, A. Martini, J. Nairn, J. Simonsen, J. Youngblood, *Chem. Soc. Rev.* **2011**, 40, 3941.
- [13] I. R. Campbell, M.-Y. Lin, H. Iyer, M. Parker, J. L. Fredricks, K. Liao, A. M. Jimenez, P. Grandgeorge, E. Roumeli, *Annu. Rev.* **2023**, 53, 53.
- [14] F. Lundell, L. D. Söderberg, P. H. Alfredsson, *Annu. Rev. Fluid Mech.* **2011**, 43, 195.
- [15] D. Klemm, B. Heublein, H.-P. Fink, A. Bohn, *Angew. Chem. Int. Ed.* **2005**, 44, 3358.
- [16] Q. Meng, T. J. Wang, *Appl. Mech. Rev.* **2019**, 71, 71.
- [17] M. Wohlert, T. Benselfelt, L. Wågberg, I. Furó, L. A. Berglund, J. Wohlert, *Cellulose* **2022**, 29, 1.
- [18] T. Puspasari, N. Pradeep, K.-V. Peinemann, *J. Membr. Sci.* **2015**, 491, 132.
- [19] M. Wada, H. Chanzy, Y. Nishiyama, P. Langan, *Macromolecules* **2004**, 37, 8548.
- [20] R. Wang, L. Chen, J. Zhu, R. Yang, *ChemNanoMat* **2017**, 3, 328.
- [21] A. Dufresne, J.-Y. Cavaillé, M. R. Vignon, *J. Appl. Polym. Sci.* **1997**, 64, 1185.
- [22] E. Johan Foster, R. J. Moon, U. P. Agarwal, M. J. Bortner, J. Bras, S. Camarero-Espinosa, K. J. Chan, M. J. D. Clift, E. D. Cranston, S. J. Eichhorn, D. M. Fox, W. Y. Hamad, L. Heux, B. Jean, M. Korey, W. Nieh, K. J. Ong, M. S. Reid, S. Rennecker, R. Roberts, J. Anne Shatkin, J. Simonsen, K. Stinson-Bagby, N. Wanasekara, J. Youngblood, *Chem. Soc. Rev.* **2018**, 47, 2609.
- [23] P. Ross, R. Mayer, M. Benziman, *Microbiol. Mol. Biol. Rev.* **1991**, 55, 35.
- [24] Z. A. Popper, M. G. Tuohy, *Plant Physiol.* **2010**, 153, 373.
- [25] D. J. Cosgrove, *Nat. Rev. Mol. Cell Biol.* **2005**, 6, 850.
- [26] D. J. Cosgrove, *Plant Physiol.* **2018**, 176, 16.
- [27] A. J. Bidhendi, A. Geitmann, *J. Exp. Bot.* **2015**, 67, 449.
- [28] Y. B. Park, D. J. Cosgrove, *Plant Physiol.* **1933**, 2012, 158.
- [29] M.-C. Maaß, S. Saleh, H. Militz, C. A. Volkert, *Adv. Mater.* **2020**, 32, 1907693.
- [30] L. J. Gibson, *J. R. Soc. Interface* **2012**, 9, 2749.
- [31] I. Burgert, P. Fratzl, *Integr. Comp. Biol.* **2009**, 49, 69.
- [32] R. Zhong, D. Cui, Z.-H. Ye, *New Phytol.* **2019**, 221, 1703.
- [33] P. T. Martone, K. Janot, M. Fujita, G. Wasteneys, K. Ruel, J. P. Joseleau, J. M. Estevez, *Planta* **2019**, 250, 1867.
- [34] I. Tsekos, H.-D. Reiss, E. Schnepf, *Acta Bot. Neerlandica* **1993**, 42, 119.
- [35] L. Gomez, C. Alvarez, M. Zhao, U. Tiwari, J. Curtin, M. Garcia-Vaquero, B. Tiwari, *Carbohydr. Polym.* **2020**, 248, 116784.
- [36] M. Gama, P. Gatenholm, D. Klemm, *Bacterial Nanocellulose: A Sophisticated Multifunctional Material*, CRC Press, Boca Raton, FL **2016**.
- [37] S. P. Lin, I. Loira Calvar, J. M. Catchmark, J. R. Liu, A. Demirci, K. C. Cheng, *Cellulose* **2013**, 20, 2191.
- [38] K.-Y. Lee, G. Buldum, A. Mantalaris, A. Bismarck, *Macromol. Biosci.* **2014**, 14, 10.
- [39] L. Zhang, L. Fu, H.-F. Wang, B. Yang, *Sci. Rep.* **2017**, 7, 44319.
- [40] A. Gupta, A. Khodayari, A. C. Van Duin, U. Hirn, A. W. Van Vuure, D. Seveno, *Biomacromolecules* **2022**, 23, 2243.
- [41] A. Paajanen, S. Ceccherini, T. Maloney, J. A. Ketoja, *Cellulose* **2019**, 26, 5877.
- [42] T. Dumitrică, *Carbohydr. Polym.* **2020**, 230, 115624.
- [43] Z. Zhao, O. E. Shklyayev, A. Nili, M. N. A. Mohamed, J. D. Kubicki, V. H. Crespi, L. Zhong, *J. Phys. Chem. A* **2013**, 117, 2580.
- [44] K. Ruel, Y. Nishiyama, J. P. Joseleau, *Plant Sci.* **2012**, 193-194, 48.
- [45] N. D. Sanandhiya, K. Prasad, R. Meena, A. K. Siddhanta, *Nat. Prod. Commun.* **2010**, 5, 603.
- [46] H. Zhu, S. Zhu, Z. Jia, S. Parvinian, Y. Li, O. Vaaland, L. Hu, T. Li, *Proc. Natl. Acad. Sci. U. S. A.* **2015**, 112, 8971.
- [47] C. Djahedi, M. Bergensträhle-Wohlert, L. A. Berglund, J. Wohlert, *Cellulose* **2016**, 23, 2315.
- [48] A. Pakzad, J. Simonsen, P. A. Heiden, R. S. Yassar, *J. Mater. Res.* **2012**, 27, 328.
- [49] M. Poletto, V. Pistor, A. J. Zattera, *Cellul-Fundam. Aspects* **2013**, 2, 45.
- [50] K. Watanabe, M. Tabuchi, Y. Morinaga, F. Yoshinaga, *Cellulose* **1998**, 5, 187.
- [51] B. B. Hallac, A. J. Ragauskas, *Biofuels Bioprod. Biorefin.* **2011**, 5, 215.
- [52] M. Yanagisawa, I. Shibata, A. Isogai, *Cellulose* **2005**, 12, 151.
- [53] C. T. Brett, *Int. Rev. Cytol.* **2000**, 199, 161.
- [54] S. S. Maleki, K. Mohammadi, K.-S. Ji, *Sci. World J.* **2016**, 2016, 8641373.
- [55] M. Matsuo, C. Sawatari, Y. Iwai, F. Ozaki, *Macromolecules* **1990**, 23, 3266.
- [56] T. Nishino, K. Takano, K. Nakamae, *J. Polym. Sci. Part B: Polym. Phys.* **1995**, 33, 1647.
- [57] R. R. Lahiji, X. Xu, R. Reifenberger, A. Raman, A. Rudie, R. J. Moon, *Langmuir* **2010**, 26, 4480.
- [58] I. Diddens, B. Murphy, M. Krisch, M. Müller, *Macromolecules* **2008**, 41, 9755.
- [59] I. Sakurada, Y. Nukushina, T. Ito, *J. Polym. Sci.* **1962**, 57, 651.
- [60] R. Wagner, R. Moon, J. Pratt, G. Shaw, A. Raman, *Nanotechnology* **2011**, 22, 455703.
- [61] T. Saito, R. Kuramae, J. Wohlert, L. A. Berglund, A. Isogai, *Biomacromolecules* **2013**, 14, 248.
- [62] S. J. Eichhorn, J. Sirichaisit, R. J. Young, *J. Mater. Sci.* **2001**, 36, 3129.
- [63] G. Guhados, W. Wan, J. L. Hutter, *Langmuir* **2005**, 21, 6642.
- [64] Y.-C. Hsieh, H. Yano, M. Nogi, S. Eichhorn, *Cellulose* **2008**, 15, 507.
- [65] A. Šturcová, G. R. Davies, S. J. Eichhorn, *Biomacromolecules* **2005**, 6, 1055.

- [66] S. Iwamoto, W. Kai, A. Isogai, T. Iwata, *Biomacromolecules* **2009**, *10*, 2571.
- [67] K. Tashiro, M. Kobayashi, *Polymer* **1991**, *32*, 1516.
- [68] K. Radotić, C. Roduit, J. Simonović, P. Hornitschek, C. Fankhauser, D. Mutavdžić, G. Steinbach, G. Dietler, S. Kasas, *Biophys. J.* **2012**, *103*, 386.
- [69] A. J. Bidhendi, A. Geitmann, *J. Exp. Bot.* **2019**, *70*, 3615.
- [70] J. Fan, A. Anastassiou, C. W. Macosko, E. B. Tadmor, *Polymer* **2020**, *196*, 122477.
- [71] J. Fan, A. Anastassiou, C. W. Macosko, E. B. Tadmor, *Tribol. Lett.* **2021**, *69*, 1.
- [72] J. Fan. *Ph.D. Thesis*, University of Minnesota **2020**.
- [73] S. L. Mayo, B. D. Olafson, W. A. Goddard, *J. Phys. Chem.* **1990**, *94*, 8897.
- [74] S. J. Weiner, P. A. Kollman, D. A. Case, U. C. Singh, C. Ghio, G. Alagona, S. Profeta, P. Weiner, *J. Am. Chem. Soc.* **1984**, *106*, 765.
- [75] J. Wang, R. M. Wolf, J. W. Caldwell, P. A. Kollman, D. A. Case, *J. Comput. Chem.* **2004**, *25*, 1157.
- [76] W. L. Jorgensen, J. Tirado-Rives, *J. Am. Chem. Soc.* **1988**, *110*, 1657.
- [77] W. L. Jorgensen, D. S. Maxwell, J. Tirado-Rives, *J. Am. Chem. Soc.* **1996**, *118*, 11225.
- [78] M. J. Hwang, T. Stockfisch, A. Hagler, *J. Am. Chem. Soc.* **1994**, *116*, 2515.
- [79] H. Sun, *J. Comput. Chem.* **1994**, *15*, 752.
- [80] H. Sun, *J. Phys. Chem. B* **1998**, *102*, 7338.
- [81] H. Sun, P. Ren, J. Fried, *Comput. Theor. Polym. Sci.* **1998**, *8*, 229.
- [82] A. C. Van Duin, S. Dasgupta, F. Lorant, W. A. Goddard, *J. Phys. Chem. A* **2001**, *105*, 9396.
- [83] O. T. Unke, S. Chmiela, H. E. Sauceda, M. Gastegger, I. Poltavsky, K. T. Schüt, A. Tkatchenko, K.-R. Müller, *Chem. Rev.* **2021**, *121*, 10142.
- [84] I. Sakurada, T. Ito, K. Nakamae, *Die Makromol. Chem.: Macromol. Chem. Phys.* **1964**, *75*, 1.
- [85] I. Satcurada, T. Ito, K. Nakamae, *J. Polym. Sci. Part C: Polym. Symp.* **1967**, *15*, 75.
- [86] X. Wu, R. J. Moon, A. Martini, *Cellulose* **2013**, *20*, 43.
- [87] F. L. Dri, L. G. Hector, R. J. Moon, P. D. Zavattieri, *Cellulose* **2013**, *20*, 2703.
- [88] K. Tashiro, M. Kobayashi, *Polym. Bull.* **1985**, *14*, 213.
- [89] S. Reiling, J. Brickmann, *Macromol. Theory Simul.* **1995**, *4*, 725.
- [90] F. Tanaka, T. Iwata, *Cellulose* **2006**, *13*, 509.
- [91] J. Ketoja, S. Paavilainen, J. L. McWhirter, T. Róg, J. Järvinen, I. Vattulainen, *Nord. Pulp Pap. Res. J.* **2012**, *27*, 282.
- [92] M. G. Ramezani, B. Golchinfar, *J. Compos. Sci.* **2019**, *3*, 57.
- [93] X. Wu, R. J. Moon, A. Martini, *Cellulose* **2014**, *21*, 2233.
- [94] I. H. Sahputra, A. Alexiadis, M. J. Adams, *J. Polym. Sci. Part B: Polym. Phys.* **2019**, *57*, 454.
- [95] A. Aabloo, A. D. French, *Macromol. Theory Simul.* **1994**, *3*, 185.
- [96] S. Eichhorn, G. Davies, *Cellulose* **2006**, *13*, 291.
- [97] Y. Nishiyama, P. Langan, H. Chanzy, *J. Am. Chem. Soc.* **2002**, *124*, 9074.
- [98] Y. Nishiyama, J. Sugiyama, H. Chanzy, P. Langan, *J. Am. Chem. Soc.* **2003**, *125*, 14300.
- [99] V. Finkenstadt, R. Millane, *Macromolecules* **1998**, *31*, 7776.
- [100] F. Khan, N. Pilpel, S. Ingham, *Powder Technol.* **1988**, *54*, 161.
- [101] B. C. Hancock, S.-D. Clas, K. Christensen, *Int. J. Pharm.* **2000**, *209*, 27.
- [102] S. Nikolov, M. Petrov, L. Lymperakis, M. Friák, C. Sachs, H.-O. Fabritius, D. Raabe, J. Neugebauer, *Adv. Mater.* **2010**, *22*, 519.
- [103] M. Rinaudo, *Prog. Polym. Sci.* **2006**, *31*, 603.
- [104] S. M. Bowman, S. J. Free, *BioEssays* **2006**, *28*, 799.
- [105] P. H. Fesel, A. Zuccaro, *Fung. Genet. Biol.* **2016**, *90*, 53.
- [106] N. A. R. Gow, J.-P. Latge, C. A. Munro, *Microbiol. Spect.* **2017**, *5*, 267.
- [107] X. Kang, A. Kirui, A. Muszyński, M. C. D. Widanage, A. Chen, P. Azadi, P. Wang, F. Mentink-Vigier, T. Wang, *Nat. Commun.* **2018**, *9*, 1.
- [108] J.-P. Latgé, *Mol. Microbiol.* **2007**, *66*, 279.
- [109] M. N. V. R. Kumar, *React. Funct. Polym.* **2020**, *46*, 1.
- [110] M.-K. Jang, B.-G. Kong, Y.-I. Jeong, C. H. Lee, J.-W. Nah, *J. Polym. Sci. Part A: Polym. Chem.* **2004**, *42*, 3423.
- [111] T. Yui, N. Taki, J. Sugiyama, S. Hayashi, *Int. J. Biol. Macromol.* **2007**, *40*, 336.
- [112] Y. Ogawa, R. Hori, U.-J. Kim, M. Wada, *Carbohydr. Polym.* **2011**, *83*, 1213.
- [113] J. Blackwell, M. Weih, *J. Mol. Biol.* **1980**, *137*, 49.
- [114] B. Duan, Y. Huang, A. Lu, L. Zhang, *Prog. Polym. Sci.* **2018**, *82*, 1.
- [115] T. Nishino, R. Matsui, K. Nakamae, *J. Polym. Sci. Part B: Polym. Phys.* **1999**, *37*, 1191.
- [116] Y. Bamba, Y. Ogawa, T. Saito, L. A. Berglund, A. Isogai, *Biomacromolecules* **2017**, *18*, 4405.
- [117] W. Xu, P. J. Mulhern, B. L. Blackford, M. H. Jericho, I. Templeton, *Scan. Microsc.* **1994**, *8*, 499.
- [118] A. Wei, J. Fu, F. Guo, *J. Mater. Sci.* **2021**, *56*, 12048.
- [119] L. Zhao, D. Schaefer, H. Xu, S. J. Modi, W. R. LaCourse, M. R. Marten, *Biotechnol. Prog.* **2005**, *21*, 292.
- [120] S. M. Stocks, C. R. Thomas, *Biotechnol. Bioeng.* **2001**, *73*, 370.
- [121] A. Smith, K. Moxham, A. Middelberg, *Chem. Eng. Sci.* **2000**, *55*, 2043.
- [122] S. Xiao, S. Xiao, F. Gräter, *Phys. Chem. Chem. Phys.* **2013**, *15*, 8765.
- [123] S. Keten, Z. Xu, B. Ihle, M. J. Buehler, *Nat. Mater.* **2010**, *9*, 359.
- [124] R. Sabaté, S. Ventura, in *Protein Supersecondary Structures* (Ed: A. E. Kister), Humana Press, Totowa, NJ **2013**, p. 237, Ch.15, ISBN 9781627033329.
- [125] S. Xiao, W. Stacklies, M. Cetinkaya, B. Markert, F. Gräter, *Biophys. J.* **2009**, *96*, 3997.
- [126] Q. Meng, B. Li, T. Li, X.-Q. Feng, *J. Mech. Phys. Solids* **2017**, *103*, 22.
- [127] C. Vepari, D. L. Kaplan, *Prog. Polym. Sci.* **2007**, *32*, 991.
- [128] C. Belbéoch, J. Lejeune, P. Vroman, F. Salaün, *Environ. Chem. Lett.* **2021**, *19*, 1737.
- [129] F. Sehna, C. Craig, in *Encyclopedia of Insects*, 2nd ed. (Eds: V. H. Resh, R. T. Cardé), Academic Press, San Diego **2009**, p. 921, ISBN 978-0-12-374144-8.
- [130] G. Li, P. Zhou, Z. Shao, X. Xie, X. Chen, H. Wang, L. Chunyu, T. Yu, *Eur. J. Biochem.* **2001**, *268*, 6600.
- [131] X. Liu, K.-Q. Zhang, *Oligomerization of Chemical and Biological Compounds*, IntechOpen, Rijeka, Croatia **2014**, ISBN 9789535116172.
- [132] J. G. Hardy, T. R. Scheibel, *J. Polym. Sci. Part A: Polym. Chem.* **2009**, *47*, 3957.

- [133] N. Kronqvist, M. Sarr, A. Lindqvist, K. Nordling, M. Otkovs, L. Venturi, B. Pioselli, P. Purhonen, M. Landreh, H. Biverstål, Z. Toleikis, L. Sjöberg, C. V. Robinson, N. Pelizzi, H. Jörnvall, H. Hebert, K. Jaudzems, T. Curstedt, A. Rising, J. Johansson, *Nat. Commun.* **2017**, *8*, 15504.
- [134] V. Volkov, A. V. Ferreira, A. Cavaco-Paulo, *Macromol. Mater. Eng.* **2015**, *300*, 1199.
- [135] Y. Cheng, L.-D. Koh, D. Li, B. Ji, M.-Y. Han, Y.-W. Zhang, *J. R. Soc. Interface* **2014**, *11*, 20140305.
- [136] E. R. Johnston, Y. Miyagi, J.-A. Chuah, K. Numata, M. A. Serban, *ACS Biomater. Sci. Eng.* **2018**, *4*, 2815.
- [137] P. Aramwit, in *Wound Healing Biomaterials* (Ed: M. S. Ågren), Woodhead Publishing, Sawston, Cambridge **2016**, p. 3, ISBN 978-1-78242-456-7.
- [138] M. Hudspeth, X. Nie, W. Chen, R. Lewis, *Biomacromolecules* **2012**, *13*, 2240.
- [139] A. Taglialegna, I. Lasa, J. Valle, *J. Bacteriol.* **2016**, *198*, 2579.
- [140] D. Romero, R. Kolter, *Int. Microbiol.* **2014**, *17*, 65.
- [141] S. L. Rouse, S. J. Matthews, M. S. Dueholm, *J. Mol. Biol.* **2018**, *430*, 3685.
- [142] A. Taglialegna, S. Navarro, S. Ventura, J. A. Garnett, S. Matthews, J. R. Penades, I. Lasa, J. Valle, *PLoS Pathog.* **2016**, *12*, 1.
- [143] P. Di Martino, *Trends Microbiol.* **2016**, *24*, 682.
- [144] G. Zeng, B. S. Vad, M. S. Dueholm, G. Christiansen, M. Nilsson, T. Tolker-Nielsen, P. H. Nielsen, R. L. Meyer, D. E. Otzen, *Front. Microbiol.* **2015**, *6*, 1.
- [145] T. P. J. Knowles, M. J. Buehler, *Nat. Nanotechnol.* **2011**, *6*, 469.
- [146] M. Solar, M. J. Buehler, *Nanotechnology* **2014**, *25*, 105703.
- [147] P. Alam, *Adv. Nat. Sci.: Nanosci. Nanotechnol.* **2014**, *5*, 015015.
- [148] N. Mittal, F. Ansari, K. Gowda, V. C. Brouzet, P. Chen, P. T. Larsson, S. V. Roth, F. Lundell, L. Wågberg, N. A. Kotov, L. D. Söderberg, *ACS Nano* **2018**, *12*, 6378.
- [149] M. Patel, D. K. Dubey, S. P. Singh, *Mater. Sci. Eng., C* **2020**, *108*, 110414.
- [150] C. Fu, Z. Shao, V. Fritz, *Chem. Commun.* **2009**, *43*, 6515.
- [151] L.-D. Koh, Y. Cheng, C.-P. Teng, Y.-W. Khin, X.-J. Loh, S.-Y. Tee, M. Low, E. Ye, H.-D. Yu, Y.-W. Zhang, M. Y. Han, *Prog. Polym. Sci.* **2015**, *46*, 86.
- [152] E. B. Tadmor, R. E. Miller, *Modeling Materials: Continuum, Atomistic and Multiscale Techniques*, Cambridge University Press, New York **2011**.
- [153] M. Patel, D. K. Dubey, S. P. Singh, *J. Mater. Sci.* **2020**, *55*, 17019.
- [154] A. Nova, S. Keten, N. M. Pugno, A. Redaelli, M. J. Buehler, *Nano Lett.* **2010**, *10*, 2626.
- [155] S. Wei, Y. Li, K. Li, C. Zhong, *Appl. Mater. Today* **2022**, *27*, 101497.
- [156] Y. Shen, G. Nyström, R. Mezzenga, *Adv. Funct. Mater.* **2017**, *27*, 1700897.
- [157] M. E. Vallejos, A. A. S. Curvelo, E. M. Teixeira, F. M. Mendes, A. J. F. Carvalho, F. E. Felissia, M. C. Area, *Ind. Crops Prod.* **2011**, *33*, 739.
- [158] X. Hu, P. Cebe, A. S. Weiss, F. Omenetto, D. L. Kaplan, *Mater. Today* **2012**, *15*, 208.
- [159] M. Henriksson, L. A. Berglund, P. Isaksson, T. Lindström, T. Nishino, *Biomacromolecules* **2008**, *9*, 1579.
- [160] S. Wang, F. Jiang, X. Xu, Y. Kuang, K. Fu, E. Hitz, L. Hu, *Adv. Mater.* **2017**, *29*, 1702498.
- [161] K. M. Håkansson, A. B. Fall, F. Lundell, S. Yu, C. Krywka, S. V. Roth, G. Santoro, M. Kvick, L. P. Wittberg, L. Wågberg, L. D. Söderberg, *Nat. Commun.* **2014**, *5*, 4018.
- [162] A. Kafy, H. C. Kim, L. Zhai, J. W. Kim, T. J. Kang, J. Kim, *Sci. Rep.* **2017**, *7*, 1.
- [163] H. Sehaqui, N. Ezekiel Mushi, S. Morimune, M. Salajkova, T. Nishino, L. A. Berglund, *ACS Appl. Mater. Interfaces* **2012**, *4*, 1043.
- [164] M. M. Rahman, A. N. Netravali, *ACS Macro Lett.* **2016**, *5*, 1070.
- [165] J. L. Fredricks, M. Parker, P. Grandgeorge, A. M. Jimenez, E. Law, M. Nelsen, E. Roumeli, *MRS Commun.* **2022**, *12*, 394.
- [166] S. Wainwright, W. Biggs, J. Currey, *Mechanical Design in Organisms*, Princeton University Press, Princeton, NJ **1982**.
- [167] N. Petersen, P. Gatenholm, *Appl. Microbiol. Biotechnol.* **2011**, *91*, 1277.
- [168] D. R. Ruka, G. P. Simon, K. M. Dean, *Carbohydr. Polym.* **2012**, *89*, 613.
- [169] W. Czaja, D. Romanovicz, R. Malcolm Brown, *Cellulose* **2004**, *11*, 403.
- [170] K.-C. Cheng, J. M. Catchmark, A. Demirci, *Cellulose* **2009**, *16*, 1033.
- [171] A. Krystynowicz, W. Czaja, A. Wiktorowska-Jeziarska, M. Gonçalves-Miśkiewicz, M. Turkiewicz, S. Bielecki, *J. Ind. Microbiol. Biotechnol.* **2002**, *29*, 189.
- [172] K. Liu, J. M. Catchmark, *Cellulose* **2018**, *25*, 2273.
- [173] K. Liu, J. M. Catchmark, *Bioresour. Technol.* **2019**, *290*, 121715.
- [174] K. Liu, J. M. Catchmark, *Carbohydr. Polym.* **2019**, *219*, 12.
- [175] K. Liu, J. M. Catchmark, *Cellulose* **2020**, *27*, 2529.
- [176] K. Chi, J. M. Catchmark, *Nanoscale* **2017**, *9*, 15144.
- [177] A. A. K. Das, J. Bovill, M. Ayesah, S. D. Stoyanov, V. N. Paunov, *J. Mater. Chem. B* **2016**, *4*, 3685.
- [178] S. Iwamoto, A. Isogai, T. Iwata, *Biomacromolecules* **2011**, *12*, 831.
- [179] S. Hooshmand, Y. Aitomäki, N. Norberg, A. P. Mathew, K. Oksman, *ACS Appl. Mater. Interfaces* **2015**, *7*, 13022.
- [180] H. C. Kim, D. Kim, J. Y. Lee, L. Zhai, J. Kim, *Int. J. Precis. Eng. Manuf. – Green Technol.* **2019**, *6*, 567.
- [181] Y. Uraki, J. Nemoto, H. Otsuka, Y. Tamai, J. Sugiyama, T. Kishimoto, M. Ubukata, H. Yabu, M. Tanaka, M. Shimomura, *Carbohydr. Polym.* **2007**, *69*, 1.
- [182] A. Putra, A. Kakugo, H. Furukawa, J. P. Gong, T. Osada, Y. Iu Uemura, M. Yamamoto, *Polym. J.* **2008**, *40*, 137.
- [183] S. Bontan, F. Robotti, P. Jayathissa, A. Hegglin, N. Bahamonde, J. A. Heredia-Guerrero, I. S. Bayer, A. Scarpellini, H. Merker, N. Lindenblatt, D. Poulikakos, A. Ferrari, *ACS Nano* **2015**, *9*, 206.
- [184] A. Putra, A. Kakugo, H. Furukawa, J. P. Gong, Y. Osada, *Polymer* **1885**, 2008, 49.
- [185] R. Prathapan, A. K. Ghosh, A. Knapp, A. Vijayakumar, N. N. J. Bogari, B. D. Abraham, A. Al-Ghabkari, A. Fery, J. Hu, *ACS Appl. Bio Mater.* **2020**, *3*, 7898.
- [186] S. Wang, T. Li, C. Chen, W. Kong, S. Zhu, J. Dai, A. J. Diaz, E. Hitz, S. D. Solares, T. Li, L. Hu, *Adv. Funct. Mater.* **2018**, *28*, 1707491.
- [187] M. M. Rahman, A. N. Netravali, *Compos. Sci. Technol.* **2016**, *136*, 85.

- [188] M. M. Rahman, A. N. Netravali, *Compos. Sci. Technol.* **2017**, *146*, 183.
- [189] M. B. Sano, A. D. Rojas, P. Gatenholm, R. V. Davalos, *Ann. Biomed. Eng.* **2010**, *38*, 2475.
- [190] H. G. Wise, H. Takana, F. Ohuchi, A. B. Dichiara, *ACS Appl. Mater. Interfaces* **2020**, *12*, 28568.
- [191] Y. Numata, T. Sakata, H. Furukawa, K. Tajima, *Mater. Sci. Eng., C* **2015**, *47*, 57.
- [192] Y. Hagiwara, A. Putra, A. Kakugo, H. Furukawa, J. P. Gong, *Cellulose* **2010**, *17*, 93.
- [193] D. Ye, C. Chang, L. Zhang, *Biomacromolecules* **2019**, *20*, 1989.
- [194] D. Zhao, J. Huang, Y. Zhong, K. Li, L. Zhang, J. Cai, *Adv. Funct. Mater.* **2016**, *26*, 6279.
- [195] S.-T. Chang, L.-C. Chen, S.-B. Lin, H.-H. Chen, *Food Hydrocolloids* **2012**, *27*, 137.
- [196] Y. Chen, X. Zhou, Q. Lin, D. Jiang, *Cellulose* **2014**, *21*, 2679.
- [197] A. Nakayama, A. Kakugo, J. Gong, Y. Osada, M. Takai, T. Erata, S. Kawano, *Adv. Funct. Mater.* **2004**, *14*, 1124.
- [198] H. Dong, J. F. Snyder, K. S. Williams, J. W. Andzelm, *Biomacromolecules* **2013**, *14*, 3338.
- [199] H. Dong, J. F. Snyder, D. T. Tran, J. L. Leadore, *Carbohydr. Polym.* **2013**, *95*, 760.
- [200] H. Françon, Z. Wang, A. Marais, K. Mystek, A. Piper, H. Granberg, A. Malti, P. Gatenholm, P. A. Larsson, L. Wågberg, *Adv. Funct. Mater.* **2020**, *30*, 1909383.
- [201] J. Yao, S. Chen, Y. Chen, B. Wang, Q. Pei, H. Wang, *ACS Appl. Mater. Interfaces* **2017**, *9*, 20330.
- [202] F. Quero, M. Nogi, K.-Y. Lee, G. V. Poel, A. Bismarck, A. Mantalaris, H. Yano, S. J. Eichhorn, *ACS Appl. Mater. Interfaces* **2011**, *3*, 490.
- [203] D. Hu, Y. Cui, K. Mo, J. Wang, Y. Huang, X. Miao, J. Lin, C. Chang, *Composites, Part B* **2020**, *197*, 108118.
- [204] J. Gu, J. M. Catchmark, *Cellulose* **2014**, *21*, 275.
- [205] E. Chanliaud, K. M. Burrows, G. Jeronimidis, M. J. Gidley, *Planta* **2002**, *215*, 989.
- [206] D. Mikkelsen, B. M. Flanagan, S. M. Wilson, A. Bacic, M. J. Gidley, *Biomacromolecules* **2015**, *16*, 1232.
- [207] S. E. C. Whitney, E. Wilson, J. Webster, A. Bacic, J. S. G. Reid, M. J. Gidley, *Am. J. Bot.* **2006**, *93*, 1402.
- [208] M. S. Dayal, J. M. Catchmark, *Carbohydr. Polym.* **2016**, *144*, 447.
- [209] A. J. Benítez, J. Torres-Rendon, M. Poutanen, A. Walther, *Biomacromolecules* **2013**, *14*, 4497.
- [210] Q.-F. Guan, H.-B. Yang, Z.-M. Han, L.-C. Zhou, Y.-B. Zhu, Z.-C. Ling, H.-B. Jiang, P.-F. Wang, T. Ma, H.-A. Wu, S.-H. Yu, *Sci. Adv.* **2020**, *6*, eaaz1114.
- [211] W. M. Fazli Wan Nawawi, K.-Y. Lee, E. Kontturi, R. J. Murphy, A. Bismarck, *ACS Sustainable Chem. Eng.* **2019**, *7*, 6492.
- [212] M. Jones, K. Weiland, M. Kujundzic, J. Theiner, H. Kählig, E. Kontturi, S. John, A. Bismarck, A. Mautner, *Biomacromolecules* **2019**, *20*, 3513.
- [213] N. Cohen, M. Levin, C. D. Eisenbach, *Biomacromolecules* **2021**, *22*, 993.
- [214] G. Nyström, L. Roder, M. P. Fernández-Ronco, R. Mezzenga, *Adv. Funct. Mater.* **2018**, *28*, 1703609.
- [215] D. Montroni, S. Fermani, K. Morellato, G. Torri, A. Naggi, L. Cristofolini, G. Falini, *Carbohydr. Polym.* **2019**, *207*, 26.
- [216] P. Hassanzadeh, M. Kharaziha, M. Nikkha, S. R. Shin, J. Jin, S. He, W. Sun, C. Zhong, M. R. Dokmeci, A. Khademhosseini, M. Rolandi, *J. Mater. Chem. B* **2013**, *1*, 4217.
- [217] N. E. Mushi, N. Butchosa, M. Salajkova, Q. Zhou, L. A. Berglund, *Carbohydr. Polym.* **2014**, *112*, 255.
- [218] J. Luo, L. Zhang, Q. Peng, M. Sun, Y. Zhang, H. Shao, X. Hu, *Int. J. Biol. Macromol.* **2014**, *66*, 319.
- [219] G. R. Plaza, P. Corsini, E. Marsano, J. Pérez-Rigueiro, M. Elices, C. Riekkel, C. Vendrely, G. V. Guinea, *J. Polym. Sci. Part B: Polym. Phys.* **2012**, *50*, 455.
- [220] L. Hu, Q. Chen, J. Yao, Z. Shao, X. Chen, *Biomacromolecules* **2020**, *21*, 5306.
- [221] M. Elices, G. R. Plaza, M. A. Arnedo, J. Pérez-Rigueiro, F. G. Torres, G. V. Guinea, *Biomacromolecules* **2009**, *10*, 1904.
- [222] M. J. Buehler, *Nano Today* **2010**, *5*, 379.
- [223] X. Hu, K. Shmelev, L. Sun, E.-S. Gil, S.-H. Park, P. Cebe, D. L. Kaplan, *Biomacromolecules* **2011**, *12*, 1686.
- [224] Y. Wang, R. Ma, K. Hu, S. Kim, G. Fang, Z. Shao, V. V. Tsukruk, *ACS Appl. Mater. Interfaces* **2016**, *8*, 24962.
- [225] E. Axpe, A. Duraj-Thatte, Y. Chang, D. M. Kaimaki, A. Sanchez-Sanchez, H. B. Caliskan, N. M. Dorval Courchesne, N. S. Joshi, *ACS Biomater. Sci. Eng.* **2018**, *4*, 2100.
- [226] C. Li, A. K. Born, T. Schweizer, M. Zenobi-Wong, M. Cerruti, R. Mezzenga, *Adv. Mater.* **2014**, *26*, 3207.
- [227] C. Li, J. Adamcik, R. Mezzenga, *Nat. Nanotechnol.* **2012**, *7*, 421.
- [228] A. Manjula-Basavanna, A. M. Duraj-Thatte, N. S. Joshi, *Adv. Funct. Mater.* **2021**, *31*, 2010784.
- [229] A. M. Duraj-Thatte, A. Manjula-Basavanna, N.-M. D. Courchesne, G. I. Cannici, A. Sánchez-Ferrer, B. P. Frank, L. van't Hag, S. K. Cotts, D. H. Fairbrother, R. Mezzenga, N. S. Joshi, *Nat. Chem. Biol.* **2021**, *17*, 732.
- [230] E. Roumeli, R. Hendrickx, L. Bonanomi, A. Vashisth, K. Rinaldi, C. Daraio, *Proc. Natl. Acad. Sci. U. S. A.* **2022**, *119*, e2119523119.
- [231] J. L. Fredricks, H. Iyer, R. McDonald, J. Hsu, A. M. Jimenez, E. Roumeli, *J. Polym. Sci.* **2021**, *59*, 2878.
- [232] R. Di Giacomo, B. Maresca, M. Angelillo, G. Landi, A. Leone, M. C. Vaccaro, C. Boit, A. Porta, H. C. Neitzert, *IEEE Trans. Nanotechnol.* **2013**, *12*, 1026.
- [233] R. Di Giacomo, C. Daraio, B. Maresca, *Proc. Natl. Acad. Sci. U. S. A.* **2015**, *112*, 4541.
- [234] A. L. Beckwith, J. T. Borenstein, L. F. Velásquez-García, *J. Cleaner Prod.* **2021**, *288*, 125571.
- [235] C. Chen, J. Song, J. Cheng, Z. Pang, W. Gan, G. Chen, Y. Kuang, H. Huang, U. Ray, T. Li, L. Hu, *ACS Nano* **2020**, *14*, 16723.
- [236] X. Yang, M. S. Reid, P. Olsén, L. A. Berglund, *ACS Nano* **2020**, *14*, 724.
- [237] F. Natalio, *Small Methods* **2019**, *3*, 1800136.
- [238] T. Li, J. Song, X. Zhao, Z. Yang, G. Pastel, S. Xu, C. Jia, J. Dai, C. Chen, A. Gong, F. Jiang, Y. Yao, T. Fan, B. Yang, L. Wågberg, R. Yang, L. Hu, *Sci. Adv.* **2018**, *4*, eaar3724.
- [239] J. Song, C. Chen, S. Zhu, M. Zhu, J. Dai, U. Ray, Y. Li, Y. Kuang, Y. Li, N. Quispe, Y. Yao, A. Gong, U. H. Leiste, H. A. Bruck, J. Y. Zhu, A. Vellore, H. Li, M. L. Minus, Z. Jia, A. Martini, T. Li, L. Hu, *Nature* **2018**, *554*, 224.
- [240] Q. Xia, C. Chen, Y. Yao, S. He, X. Wang, J. Li, J. Gao, W. Gan, B. Jiang, M. Cui, L. Hu, *Adv. Mater.* **2021**, *33*, 2001588.

- [241] C. Chen, Y. Kuang, S. Zhu, I. Burgert, T. Keplinger, A. Gong, T. Li, L. Berglund, S. J. Eichhorn, L. Hu, *Nat. Rev. Mater.* **2020**, *5*, 642.
- [242] J. Li, C. Chen, J. Y. Zhu, A. J. Ragauskas, L. Hu, *Acc. Mater. Res.* **2021**, *2*, 606.
- [243] E. Oliaei, F. Berthold, L. A. Berglund, T. Lindström, *ACS Sustainable Chem. Eng.* **2021**, *9*, 1899.
- [244] E. Oliaei, T. Lindström, L. A. Berglund, *Polymer* **2021**, *13*, 2747.
- [245] D. U. Pascoli, A. Dichiaro, E. Roumeli, R. Gustafson, R. Bura, *Carbohydr. Polym.* **2022**, *295*, 119857.
- [246] Y. Wan, J. Wang, M. Gama, R. Guo, Q. Zhang, P. Zhang, F. Yao, H. Luo, *Compos. Part A: Appl. Sci. Manuf.* **2019**, *125*, 105560.
- [247] J. Bustillos, A. Loganathan, R. Agrawal, B. A. Gonzalez, M. G. Perez, S. Ramaswamy, B. Boesl, A. Agarwal, *ACS Appl. Bio Mater.* **2020**, *3*, 3145.
- [248] F. V. Appels, S. Camere, M. Montalti, E. Karana, K. M. Jansen, J. Dijksterhuis, P. Krijgsheld, H. A. Wösten, *Mater. Des.* **2019**, *161*, 64.
- [249] A. Xin, Y. Su, S. Feng, M. Yan, K. Yu, Z. Feng, K. Hoon Lee, L. Sun, Q. Wang, *Adv. Mater.* **2021**, *33*, 2006946.
- [250] P. Anbu, C.-H. Kang, Y.-J. Shin, J.-S. So, *Springerplus* **2016**, *5*, 1.
- [251] N. De Belie, E. Gruyaert, A. Al-Tabbaa, P. Antonaci, C. Baera, D. Bajare, A. Darquennes, R. Davies, L. Ferrara, T. Jefferson, C. Litina, B. Miljevic, A. Otlewska, J. Ranogajec, M. Roig-Flores, K. Paine, P. Lukowski, P. Serna, J.-M. Tulliani, S. Vucetic, J. Wang, H. M. Jonkers, *Adv. Mater. Interfaces* **2018**, *5*, 1800074.
- [252] W. Li, B. Dong, Z. Yang, J. Xu, Q. Chen, H. Li, F. Xing, Z. Jiang, *Adv. Mater.* **2018**, *30*, 1705679.
- [253] C. M. Heveran, S. L. Williams, J. Qiu, J. Artier, M. H. Hubler, S. M. Cook, J. C. Cameron, W. V. Sruhar, *Matter* **2020**, *2*, 481.
- [254] W. V. Sruhar, *Trends Biotechnol.* **2021**, *39*, 574.
- [255] X. Chen, M. Charrier, W. V. Sruhar, *Front. Mater.* **2021**, *7*, 420.
- [256] F. V. Appels, J. Dijksterhuis, C. E. Lukasiewicz, K. M. Jansen, H. A. Wösten, P. Krijgsheld, *Sci. Rep.* **2018**, *8*, 1.
- [257] W. Sun, M. Tajvidi, C. G. Hunt, G. McIntyre, D. J. Gardner, *Sci. Rep.* **2019**, *9*, 1.
- [258] K. Joshi, M. K. Meher, K. M. Poluri, *ACS Appl. Bio Mater.* **2020**, *3*, 1884.
- [259] E. Elsacker, S. Vandeloock, J. Brancart, E. Peeters, L. De Laet, *PLoS One* **2019**, *14*, 1.
- [260] A. Ghazvinian, P. Farrokhsiar, F. Vieira, J. Pecchia, B. Gursoy. in *Architecture in the Age of the 4th Industrial Revolution – Proceedings of the 37th eCAADe and 23rd SIGRaDi Conference*, Vol. 2, Porto, Portugal **2019**, 505.
- [261] M. Islam, G. Tudryn, R. Bucinell, L. Schadler, R. Picu, *Sci. Rep.* **2017**, *7*, 1.
- [262] N. Attias, O. Danai, T. Abitbol, E. Tarazi, N. Ezov, I. Pereman, Y. J. Grobman, *J. Cleaner Prod.* **2020**, *246*, 119037.
- [263] C. Girometta, A. M. Picco, R. M. Baiguera, D. Dondi, S. Babbini, M. Cartabia, M. Pellegrini, E. Savino, *Sustainability* **2019**, *11*, 281.
- [264] M. Jones, T. Huynh, C. Dekiwadia, F. Daver, S. John, *J. Bionosci.* **2017**, *11*, 241.
- [265] M. Haneef, L. Ceseracciu, C. Canale, I. S. Bayer, J. A. Heredia-Guerrero, A. Athanassiou, *Sci. Rep.* **2017**, *7*, 1.
- [266] M. E. Antinori, L. Ceseracciu, G. Mancini, J. A. Heredia-Guerrero, A. Athanassiou, *ACS Appl. Bio Mater.* **2020**, *3*, 1044.
- [267] R. Lelivelt, G. Lindner, P. Teuffel, H. Lamers. in *First International Conference on Bio-based Building Materials*, 22–25 June 2015, Clermont-Ferrand, France **2015**, 1.
- [268] C. Ververis, K. Georghiou, N. Christodoulakis, P. Santas, R. Santas, *Ind. Crops Prod.* **2004**, *19*, 245.
- [269] L. Burhenne, J. Messmer, T. Aicher, M.-P. Laborie, *J. Anal. Appl. Pyrolysis* **2013**, *101*, 177.
- [270] A. Svärd, R. Moriana, E. Brännvall, U. Edlund, *ACS Sustainable Chem. Eng.* **2019**, *7*, 790.
- [271] W. Ji, Z. Shen, Y. Wen, *BioEnergy Res.* **2014**, *7*, 1392.
- [272] E. Bari, H. R. Taghiyari, B. Mohebbi, C. A. Clausen, O. Schmidt, M. A. T. Ghanbary, M. J. Vaseghi, *Holzforschung* **2015**, *69*, 587.
- [273] G. J. Tudryn, L. C. Smith, J. Freitag, R. Bucinell, L. S. Schadler, *J. Polym. Environ.* **2018**, *26*, 1473.
- [274] N. M. Pugno, L. Valentini, *Nanoscale* **2019**, *11*, 3102.
- [275] L. Valentini, S. B. Bon, S. Signetti, M. Tripathi, E. Iacob, N. M. Pugno, *Sci. Rep.* **2016**, *6*, 27031.
- [276] L. Valentini, S. Bittolo Bon, S. Signetti, N. M. Pugno, *ACS Appl. Mater. Interfaces* **2016**, *8*, 7607.
- [277] L. Valentini, S. Bittolo Bon, N. M. Pugno, *Adv. Funct. Mater.* **2017**, *27*, 1606526.
- [278] C. Zhang, P.-L. Show, S.-H. Ho, *Bioresour. Technol.* **2019**, *289*, 121700.
- [279] A. Miharanyan, *J. Appl. Polym. Sci.* **2011**, *119*, 2449.
- [280] S. Ahmed, S. Ikram, S. Kanchi, K. Bisetty, *Biocomposites: Biomedical and Environmental Applications*, 1st ed., Vol. 1, CRC Press, Milton **2018**.
- [281] M. Vert, Y. Doi, K.-H. Hellwich, M. Hess, P. Hodge, P. Kubisa, M. Rinaudo, F. Schué, *Pure Appl. Chem.* **2012**, *84*, 377.
- [282] N. Zulian, E. Klarenbeek, M. Dros. *Algae-based bioplastics 2020*. <https://www.pluralmagazine.net/news-1/algae-based-alternative-to-single-use-plastic-lan9w> (accessed: February 2023).
- [283] K. Larsen. *Studio Kathryn Larsen 2020*. <https://kathrynlarsen.com/seaweedbioplastic> (accessed: February 2023).
- [284] T. Otsuki, F. Zhang, H. Kabeya, T. Hirotsu, *J. Appl. Polym. Sci.* **2004**, *92*, 812.
- [285] K. Liao, P. Grandgeorge, A. M. Jimenez, B. H. Nguyen, E. Roumeli, *Sustain. Mater. Technol.* **2023**, *36*, e00591.
- [286] S. Balasubramanian, K. Yu, A. S. Meyer, E. Karana, M.-E. Aubin-Tam, *Adv. Funct. Mater.* **2021**, *n/a*, 2011162.
- [287] A. Gujar, H. Cui, C. Ji, S. Kubar, R. Li, *Appl. Microbiol.* **2019**, *5*, 1.
- [288] M. I. Khan, J. H. Shin, J. D. Kim, *Microb. Cell Fact.* **2018**, *17*, 36.
- [289] S. Charoensiddhi, M. A. Conlon, C. M. Franco, W. Zhang, *Trends Food Sci. Technol.* **2017**, *70*, 20.
- [290] E. Deniaud-Bouët, N. Kervarec, G. Michel, T. Tonon, B. Kloareg, C. Hervé, *Ann. Bot.* **2014**, *114*, 1203.
- [291] P. Otero, M. Carpena, P. Garcia-Oliveira, J. Echave, A. Soria-Lopez, P. Garcia-Perez, M. Fraga-Corral, H. Cao, S. Nie, J. Xiao, J. Simal-Gandara, M. A. Prieto, *Crit. Rev. Food Sci. Nutr.* **2021**, *1*.
- [292] M. Garcia-Vaquero, G. Rajauria, J. V. O'Doherty, T. Sweeney, *Food Res. Int.* **2017**, *99*, 1011.
- [293] T. M. M. Bernaerts, L. Gheysen, I. Foubert, M. E. Hendrickx, A. M. Van Loey, *Biotechnol. Adv.* **2019**, *37*, 107419.

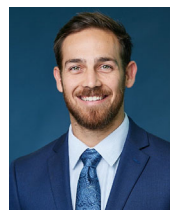
- [294] L. Soto-Sierra, P. Stoykova, Z. L. Nikolov, *Algal Res.* **2018**, 36, 175.
- [295] M. L. Amorim, J. Soares, J. S. D. R. Coimbra, M. D. O. Leite, L. F. T. Albino, M. A. Martins, *Crit. Rev. Food Sci. Nutr.* **2021**, 61, 1976.
- [296] J. Wei, X. Zhang, S. Ai, Y. Huang, X. Yang, Y. Mei, K. Zhang, H. Wang, *Bioresour. Technol.* **2022**, 344, 126317.
- [297] V. Nóbrega, M. Faria, A. Quintana, M. Kaufmann, A. Ferreira, N. Cordeiro, *Materials* **2019**, 12, 2275.
- [298] V. V. Devadas, K. S. Khoo, W. Y. Chia, K. W. Chew, H. S. H. Munawaroh, M.-K. Lam, J.-W. Lim, Y.-C. Ho, K. T. Lee, P. L. Show, *Bioresour. Technol.* **2021**, 325, 124702.
- [299] S. Onen Cinar, Z. K. Chong, M. A. Kucuker, N. Wiczorek, U. Cengiz, K. Kuchta, *Int. J. Environ. Res. Publ. Health* **2020**, 17, 3842.
- [300] N. Zhu, M. Ye, D. Shi, M. Chen, *Macromol. Res.* **2017**, 25, 165.
- [301] M. A. Zeller, R. Hunt, A. Jones, S. Sharma, *J. Appl. Polym. Sci.* **2013**, 130, 3263.
- [302] C. Mathiot, P. Ponge, B. Gallard, J.-F. Sassi, F. Delrue, N. Le Moigne, *Carbohydr. Polym.* **2019**, 208, 142.
- [303] E. Chiellini, P. Cinelli, V. I. Ilieva, M. Martera, *Biomacromolecules* **2008**, 9, 1007.
- [304] M. Bulota, T. Budtova, *Compos. Part A: Appl. Sci. Manuf.* **2015**, 73, 109.
- [305] M. M. Hassan, M. Mueller, M. H. Wagners, *J. Appl. Polym. Sci.* **2008**, 109, 1242.
- [306] S. Jantasrirad, J. Mayakun, A. Numnuam, K. Kaewtatip, *Algal Res.* **2021**, 56, 102321.
- [307] B. Purvis, Y. Mao, D. Robinson, *Sustain. Sci.* **2019**, 14, 681.
- [308] M. Hajian, S. Jangchi Kashani, in *Sustainable Resource Management* (Eds: C. M. Hussain, J. F. Velasco-Muñoz), Elsevier, Amsterdam, Netherlands **2021**, p. 1, ISBN 978-0-12-824342-8.
- [309] E. MacArthur. *What is Circular Economy?* <https://ellenmacarthurfoundation.org/topics/circular-economy-introduction/overview> (accessed January 2023).
- [310] OECD. *The Bioeconomy to 2030: designing a policy agenda.* <https://www.oecd.org/futures/long-termtechnologicalsocietalchallenges/thebioeconomyto2030designingapolicyagenda.htm> (accessed January 2023).
- [311] E. C. D. Tan, P. Lamers, *Front. Sustain.* **2021**, 2, 701509.
- [312] C. L. Partners. *Navigating Plastic Alternatives in a Circular Economy* **2022**.

## AUTHOR BIOGRAPHIES



**Jeremy L. Fredricks** received his B.S. (2016) and M.S. (2018) in Materials Science and Engineering from Cornell University, where he worked on the hydrothermal synthesis of bismuth iron oxides in Prof. Lara Estrhoff's Bio-inspired Materials Synthesis Lab. Following, he took a half-year internship at Sekisui Chemical Co. in Tsukuba, Japan, where he worked on developing metal nanocatalysts for the

conversion of 2-carbon to 4-carbon compounds. Currently, he is obtaining his Ph.D. in the Roumeli Lab at University of Washington, investigating the synthesis and processing of biomatter-based composites of varying complexity components.



Dr. **Andrew M. Jimenez** received his B.S. (2015) in chemical engineering from the University of Arizona, where he studied adsorption/desorption kinetics in semiconductor applications. Following this, he completed his Ph.D. in chemical engineering at Columbia University (2020) under Prof. Sanat Kumar studying the effect of nanoparticle fillers on the crystallization and resulting mechanical properties of polymer composites. His postdoctoral work with Prof. Eleftheria Roumeli (University of Washington, Material Science and Engineering) focused on processing biomatter composites for sustainable plastic alternatives with tunable properties and applications.



Dr. **Paul Grandgeorge** received his B.S. (2012) and M.S. (2014) in mechanical engineering from the École Polytechnique Fédérale de Lausanne (EPFL, Lausanne, Switzerland). He then obtained his PhD in mechanics in 2018 at the d'Alembert Institute (Sorbonne Université, Paris, France), where he worked on elasto-capillary interactions in spider webs and synthetic membranes. After his PhD, he did a postdoc at the Flexible Structures Laboratory (EPFL, Lausanne, Switzerland), working on the mechanics of knots. Currently, during his second postdoc at the Roumeli Lab (Material Science and Engineering, University of Washington, Seattle, USA), he focuses on the fabrication, mechanical characterization, and the modeling of bio-based materials with the aim to replace petroleum-derived plastics.



**Rachel Meidl** LP.D., CHMM, is a strategic thought leader with over 27 years of regulatory, public policy, advocacy and technical experience in industry, academia, government and international relations. She is a distinguished fellow at Rice University's Baker Institute for Public Policy and a strategic advisor for Morgan Stanley Capital International. Her leadership and research portfolio focuses on sustainability, circular economy, life cycle management,

environmental justice, safety and environmental regulations of the treatment, storage, disposal, and transportation of hazardous materials and wastes, and assessing low carbon, alternative energy pathways to understand the environmental, economic, and social impacts across supply chains. She previously was appointed deputy associate administrator for the Pipeline and Hazardous Materials Safety Administration, an agency of the U.S. Department of Transportation. Prior to public service, Dr. Meidl was the director of regulatory and technical affairs at the American Chemistry Council in Washington, DC. She holds a doctorate in law and public policy from Northeastern University.



**Esther Law** received her B.S. (2020) and M.S. (2021) in Materials Science & Engineering from the University of Washington (UW) in Seattle, Washington, USA. Her B.S. research was focused on the advancing continuous carbon fiber filaments for 3D printing thermoplastic composites with Dr. Dywan Arola (UW) and Dr. K. Matsuzaki from the Tokyo Institute of Technology. She also worked as a research assistant on the research topic of microbial challenge of Zirconia–Titanium striped composite dental implant. During her M.S. thesis, she investigated the fabrication of bacteria cellulose infiltrated with lignin nanocomposite in the group of Dr. Eleftheria Roumeli.



**Jiadi Fan** received his master's degree in mechanical and aerospace department from Cornell University in 2014, and his PhD in aerospace engineering and mechanics department from University of Minnesota in 2020. His research interest is to

use multiscale material modeling to study the phase transition in crystalline materials, mechanical and thermal properties of polymer and polymer composites. He is also interested in using the phase field model and cohesive zone model to study the fracture of concrete and polymer. He is now a research specialist at 3M company.



**Eleftheria Roumeli** received her B.S. (2009) and Ph.D. in Physics (2014) from the Aristotle University of Thessaloniki in Greece. Her PhD focused on the processing, mechanical, and thermal properties of synthetic polymer nanocomposite materials. She then did a postdoc at Tampere University of Technology in 2015, followed by postdoctoral work at ETH Zurich (2015–2017) and California Institute of Technology (2017–2020). In January 2020, she joined the Materials Science & Engineering Department of the University of Washington (UW) as an Assistant Professor. Her group focuses on creating sustainable polymeric materials from biological matter with applications in bioplastics, biocomposites and green structural materials.

**How to cite this article:** J. L. Fredricks, A. M. Jimenez, P. Grandgeorge, R. Meidl, E. Law, J. Fan, E. Roumeli, *J. Polym. Sci.* **2023**, 1. <https://doi.org/10.1002/pol.20230126>